# Multi-stage metamorphic evolution and protolith reconstruction of spinel-bearing and symplectite-bearing ultramafic rocks in the Zheltau massif, Southern Kazakhstan (Central Asian Orogenic Belt)

Pilitsyna, Anfisa V.; Tretyakov, Andrey A.; Degtyarev, Kirill E.; Alifirova, Taisia A.; Batanova, Valentina G.; Cuthbert, Simon J.; Kovalchuk, Elena V.; Ermolaev, Boris V.

*Published in:*
Gondwana Research

*DOI:*
10.1016/j.gr.2018.06.005

Published: 31/12/2018

*Document Version*
Peer reviewed version

Accepted Manuscript


# Multi-stage metamorphic evolution and protolith reconstruction of spinel-bearing and symplectite-bearing ultramafic rocks in the Zheltau massif, Southern Kazakhstan (Central Asian Orogenic Belt)

Anfisa V. Pilitsyna, Andrey A. Tretyakov, Kirill E. Degtyarev, Taisia A. Alifirova, Valentina G. Batanova, Simon J. Cuthbert, Elena V. Kovalchuk, Boris V. Ermolaev

PII: S1342-937X(18)30202-8
DOI: doi:10.1016/j.gr.2018.06.005
Reference: GR 2002

To appear in: *Gondwana Research*

Received date: 30 September 2017
Revised date: 22 June 2018
Accepted date: 23 June 2018

Please cite this article as: Anfisa V. Pilitsyna, Andrey A. Tretyakov, Kirill E. Degtyarev, Taisia A. Alifirova, Valentina G. Batanova, Simon J. Cuthbert, Elena V. Kovalchuk, Boris V. Ermolaev , Multi-stage metamorphic evolution and protolith reconstruction of spinel-bearing and symplectite-bearing ultramafic rocks in the Zheltau massif, Southern Kazakhstan (Central Asian Orogenic Belt). Gr (2018), doi:10.1016/j.gr.2018.06.005

# Multi-stage metamorphic evolution and protolith reconstruction of spinel-bearing and symplectite-bearing ultramafic rocks in the Zheltau massif, Southern Kazakhstan (Central Asian Orogenic Belt).

Anfisa V. Pilitsyna[1,*], Andrey A. Tretyakov[1], Kirill E. Degtyarev[1], Taisia A. Alifirova[2], Valentina G. Batanova[3,4], Simon J. Cuthbert[5], Elena V. Kovalchuk[6], Boris V. Ermolaev[1]

[1]Geological Institute of Russian Academy of Sciences, Pyzhevsky lane, 7, Moscow, Russia;

[2] Sobolev Institute of Geology and Mineralogy, Siberian Branch of Russian Academy of Sciences, Koptyuga st., 3, Novosibirsk, Russia;

[3] Univ. Grenoble Alpes, Univ. Savoie Mont Blanc, CNRS, IRD, IFSTTAR, ISTerre, 38000 Grenoble, France;

[4]Vernadsky Institute of Geochemistry and Analytical Chemistry of Russian Academy of Sciences, Kosygin str. 19, Moscow, Russia;

[5]University of the West of Scotland, School of Science, Paisley PA1 2BE, United Kingdom;

[6]Institute of mineralogy, geochemistry and petrography of Russian Academy of Sciences, Staromonetny lane, 35, Moscow, Russia.

***Corresponding author e-mail:** an.pilitsyna@gmail.com (Anfisa Pilitsyna).

Telephone: +79265443256; Post address: Pyzhevsky lane, 7, Moscow, Russia (zip-code 119017), room 319.

**Co-authors:**

and8486@yandex.ru (Andrey Tretyakov)

degtkir@mail.ru (Kirill Degtyarev)

talifirova@gmail.com (Taisia Alifirova)

valentina.batanova@univ-grenoble-alpes.fr (Valentina Batanova)

Simon.Cuthbert@uws.ac.uk (Simon Cuthbert)

elena7kovalchuk@gmail.com (Elena Kovalchuk)

analytic@ginras.ru (Boris Ermolaev)

**Abstract.**

Spinel-bearing ultramafic rocks, metamorphosed in high-pressure conditions, are described from the metamorphic complexes of the western part of the Central Asian Orogenic Belt (CAOB) in the Chu-Yili region in Southern Kazakhstan. They comprise small bodies of magnetite-bearing serpentinites, Cr-spinel-bearing serpentinized and amphibolitized dunites and peridotites enclosed by strongly retrogressed kyanite-bearing paragneisses. Apart from serpentinization, the ultramafic rocks were also overprinted by later rodingitization expressed in the development of the index-minerals hydrogrossular, prehnite and vuagnatite. Cr-spinel-bearing peridotites are characterized by extensive development of symplectitic and coronitic microtextures, which are interpreted to have been formed after garnet breakdown during decompression (i.e. exhumation). Calculated pressure (P) and temperature (T) obtained by phase diagram modeling and conventional geothermobarometry for the symplectites were P 11.5 – 14.5 kbar for a wide temperature range of T 600 – 850° C, which followed the transition from garnet to spinel peridotite. Major and trace element whole-rock geochemical characteristics of the spinel-bearing ultramafic rocks as well as their structurally close relations indicate their mutual origin as parts of an oceanic cumulate complex of an arc - basin system. The protoliths were probably plagioclase-bearing (thus shallow, crustal) ultramafic rocks and troctolites, subducted to eclogite facies conditions and then exhumed along with other metamorphic complexes of the Zheltau massif. These spinel-bearing ultramafic rocks could be classified as crustal formations in accordance with the inferred depths of their origin (< 5 kbar), in common with many HP ultramafic/mafic complexes in the CAOB. However, strongly depleted geochemical signatures of the rocks, together with the distinctive microtextural features observed in the spinel

peridotites, are unique, and their occurrence in the western CAOB is described here for the first time.

**Key words:** spinel peridotite; Cpx-Opx-Spl symplectite; HP metamorphism; west Central Asian Orogenic Belt; cumulate.

## Introduction.

In recent decades much attention has been devoted to the study of ultramafic and mafic rocks within metamorphic orogenic terranes worldwide e.g. Dabie-Sulu, China (Zhang et al., 2000); Western Gneiss Region, Norway; Bohemian massif, Czech Republic (Medaris et al., 1995; Brueckner and Medaris, 2000); Ulten zone, Italian Alps (Godard et al., 1996) where tectonic exhumation processes following subduction or collision events have led to exposure of ultramafic-mafic ultrahigh-pressure (UHP) and high-pressure (HP) lithologies, represented by more or less retrogressed garnet and spinel peridotites, eclogites and garnet pyroxenites. The provenance of such rocks and the mechanisms of their emplacement into continental crust (especially for ultramafic rocks) are of great significance for understanding the dynamics of plate collision and continental subduction (e.g. Zhang et al., 2000; Brueckner and Medaris, 2000; Medaris et al., 2004; Ernst et al., 2007; Zhang et al., 2011). Generally, these rocks are interpreted to have been formed as a result of the tectonic burial (subduction) of oceanic or thinned continental lithosphere fragments to depths corresponding to the eclogite facies. Subsequent exhumation may have been induced by slab break-off and subsequent buoyancy-driven ascent, underplating with tectonic erosion or tectonic extrusion (Ernst et al., 2007).

Geochemical affiliations of ultramafic-mafic rocks in continental (U)HP terrains are characterized by their great diversity, where the main groups are either mantle-derived, or crustal in the form of intrusions differentiated from mafic melts (Zhang et al., 2000; Brueckner and Medaris, 2000; Ernst et al., 2007). Giving that these ultramafic and mafic lithologies tend to retain relict (U)HP minerals significantly more often in comparison to felsic rocks (Ernst et al., 1998; Proyer, 2003), the identification of mafic and ultramafic HP and UHP rocks within

collisional orogens provides a key type of evidence for understanding the paleotectonic processes that operated within them and their resultant tectonothermal evolution.

In western Central Asian Orogenic Belt (CAOB) (Fig. 1, A) the overwhelming majority of ultramafic and mafic (U)HP rocks are metabasic eclogites. These have been described in detail in the Kokchetav massif, Northern Kazakhstan (Kushev and Vinogradov, 1978; Dobretsov et al., 1989; Okamoto et al., 2000; Katayama et al., 2001), the Makbal and Aktyuz Complexes of Kyrgyz North Tien Shan (Dobretsov et al., 1989; Meyer et al., 2013; 2014; Orozbaev et al., 2010; Klemd et al., 2014), Kassansai (South Chatkal) Complex of Middle Tien Shan (Loury et al., 2015), and Atbashi and Akeyaz Complexes of Kyrgyz and Chinese South Tien Shan (Biryukov, 1988; Hegner et al., 2010; Klemd et al., 2015; Liu et al., 2013; Zhang et al., 2013; Soldner et al., 2016; Tan et al., 2017). Ultramafic rocks such as garnet and spinel peridotites are commonly found in UHP-HP metamorphic complexes throughout the world in association with eclogites. In the western CAOB they have only been described to date in the Kokchetav massif (Dobretsov et al., 1989; Zhang et al., 1997), where peridotites are interpreted to have been formed after shallow layered ultramafic intrusions intruded into the upper part of the continental crust prior to subduction. These correspond to the “crustal” type of UHP ultramafic rocks (e.g. Reverdatto et al., 2008).

During fieldworks in 2014-2015, intensively metamorphosed spinel-bearing ultramafic rocks with chemical compositions similar to depleted, mantle-derived peridotites were discovered by the authors in the Zheltau massif of Southern Kazakhstan. The rocks provide evidence for a multistage metamorphic evolution, expressed in the abundance of symplectitic and coronitic microtextures, similar to those described by, for example, Godard et al. (2000), Morishita and Arai (2003), Song et al. (2009), Obata (2011), Obata et al. (2012). Furthermore, the chemical compositions of these rocks clearly indicate that their formation was accompanied by pervasive element redistribution both prior to collision and during tectonic burial and exhumation. This paper reports on our discovery of depleted spinel-bearing ultramafic rocks in

the western CAOB and we present evidence that they experienced at least high-pressure metamorphism. Through whole-rock geochemistry, petrological observations and geothermobarometry we were able to distinguish the main stages of metamorphic evolution for the rocks, deduce their protolith affinities and determine their geodynamic significance for tectonic evolution of the studied region as parts of oceanic lithosphere, subducted to high-pressure conditions. These are a new type of ultramafic HP lithologies, described for the first type from the west CAOB.

## 1. Geological outline.

In western CAOB within Kazakhstan, Tien Shan and NW China, large blocks (massifs) composed of Precambrian continental crust, forming narrow (≥200 km) but long (≤2600 km) fault-bounded domains, separated from each other by Early Paleozoic sutures, which contain fragments of oceanic arcs, accretionary wedges along with dismembered ophiolites (Fig. 1, A). HP and UHP rocks are normally found within the Precambrian massifs, e.g. the HP and UHP complexes of the Zerendy Group in the Kokchetav massif; the Makbal UHP complex of the Issyk-Kul massif and the Aktyuz HP complex of the Chu-Kendyktas Precambrian massif (Dobretsov et al., 1989; Klemd et al., 2014; Meyer et al., 2014; Degtyarev et al., 2017; etc.). These are generally represented by diverse mica schists and gneisses tectonically interfingered with eclogites, retrogressed eclogites and garnet amphibolites. In the case of the Kokchetav massif, garnet and spinel peridotites associated with mica schists are also present (Kushev and Vinogradov, 1978; Zhang et al., 1997).

The Zheltau Precambrian massif (also referred to as Anrakhai or Chu-Yili microcontinent (e.g. Windley et al. 2007; Alexeiev et al., 2011)), located in the SE part of the Chu-Yili Mountains (Southern Kazakhstan), is represented by a narrow (5-25 km) NW-trending block, more than 200 km long. In the SW the Zheltau massif is bounded by the Early Paleozoic Dzhalair-Naiman ophiolite suture zone, which divides the Zheltau massif from the Chu-Kendyktas Precambrian massif (Fig. 1, B). The Dzhalair-Naiman zone consists of early

Cambrian dismembered ophiolites (ultramafics, gabbroids, tonalites, plagiogranites, basalts and rhyolites) as well as late Cambrian felsic to basic unmetamorphosed volcanic rocks, overlain by Early Ordovician turbidites and carbonates (Ryazantsev et al., 2009b; Degtyarev, 2012). Ophiolitic and deeper marine sediments of the Dzhalair-Naiman suture and Precambrian rocks of the Zheltau massif are unconformably overlain by Middle and Late Ordovician marine siliciclastic deposits (Fig. 2, A).

In the Zheltau massif various Precambrian and Early Paleozoic metamorphic and magmatic complexes are present (Fig.2, A). Precambrian formations make up Anrakhai and Koyandy metamorphic complexes (Alexeiev et al., 2011; Tretyakov et al., 2016b; Degtyarev et al., 2017). The Anrakhai complex is most extensive in the SW part of the massif, consisting of orthogneisses with bodies of amphibolites. The orthogneisses predominate and have mainly Neoproterozoic protolith ages ~ 800 Ma (Tretyakov et al., 2016b) and 741± 1 Ma (Kröner et al., 2007), but a group of subalkaline amphibole-bearing varieties have yielded Paleoproterozoic protolith ages (1789 ± 1 Ma, 2187± 1 Ma; (Kröner et al., 2007), and 1841 ± 6 Ma (Tretyakov et al., 2016b)).

The Anrakhai complex has overthrust the Koyandy complex, whose outcrop is considerably less extensive within the Zheltau massif. The Koyandy complex consists of strongly retrogressed and mylonitized garnet-mica paragneisses with relics of tourmaline, phengite, alkaline feldspar and kyanite, indicating their high-pressure origin (e.g. Kotková, 2007). These contain lenses and pods of mylonitized quartz-feldspar orthogneisses, meta-arenites and metacarbonates, muscovite-chlorite schists and garnet amphibolites that form a NW-trending band 50 m to 1.5 km wide. The protolith ages for garnet-mica paragneisses, are constrained by detrital zircons, which span a wide range from 694 ± 7 to 2257 ± 27 Ma (Alexeiev et al., 2011), implying a maximum Neoproterozoic (Cryogenian) age for the Koyandy Complex, the clastic material of which may have been sourced from the Anrakhai complex (Degtyarev et al., 2017).

The garnet-mica paragneisses of the Koyandy complex also enclose pods of ultramafic rocks formed under at least HP metamorphic conditions and represented by eclogites and garnet clinopyroxenites, with the age of HP metamorphism estimated from U-Pb zircon dating at 489±9 Ma, corresponding to the Cambrian-Ordovician boundary (Alexeiev et al., 2011). These rocks are interpreted to have been formed during subduction of mafic-ultramafic intrusions within continental crust (Pilitsyna et al., 2018); they correspond to the "crustal" type of HP ultramafic-mafic rocks (Carswell et al., 1983; Zhang et al., 2000; Reverdatto et al., 2008).

In the SE part of the Zheltau massif sparse bodies of ultramafic rocks, represented by serpentinites and amphibolitized peridotites, are also exposed among the garnet-kyanite gneisses of the Koyandy complex (Fig. 2, A). One of the pods (250 m × 120 m), containing bodies of relatively less altered spinel peridotite and accompanying varieties (see Section 2 below), was sampled and the results are provided in the following (Fig. 2, B).

In the NE part of the Zheltau massif the Koyandy complex has been overthrust by dismembered Cambrian (?) ophiolites (mainly serpentinites and deformed banded, amphibolitized gabbroids; their age has been estimated on the basis of the stratigraphic evidences), which make up narrow zone up to 500 m wide (Fig. 2, A). These gabbroids are thought to represent the upper parts of the ophiolitic sequence (discussed in Paragraphs 4.2, 4.3 hereinafter).

The Koyandy complex and the ophiolites are bounded by a narrow (20 x 1 km) unmetamorphosed granodiorite-granite body with a protolith age of 509±3 Ma, corresponding to the Middle Cambrian. It is noteworthy that the granitoids contain xenoliths of amphibolite and zircons have xenocrystic cores of Early- and Mesoproterozoic ages. Chemical compositions of the granitoids indicate their supra-subduction zone derivation within an ensialic island arc (Alexeiev et al., 2011).

The Zheltau massif is unconformably overlain by unmetamorphosed, Early-to-Middle Ordovician clastic and carbonate strata (Nedovizin, 1961; Abdulin et al., 1980; Nikitina et al., 2006).

## 2. Field relations and petrography of the main rock types.

Serpentinite is the predominant lithology among the studied spinel-bearing ultramafic rocks of the Koyandy complex. They form pods of average length 100-150 m in the southeastern part of the complex (Fig. 2, A) and generally consist of talcites and talc-chlorite schists in addition to the serpentinites. However, one of the large pods (Fig. 2, B) (43°50´17.1´´ N; 75°32´12.4´´ E) is characterized by a patchy structure where homogenous, magnetite-bearing serpentinite encloses dismembered layers, from a few decimeters to several meters thick, of chrome spinel-bearing serpentinized dunite, chrome spinel-bearing peridotite, amphibole-rich peridotite with relics of olivine and hornblendite ('Ashchisu river pod'). Contacts between these varieties and the enclosing serpentinite are obscured due to the strong serpentinization of all rock types. Importantly, the spinel-bearing ultramafic rocks also contain chloritized and serpentinized *mafic* varieties.

The ultramafic rocks were evidently overprinted by late metasomatic changes, since almost all of them contain a number of phases normally associated with rodingites. Layers of nearly completely rodingitizied lithologies are enclosed by serpentinites. The petrography of these metasomatic rocks has been considered separately from the predominant metamorphic parageneses from hereon.

### 2.1. Metamorphic parageneses.

*Magnetite-bearing serpentinites* are the prevailing variety and characterized by typical mesh- textures, formed by serpentine (lizardite) after olivine (Ol). No relics of Ol are generally present; however, the olivine habit is well-preserved. Magnetite (Mag) is developed among the cracks in Ol as well as forming black, rounded grains up to 0.3 mm (possibly after chromium spinel (Cr-Spl)).

*Cr-Spl-bearing serpentinized dunites* possess fine- to medium-grained textures, made up by Ol and Cr-Spl, forming the groundmass; interstices are filled by serpentine (lizardite) (Fig. 3, a). Olivine is characterized by roundish, relatively fresh, quasi-euhedral grains varying from 0.2 to 1.7 mm. However, they are intensely fractured, following an imperfect cleavage. Lizardite and magnetite are developed along the fractures. Cr-Spl is represented by dark-brown roundish grains up to 0.5 mm, replaced by black Mag from the rims. Among the late minerals Cr-bearing chlorite, amphibole and carbonate (probably related to metasomatism) are present.

*Cr-Spl peridotites* (or *symplectite-bearing peridotites* (Bodinier and Godard, 2003)) demonstrate characteristic mineral assemblages of the different metamorphic stages. They consist of anhedral Ol (0.1 mm to 1.5 mm), in *all* cases rimmed by orthopyroxene (Opx) coronas identical to the Coarse Opx Rim (COR) of Obata and Ozawa (2011) (Fig. 3, b). The sizes of the COR's vary considerably, from 0.1 mm to 0.8 mm, and in many cases the COR's almost completely replace Ol. Furthermore, Opx is a constituent of the symplectites, which also are composed of pale green spinel (Spl) and clinopyroxene (Cpx). The symplectites are fine-grained, "worm-like" fibrous intergrowths of spinel with ortho- and clinopyroxenes (Fig. 3, c) and make up more than 30% of the rock volume. Frequently, these symplectites have a "seam" in the center of the Cpx-Opx-Spl symplectitic body (clearly indicated on Fig. 4, f), extended subparallel to the COR's. Cpx-Opx-Spl symplectites are enclosed by more coarse-grained amphibole-spinel (Amp-Spl) symplectites in which colorless amphibole and pale green Spl also form sheaf-like intergrowths (Fig.3, d). However, taking into account the grain sizes of Amp-Spl symplectites, which are considerably coarser than the enclosed Cpx-Opx-Spl symplectites (Fig. 3, d), and the complete absence of amphibole inside of the pyroxene-spinel (Px-Spl) symplectitic body (Fig. 3, c), it could be proposed that Amp-Spl symplectites were formed after Cpx-Opx-Spl symplectites. In most cases Amp-Spl symplectites have direct boundaries with the COR's, whereas the earlier Cpx-Opx-Spl symplectites hardly ever preserve boundaries with the COR's. Cr-bearing Cpx forms brownish aggregates and rims around the COR's up to 1.5 mm in size,

occasionally exhibiting well-preserved cleavages, and replace the COR's and the symplectites (Fig. 3, e). In one case Cpx contains an inclusion of dolomite. Cr-Spl of the symplectite-bearing peridotites is characterized by several types. Ol, Cr-Cpx and the COR's enclose grains of Cr-Spl from 0.005 mm to 0.8 mm (Fig. 4, a); zoned grains of Cr-Spl (0.1-0.3 mm) that are dark-brown in the center and grade to pale-green color towards the rims frequently lie close to the boundaries between the COR's and the symplectites (Fig. 4, b). Tiny oriented needles of Cr-Spl up to 3 μm in size, probably representing an exsolved phases, are contained within a number of grains of Ol (Fig. 4, c). The last metamorphic stage (or stages) involved the formation of anhedral pale-green Spl (up to 1 mm) and colorless amphibole (Fig. 4, d) as well as chlorite, magnetite, carbonate and serpentine. Homogenous reddish-brown grains of Cr-Spl (0.2 – 1 mm in size), chlorite and some amphiboles in the most rodingitizied varieties could be possibly attributed to a late metasomatic stage or stages.

*Amphibolitized Cr-Spl peridotites* are a strongly altered variety of the Cr-Spl (symplectite-bearing) peridotites described above. Olivine (up to 1.2 mm) and Cr-Spl are preserved only as relics (Fig.4, e); Cr-Spl is almost completely replaced by Mag, whereas the groundmass consists of colorless amphibole grains 0.05 mm to 0.7 mm long. Serpentine and minor carbonate are also present as interstitial phases or fill fractures in Ol.

### 2.2. Metasomatic mineral assemblages.

Minerals that can be robustly attributed to the late metasomatic stage in the Cr-Spl (symplectite-bearing) peridotites are prehnite and hydrogrossular (Rice, 1983), forming small isolated areas up to 1-1.5 $mm^2$ in the groundmass. Moreover, within the Cpx-Opx-Spl "symplectitic seams" prehnite, hydrogrossular and chlorite, together with vuagnatite, are developed (Fig. 4, f). The last mineral appears to be exotic and has mostly been found within rodingitic zones of ophiolites (Sarp et al., 1976). Sr-bearing zoisite (niigataite) within prehnite was also identified. Cr-bearing chlorite in the spinel-bearing serpentinized dunites forms prismatic grains varying from 0.5 to 1 mm (Fig. 3, a) and could be attributed to retrograde

metamorphic rather than metasomatic stages, involving an ingress of water. It should be noted, that among the ultramafic bodies there are intensively rodingitizied varieties, where more than 70 vol.% of the rocks are made up by metasomatic assemblages.

## 3. Whole-rock geochemistry and mineral chemistry.

Ultramafic rocks of the Zheltau massif were extensively altered during the later stages of metamorphism, therefore the early mineral parageneses have largely been destroyed; hence their whole-rock geochemistry is the main key to understanding of their protolith compositions and affinities. However, chemical compositions of the studied rocks could also have been influenced by retrogression and metasomatism. Metamorphic evolution of the rocks may, in turn, been reconstructed from the phase chemical compositions and textural relationships. Cr-spinel-bearing serpentinized dunites and Cr-spinel (symplectite-bearing) peridotites were selected from relatively fresh parts of the 'Ashchisu river pod' (see Fig. 2, B) with massive structures so as to minimize the influence of volatile components and metasomatism. Nonetheless, the effects of serpentinization and rodingitization are pervasive and the losses on ignition vary in the ranges 6.5 – 14 wt.% (Table 1). Supplementary whole-rock chemical compositions of mafic metamorphic lithologies from the studied pod (Fig. 2, B), as well as ophiolitic serpentinites and amphibolitized gabbroids from the NE part of the massif (Fig. 2, A) are provided in Table S1.

### 3.1. Analytical methods.

#### 3.1.1. Whole-rock geochemistry analytical procedures.

Major elements were determined by XRF using a Bruker AXS wavelength dispersive S4 PIONEER spectrometer with a 4 kW X-ray tube in the Geological Institute of the Russian Academy of Sciences (RAS). Data processing was implemented using the «Spectra-Plus$^{TM}$» software package. Calibration was based upon ultramafic rocks standards. Automatic registration of peak overlaps and correction for matrix effects were carried out during individual measurements of fundamental parameters for each sample. The standard reference materials for major element determinations were: 1) Russian standard sample of dunite SDU-1 (Catalog of the

standards of natural and technology-related mediums; IGI Irkutsk 2009, Russia); 2) Peridotite powders MY-1 and MY-2 (Russian Academy of Sciences, Institute of Geology of Ore deposits, GeoRem database, Application version 21, January 2017); 3) United States Geological Survey (USGS) Certificate of Analysis Dunite, DTS-1 (Flanagan, 1967). Intervals of analyzed concentrations obtained after recalculation to oxides (mass fraction %) were: Si – 0.01–1.0, Ti – 0.01–5.0, Al – 1.0–60.0, Fe(total) – 1.0–40.0, Mn – 0.01–1.0, Ca – 1.0–50, Mg – 0.1–40, Na – 0.1–10.0, K – 0.1–10.0, P – 0.01–5.0. Ferric and ferrous iron (with labels "init" in the 1) were calculated using the HCAM 50-X titrimetric bichromatic method (Kazakhstan Institute of Metrology; reg. number KZ.07.00.03141-2015 from 12.05.2015). However, the obtained values of $Fe_2O_3$ seem to be overestimated; thus the corrections after Irvine and Baragar (1971) for highly oxidized rocks were introduced (with labels "I&B" in the Table 1). The latter values were used in the consideration in the following.

Trace elements were acquired in the Analytical Centre of the Institute of Microelectronics Technology and High-Purity Materials RAS using an ICP-MS on a Perkin Elmer ELAN 6100 DRC as well as by atomic emission spectrometry with ICP-MS (ICAP-61, Thermo Jarrell Ash; X-7, Thermo Elemental, USA). The relative standard deviation for all analyzed elements was no more than 0.2 for element contents below the five-fold detection limit and below 0.1 for contents above the five-fold detection limit.

Major element concentrations in tables 1, S1 are given in wt.%; trace elements are in ppm.

3.1.2. Analytical procedures for mineral chemistry.

Mineral compositions were determined on a JEOL-8200 electron probe microanalyzer (EPMA) in the Laboratory of Mineral Substances Analysis, Institute of mineralogy, geochemistry and petrography of the RAS, a JEOL JXA-8230 EPMA at the Institut des Sciences de la Terre (ISTerre, University Grenoble Alpes, France) and a JEOL JXA-8100 EPMA at the Analytical Center for multi-elemental and isotope research Siberian Branch (SB) RAS. These were equipped with five wavelength dispersive spectrometers and an energy dispersive (EDX)

spectrometer at an accelerating voltage of 20 kV, probe current of 20 nA, beam diameter of 1 μm. Standards were certified natural minerals and synthetic oxides: Wollastonite (Si, Ca); Corundum (Al), Orthoclase (K), Rhodonite (Mn), Albite (Na), Apatite (P), Rutile (Ti), Hematite (Fe), Periclase (Mg). Chemical compositions of some minerals were also measured using a scanning electron microscope (SEM) JSM-6510 with EDX INCA Energy-350 (Oxford Instruments) MIRA 3 (TESCAN, Czech Republic) at the Analytical Center for multi-elemental and isotope research SB RAS. Analysis was carried out in low vacuum mode in the back-scattered electron regime at an accelerating voltage of 20-30 kV, beam diameter of 1 μm, counting time 20 seconds. EDX-analyzed points are marked in italics in the provided tables S2-S6.

Ferric iron was recalculated for olivine, clino- and orthopyroxene, spinel, amphibole and chlorite on the basis of charge balance and stoichiometry (Droop, 1987). All iron for Sr-zoisite and prehnite was calculated as $Fe^{3+}$. Mineral abbreviations are after Whitney and Evans (2010) with the exception of vuagnatite, taken as Vgn. An additional vuagnatite and lizardite spectrums, confirming the minerals compositions, were obtained with using of a Raman-scattering spectroscopy on the automatic Raman spectrometer XPloRA (Horiba Scientific) (Micro-Raman Laboratory; M. V. Lomonosov Moscow State University) and a high throughput Raman spectrometer inVia Reflex (Renishaw, United Kingdom) at room temperature with a grating of 1800 lpmm, 100x objective, spot diameter 500 nm, 532 nm Nd:YAG laser, 70 mW power at the sample, confocal mode. The measurements were carried out by multiple accumulations (3 accumulations) each for 20 seconds and resolution <3 $cm^{-1}$; frequency span was 100–4000 $cm^{-1}$.

3.2. Whole-rock major and trace element geochemistry of spinel-bearing ultramafic rocks.

Major and trace element analyses results are provided in Table 1. MgO contents across all samples range from 27.93 – 37.88 wt.% (counting out the “dry basis” calculations) with Cr and Ni concentrations of 402 – 3114 ppm and 1085 – 2240 ppm, respectively. The rocks are strongly depleted in $TiO_2$ (151 – 373 ppm) and all REE (∑REE = 0.24 – 0.98 ppm), with the exception of

AH 1511, showing much higher sum of REE due to LREE enrichment. These features are close to those normally described in peridotites derived from mantle sources (Bodinier and Godard, 2003; Janák et al., 2006; Godard et al., 2009). On the other hand, they tend to possess high concentrations of fertile components (e.g. 1.06 – 9.15 wt.% of $Al_2O_3$; 0.12 – 7.07 wt.% of CaO). Amphibole-bearing lithologies are also characterized by perceptible $\sum (Na_2O + K_2O)$ contents (0.21 – 1.06 wt.%). Moreover, the relatively high $FeO_{tot}$ contents (7.12 – 9.79 wt.%) together with moderate MgO contents (Mg# is in the range of 0.78 – 0.83; Table 1) differ from typical refractory peridotites, which are characteristic of residual depleted mantle (e.g. Pearce et al., 2000; Godard et al., 2009).

Normative compositions of the ultramafic rocks, calculated with using of the CIPW method, are shown on Fig. S1 and Table 1. All lithologies are plagioclase-normative to some extent. On the Ol-Pl-Px triangle (after Streckeisen, 1976) they show a range of norm compositions from Pl-bearing ultramafics to troctolites and melanogabbroids. Note that the most magnesian varieties correspond to Pl peridotites, whereas the most aluminous samples lie in the fields of troctolite or melanogabbro. It should be also cautioned that CIPW method is not reliable for petrogenetic interpretations, since it does not take into account amphiboles (which are typical, for example, for subduction-related peridotites (Pearce and Parkinson, 1993)) or contamination by country-rocks, and it is impossible to determine sequences of crystallization using of the CIPW calculations. However, some useful insights into the initial modal compositions of the rocks can be reasonably deduced.

Some element concentrations show clear covariation (Fig. 5). Thus, Cr vs. Ni and CaO vs. $Al_2O_3$ display positive correlations, whereas MgO vs. $Al_2O_3$ and Ca/(Ca+Al) vs. Cr show clear negative correlations. These features are normally attributed to either fractional crystallization or variable degrees of partial melting. HREE and LREE contents do not reveal any obvious covariations, though on Fig. 5 Yb and Ce points fall into the impregnated peridotite field (in accordance with Godard et al., 2009).

C1 chondrite-normalized compositions (Fig. 6, A) of the spinel-bearing ultramafic rocks show moderately depleted REE contents (Yb = 0.15 – 0.47 *x* chondritic; Ce = 0.14 – 0.58 *x* chondritic) with prominent positive Eu anomalies (Eu/Eu* = 1.2 – 11.34). The patterns are also characterized by smoothly U-shaped forms with positive Eu anomalies (except LREE-enriched sample AH 1511) and slight MREE depletion relative to LREE and HREE ($(La/Sm)_n$ – 0.85 – 2.48; $(Dy/Lu)_n$ – 0.31 – 0.68). On the primitive mantle (PM)-normalized plot (Fig. 6, B) the samples display clear positive Sr anomalies, which are complementary to Eu. Furthermore, compared to depleted MORB mantle (DMM) the rocks are considerably enriched in LILE (Rb = 6.46 – 566.75 * DMM; Pb = 31.75 – 114.48 * DMM), whereas REE distribution (right part of the plot) is characterized by MREE and HREE depletion (generally up to 0.25 * DMM).

It should be added that normative plagioclase, recalculated to vol.% (which in some respects could be compared to the mineral modes), has positive correlations with Eu and Sr (Fig. 5), implying the possible link of the observed Eu and Sr anomalies with Pl crystallization on the primary igneous stage. One could argue that Eu anomalies are also often interpreted to have been related to fluid-dominated serpentinization (e.g. in Paulick et al., 2006). However, in our case, LOI in the ultramafic rocks have clear negative correlations with the whole-rock Eu contents (Fig. 5): the highest losses on ignition correspond to the most magnesian varieties, showing at the same time the least Eu contents. Thus, the contents of REE (in particular Eu) have not been significantly modified by serpentinization and associated rodingitization.

### 3.3. Mineral chemistry.

Chemical compositions of representative minerals in Cr-Spl-bearing serpentinized dunites, Cr-Spl (symplectite-bearing) peridotites and amphibolitized peridotites are provided in Tables S2 – S7. Cr-Spl (symplectite-bearing) peridotites possess an abundance of mineral parageneses and reactional microtextures, which help to shed light on the metamorphic evolution of the rocks. Therefore, the overwhelming majority of the analyses have been acquired from the Cr-Spl

(symplectite-bearing) peridotites. These have been used as a basis for P-T estimation and reconstruction of the metamorphic evolution (considered further below).

Chemical compositions of the minerals of the inferred metamorphic stages and the later metasomatic stage are considered separately in sections 3.3.1 and 3.3.2, respectively.

3.3.1. Minerals of the metamorphic stages.

*Olivine* grains in the all lithologies are mostly broken by cracks filled by lizardite (Table S2) and magnetite, and do not exhibit a prominent zonation; they show $Mg/(Mg+Fe^{2+})$ in the range 0.85 – 0.875 (Table S2), indicating a considerable fayalite component. Olivine of the Cr-Spl (symplectite-bearing) and amphibolitized peridotites is characterized by high NiO (up to 0.7 wt.%) and low $Cr_2O_3$ contents (0.001- 0.053 wt.%), whereas in the Cr-Spl serpentinized dunite $Cr_2O_3$ is 0.58 wt.%. In many cases Ol of the Cr-Spl (symplectite-bearing) peridotites contains solid inclusions and oriented exsolutional lamellaes of Cr-Spl.

*Spinel* has the most variable composition in these rocks (Fig. 7, a, b). Cr-Spl of the serpentinized dunites, intensively replaced by Mag, shows Cr/(Cr+Al) in the range of 0.44 – 0.47 (Table S3); almost the same ratios are typical for Cr-Spl relics in the amphibolitized peridotites. In the symplectite-bearing peridotites nodular grains of Cr-Spl, located at the boundaries between Opx coronas around olivine and symplectitic aggregates, demonstrate chemical zonation, clearly expressed in Cr/(Cr+Al) decreasing from core to rim and $Mg/(Mg+Fe^{2+})$ increasing in the same direction. Maximum $Cr_2O_3$ content in the core of Cr-Spl is 35 wt.% (Cr/(Cr+Al) = 0.44). Note that iron contents of the most chromian spinels are high as well, whereas MgO contents are notably low, indicating higher ferrichromite contents in comparison to magnesiochromite. Inclusions of Cr-Spl in Ol, Opx and Cr-bearing Cpx in the symplectite-bearing peridotites show different contents of $Cr_2O_3$, varying from 12 to 33 wt.%. Tiny oriented exsolutional lamellaes of Cr-Spl in olivine are too small to obtain proper analyses and evidently represent mixed values with the host-mineral (Ol). However, they are certainly Cr-bearing with Cr/(Cr+Al) of about 0.2. Al-rich spinel, composing symplectites with Opx + Cpx (early stage)

and Amp (later stage), have high $Mg/(Mg+Fe^{2+})$ ratios (0.72 – 0.75), whereas $Cr_2O_3$ contents are very low; in the case of Cpx-Opx-Spl symplectites chromium contents are sparse and do not exceed 0.3 wt.% (average value for Cpx-Opx-Spl-Amp intergrowth area; Table S7), whereas Spl from Amp-Spl symplectites possess $Cr_2O_3$ up to 1.5 - 2%. Coarser grains of greenish Al-Spl, developed in the groundmass of the symplectite-bearing peridotites, are often enclosed by late Amp crystals. These grains do not show any considerable changes in compositions compared to Spl from the symplectites; nevertheless, they are characterized by anhedral (or roundish) forms and significantly coarser sizes (Fig. 4, d). In the intensively rodingitizied varieties of the peridotites the late reddish spinel is represented by homogenous Cr-Spl without any zonation, possessing distinctly higher $Mg/(Mg+Fe^{2+})$ (0.56 – 0.59), compared to the zoned nodular Cr-Spl, and can probably be affiliated to the metasomatic stage.

*Orthopyroxene* is present in the Cr-Spl (symplectite-bearing) peridotites and as relics in the amphibolitized peridotites; it forms coronas (COR's) around olivine, in some cases replacing Ol completely. $Mg/(Mg+Fe_{tot})$ varies from 0.85 – 0.88 (Fig. 7, c; Table S2). The COR's are characterized by prominent chemical zonation in $Al_2O_3$ distribution with lowest values closest to olivine and the highest values at the boundaries with Cpx or Amp from the symplectites (Table S2). Note that Opx near Amp-Spl symplectites has higher $Al_2O_3$ than that adjacent to the Cpx-Opx-Spl symplectites (e.g. 3.38 wt.% and 1.76 wt.%, respectively). $Mg/(Mg+Fe_{tot})$ is inversely correlated with $Al_2O_3$ in Opx (Fig. 7, c). Fine-grained, fibrous Opx is a constituent of the symplectites ($Opx_{symp}$) along with Cpx and Al-rich Spl (Fig. 8, a). $Opx_{symp}$ has $Mg/(Mg+Fe_{tot})$ = 0.85, similarly to the COR's, while $Al_2O_3$ is relatively high (up to 4.5 wt.%). This could be related to a mixture with neighboring Al-rich spinel. Thus, these analyses clearly indicate the presence of Opx within the early, intimately intergrowing pyroxene-spinel symplectites. This is also confirmed by element mapping (Fig. 8, b). It should be noted that Opx is only developed in the Cr-Spl (symplectite-bearing) peridotites. Some of the intensively rodingitizied varieties retain minor relics of the COR's around almost completely serpentinized Ol.

*Clinopyroxene* of the Cr-Spl (symplectite-bearing) peridotites varies from diopside to augite (Fig. 7, d) with low contents of $\sum(Na_2O+K_2O)$ up to 0.35 wt.% (Table S4). Cpx-Opx-Spl symplectites contain magnesian diopside ($Mg/(Mg+Fe^{2+})$ = 0.92 – 0.94), intergrown with Al-rich Spl and Opx. In some cases relics of the host Cpx (prior to Spl release) are preserved (Fig. 3, c) and characterized by higher $Al_2O_3$ contents than Cpx in symplectite (2.87 wt.% and 2.07 wt.%, respectively). The later stages of metamorphism clearly led to "migration" of Al-Spl from the symplectite masses (possibly related to intense Amp growth during retrogression), whereas the remnants of Cpx show the least contents of $Al_2O_3$ (1.2 – 1.7 wt.%). Cr-bearing Cpx (0.3 – 1.5 wt.% of $Cr_2O_3$), developing as a second rim around olivine (Fig. 3, e) along with the COR's, was one of the latest minerals to form and probably represents a phase of the metasomatic stage, since in the most rodingitizied lithologies Cr-Cpx forms euhedral prismatic crystals with the highest $Cr_2O_3$ contents (1.5 – 1.7 wt.%), whereas the earlier minerals are only present as relics among metasomatic assemblages.

*Amphibole* is a widespread mineral of the Cr-Spl-bearing serpentinized dunites, Cr-Spl (symplectite-bearing) and amphibolitized peridotites, and constitutes symplectites together with Al-rich Spl (only in peridotites) as well as make up the groundmass as discrete grains (Table S4, S5; Fig. 9). All the amphiboles demonstrate consistently high $Mg/(Mg+Fe^{2+})$ in the range of 0.85 – 1.0. Pargasite from the symplectites shows the highest $Al_2O_3$ contents (16 – 19 wt.%); extensive amphibole growth with reduction of Al-Spl "branches" led to a decrease in $Al_2O_3$ in Amp (12 – 13 wt.%). The latest crystals of Amp have magnesiohornblende compositions (with $Al_2O_3$ 10 – 13 wt.%). In the amphibolitized peridotites the groundmass comprises solely magnesiohornblende with the lowest $Al_2O_3$ (9 – 10 wt.%). It should be added that metasomatic areas with chlorite and prehnite normally also include tschermakitic amphiboles. Cr-Spl-bearing serpentinized dunites contain magnesiohornblende and evidently later tremolite.

Other minerals, displaying subordinate development in the rocks, include carbonates (dolomite and calcite), magnetite with overprinted sulphides and lizardite.

Thus, mineral assemblages, mainly in the Cr-Spl (symplectite-bearing) peridotites, are characterized by highly variable chemical compositions, reflecting the significant element redistribution during metamorphic evolution of the rocks; however, the critical phases, namely plagioclase (Pl) or garnet (Grt), are virtually absent in these rocks, considerably complicating the metamorphic history recovery.

3.3.2. Minerals of the metasomatic stage.

As mentioned in Part 2.2., the metasomatic assemblages are frequently located at the symplectitic "seams" in Cr-Spl (symplectite-bearing) peridotites (Fig. 4, f) as well as making up most of the matrix in some ultramafic lithologies. The assemblages reflect extensive rodingitization, normally related to serpentinization (e.g. Bilgrami and Howie, 1960; Li et al., 2007). Ca-rich minerals are represented by hydrogrossular with low FeO contents, prehnite, Sr-bearing zoisite and vuagnatite (Table S6), which is exotic and distinctly metasomatic and has been described only in few places in the world (e.g. Sarp et al., 1976; Craw et al., 1979) (the confirming Raman spectrum is given on Fig. S2). Vuagnatite is evidently present instead of the more typical vesuvianite. Highly magnesian chlorite (MgO in the range of 20 – 35 wt.%) in the Cr-Spl (symplectite-bearing) peridotites and Cr-bearing chlorite (up to 1.05 wt.% of $Cr_2O_3$) of the Cr-Spl serpentinized dunites could be referred to either retrograde metamorphic or metasomatic stages (additional microtextural studies are required).

## 4. Discussion.

The metamorphosed ultramafic rocks of the Zheltau massif are an uncommon case for petrological and geochemical characterization or interpretation. On the one hand the rocks preserve plenty of informative mineral assemblages that could be used to ascertain at least some stages of their petrogenesis. On the other hand, critical phases for P-T determination are absent; moreover, the obtained geochemical patterns may have been affected by one or all of the multi-stage metamorphic and metasomatic processes described above. In spite of these challenges, we believe there is sufficient information from the data presented above to attempt to deduce the

metamorphic evolution and geochemical affiliation of the spinel-bearing ultramafic rocks of the Zheltau massif. The outcomes are set out in the next section.

### 4.1. Metamorphic evolution.

The magnetite-bearing serpentinites and Cr-Spl-bearing serpentinized dunites are not suitable for evaluating metamorphic evolution due to their monotonous petrography and the pervasive overprinting of earlier mineral assemblages. However, within the same 'Ashchisu river pod' among minerals of the Cr-Spl (symplectite-bearing) peridotites and associated amphibolitized peridotites abundant relics of earlier mineral assemblages and microtextures have been preserved. However, on the basis of petrological observations alone it has not been possible to determine whether these different varieties of spinel-bearing ultramafic rocks recorded the same P-T history in their mineral assemblages or they were superposed at different stages of their metamorphic evolution.

#### 4.1.1. P-T conditions and P-T path.

Cr-Spl (symplectite-bearing) peridotites are characterized by two principal microtextural features, namely extensive Cpx-Opx-Spl and Amp-Spl symplectites and Opx rims (the COR's) around olivine. These features are well documented from studies in a number of metamorphosed ultramafic-mafic rocks massifs worldwide (e.g. Ulten zone, Italian Alps (Godard and Martin, 2000); Horoman Complex (Morishita and Arai, 2003); North Carolina Blue Ridge (Lang et al., 2004); Ugelvik Complex, Western Norway Gneiss region (Obata and Ozawa, 2011); San Juan Province, Argentina (Gallien et al., 2012); Moldanubian zone, Bohemian massif (Obata et al., 2012), etc.). Regardless of the source of the protoliths, the P-T-t paths of these massifs fall into two general scenarios. In the first a counterclockwise P-T-t path commences with a magmatic stage with crystallization of Ol – Pl, followed by cooling associated with granulite facies re-equilibration during which Opx coronas and Cpx-Spl symplectites form by reactions between Ol and Pl, then development of Amp-Spl symplectites during further re-equilibration at amphibolite

facies (Cruciani et al., 2008; Gallien et al., 2012; etc.). The rocks in this class of massifs are normally metatroctolites, formed at pressures that do not exceed 8 kbar for the whole P-T path. In the second scenario the P-T path is clockwise; a Grt – Ol assemblage forms at high pressures (the peak pressure varies considerably), followed by decompression with formation of COR's and pyroxene-spinel symplectites due to reactions between Grt and Ol, again followed by development of later Amp-Spl symplectite (Godard and Martin, 2000; Obata and Ozawa, 2011; etc.). Thus identification of the reactants responsible for symplectites + coronas growth is a crucial aspect for reconstruction of the metamorphic evolution and P-T paths.

In the Cr-Spl (symplectite-bearing) peridotites of the Zheltau massif, neither Pl nor Grt were unambiguously identified. Hence only indirect indications of their inferred prior presence have been used to reconstruct their metamorphic evolution. The salient observations and arguments are as follows:

- *Pyroxene-spinel (Px-Spl) symplectites comprise Cpx, Spl and Opx (Fig. 3, c; 8; Tables S2, S3, S4).* In numerous published cases where symplectites can be shown to have formed by the Ol-Pl reaction (e.g. Lang et al., 2004; Cruciani et al., 2008) the symplectites comprise Cpx with Al-Spl (± sapphirine) or Opx with Al-Spl (but not both Cpx and Opx) and subsequent Amp with Al-Spl resulting from hydration. In such cases the anhydrous assemblage comprising an Opx corona and the adjacent, separate Cpx-Spl symplectite is formed nearly simultaneously as a result of Mg (Fe) – Ca, Al diffusion along the reaction zones (Gallien et al., 2012); Al and Ca diffuse outward from Pl, comprising Spl and Cpx, whereas Mg is released by Ol to form the COR's. Mg diffusion rates are faster than those of Al and Ca, resulting in a symplectite (a diffusion-limited microstructure) rather than discrete, larger grains of these phases (Mongkoltip and Ashworth, 1983). However, in the Zheltau massif peridotites the earlier (anhydrous) symplectitic aggregates have *orthopyroxene* as an additional phase in association with Cpx and Al-Spl, together with well-developed Opx rims around olivine (Fig. 3, b; 4 b, f). This could indicate a higher chemical potential of Mg relative to Ca, which could not be provided by Pl, but

may instead have been contributed by garnet (e.g. Godard and Martin, 2000; Morishita and Arai, 2003; Obata, 2011), or perhaps Ca-Al-rich orthopyroxene (Field and Haggerty, 1994). In such cases the boundary between the COR and Px-Spl symplectite is considered to have been the initial boundary between Ol and the decomposed phase (e.g. garnet) (Obata, 2011).

- *Nodular Cr-rich spinel has a preferred textural location, assigned to the boundaries between the COR's and the symplectites (Fig. 4, b, f).* In possible contradiction to the hypothesis of a pre-existing Ol – Grt assemblage, the symplectite-bearing peridotites described here show only sparse contents of $Cr_2O_3$ in the anhydrous symplectite phases (Tables S2, S3, S4, S7). It is well known that relict Grt from (ultra-) high-pressure chromium-rich ultramafics is characterized by elevated $Cr_2O_3$ concentrations (1-3 wt.% in general (e. g. Godard and Martin, 2000; Obata et al., 2013)), therefore the pyroxene-spinel symplectites formed after garnet breakdown normally possess notable contents of $Cr_2O_3$ even in the absence of preserved garnet (e. g. the Horoman complex (Morishita and Arai, 2003)). Alternatively, the Cpx-Opx-Spl (± Amp) symplectites in the Zheltau peridotites show $Cr_2O_3$ values < 0.3 wt.% (Table S7). However, Cr- and Al-bearing phases, represented by zoned nodular spinel (Table S3) are, in most cases, intimately associated with the reaction fronts between the COR's and Cpx-Opx-Spl symplectites. Extensive amphibole development (expressed in later Amp-Spl symplectites) strongly obscures the direct contacts between the earlier COR's and pyroxene-spinel symplectites. Nevertheless, the cores of zoned nodular spinels with the highest chromium contents could be interpreted as resulting from a "sink" of Al and Cr away from the decomposed former Cr-Al-bearing reactant (i.e. garnet) (Obata, 2011). This is also confirmed by the well-described reaction of Cr-Grt + Ol = 2 Opx + Cr-Spl (Klemme, 2004). It should be noted that, in accordance with experimental data (Turkin and Sobolev, 2009; Turkin, 2011), the fast ascent of ultramafic masses through the garnet peridotite to spinel peridotite transition results in almost simultaneous reactions of garnet with olivine (followed by spinel and orthopyroxene production) as well as garnet breakdown by itself, leading to pyroxene-spinel symplectite development (also described in Obata, 2011).

- *Orthopyroxene constituting the COR's, is characterized by prominent zoning of Al and moderate zoning of Mg/(Mg+$Fe^{2+}$), with $Al_2O_3$ decreasing from the symplectite margin towards olivine and Mg# increasing in the same direction* (Fig. 7, c; Table S2). It is clearly observed from petrography that the COR's replace olivine, to an extent varying from a narrow shell at the rim to almost complete disappearance (Fig. 3, b), indicating the outward growth of Opx from the boundary with symplectite towards the olivine. The elevated $Al_2O_3$ contents at the boundaries with Px-Spl symplectites could have been controlled by grain boundary diffusion; olivine contains virtually no Al, therefore the former neighboring Al-rich mineral (plagioclase or garnet) must be considered as a source of Al for the CORs'. Lower diffusion rates of Al relative to Mg (Mongkoltip and Ashworth, 1983) indicate the "lagging" mobility of aluminum, therefore $Al_2O_3$ decreases towards to Ol, whereas Mg/(Mg+$Fe^{2+}$) shows slight increase closer to olivine. It is also significant that the COR's in many cases contain solid inclusions of Cr-rich spinel (Table S3), which could have contributed to element redistribution of the COR's, however, the derivation of such inclusions is controversial.

- *Cr-Spl exsolution lamellae in olivine indicate more aluminum and chromium olivine-precursor existence.* Olivine in the observed Cr-Spl (symplectite-bearing) peridotites exhibit relatively little serpentinization. They contain tiny oriented lamellaes of Cr-rich spinel (Fig.4, c). To the authors' knowledge these have never been described in low-pressure metatroctolites, whereas Song et al. (2004) interpreted Al-chromite exsolution in olivine to have been related to ultra-high pressure metamorphism. While this is not excluded by the observations presented here, such exsolution of high-charge cations ($Cr^{3+}$, $Fe^{3+}$) may be consistent with cooling and/or decompression from a wide range of prior medium-to-high-T conditions as temperature and pressure decrease (Ruiz Cruz et al., 1999).

The Zheltau massif Cr-Spl (symplectite-bearing) peridotites exhibit some instructive similarities with orogenic garnet peridotites in other orogenic belts. In the Ugelvik Complex (Norwegian Caledonides) and the Moldanubian Zone (Variscides, Czech Republic), which have

a complete absence of plagioclase, there is a geometric tendency of the fibrous pyroxene-spinel symplectites to grow orthogonally to the symplectitic "seams" (Fig. 4, b, f) (see Obata (2011), elsewhere). The key observations set out above along with similarities with known garnet peridotites elsewhere appear to favor the "clockwise P-T-t path scenario" in which the coronas around olivine relics result from reactions with garnet during decompression and/or cooling. Hence the ultramafic rocks apparently achieved garnet stability and were then drastically re-equilibrated with destruction of garnet by pervasive development of Cpx-Opx-Spl symplectites and Coarse Opx Rims. In this way Cr-Spl lamellae release could be considered as a response to P-T dropping during the retrogression, whereas solid inclusions of Cr-Spl in olivine (Fig. 4, a) could possibly represent minerals of the earlier, prograde stages of metamorphism.

4.1.2. Thermobarometry.

Based on the above observations of the Cr-Spl (symplectite-bearing) peridotites of the Zheltau massif, we attempted to constrain the P-T conditions of some stages of the metamorphic evolution. The main assessments were obtained using the Gibb's energy minimization method by means of pseudosections constructed using Perple_X software (version 6.7.3; Connolly (1990), Connolly (2005)) for calculated effective bulk compositions (EBC) (Fig. 10; 11, A). Careful estimation of the EBC is necessary because of the abundance reaction microtextures (e.g. coronas, symplectites) in the rocks, reflecting only local compositional equilibration on domainal scales. Therefore, two domains were chosen to calculate the EBCs and to model the reactions responsible for 1) Cr-Spl and the COR growth (Fig. 10); 2) Cpx-Opx-Spl symplectite formation (Fig. 11, A). Both EBCs were calculated by directly from mineral modes in the thin-section (using BSE SEM images) by measuring the area occupied by each visible phase and calculating the bulk composition by combining the mineral modes and converting them to mass fractions. The method of least squares (reviewed in Cruciani et al., 2008; Groppo et al., 2015) was ruled out owing to an absence of an accurate analysis of one of the reactants (i.e. garnet).

In the first case a mineral mode was estimated for a representative area of about 400 × 600 μm (including the inferred reactants (Ol, decomposed into symplectites Grt) and products (Cr-Spl and Opx (COR)), resulting in the indicated EBC for a Cr-bearing system (Fig. 10). Amphibole is considered to have grown during the later stages of retrogression, evidently forming after Cpx-Opx-Spl symplectites as a result of water ingress during exhumation (see Paragraph 2.1), therefore water was not added into the system components set. The second EBC was also obtained for an anhydrous system and includes Cpx, Opx and Spl from the symplectites for a small area (Fig. 8, a; Table S7), with extremely finely-intergrown mineral phases. As it was discussed earlier, such microtextures as Px-Spl symplectite and Opx coronas could be produced by reaction of either plagioclase + olivine or garnet + olivine. In this reason using indicated EBCs, plagioclase, olivine and garnet were included in the pseudosections in addition to Cpx, Opx and Spl.

The obtained pseudosections should be considered as satisfactory if 1) the pseudosection contains both the inferred reactants and products; 2) compositional isopleths of the products have an intersection, falling into a multivariate field, representing a transition between reactants and products; and 3) some microtextures of the chosen domains indicate contemporaneous formation (the terms are taken from Groppo et al. (2015)).

The lack of garnet restricts the choice of available conventional geothermobarometers. However, two-pyroxene geothermometry, based on Mg, Fe-Ca and Mg-Fe exchanges between Opx and Cpx in the symplectite was implemented (Fig. 11, B; the details are given hereafter).

4.1.2.1. Thermodynamic modeling.

Version 6.7.3 of Perple_X in conjunction with the internally consistent thermodynamic databases of 1) Holland and Powell (1998), Klemme et al. (2009) and Ziberna et al. (2013) for the system CaO-FeO-MgO-$Na_2O$-$Al_2O_3$-$SiO_2$-$Cr_2O_3$ (Fig. 10) and 2) Holland and Powell (1998) for CaO-FeO-MgO-$Na_2O$-$Al_2O_3$-$SiO_2$ system (Fig. 11, A) were used to construct two pseudosections. For the Cr-bearing system the following solution models were incorporated: O

(JH), Opx (JH) (both after Jennings and Holland, 2015), Cpx (HP) (Holland and Powell, 1996), CrSp, CrGt (both after Klemme et al., 2010). For the second, Cr-free system, the chosen solution models were Cpx (HP), Opx (HP) (Holland and Powell (1996)), Pl (h) (Newton et al., 1980) and Gt (HP), Sp (HP), O (HP) (Holland and Powell, 1998). Isopleths were plotted using PyWerami software (Lexa, 2011).

On Fig. 10 reaction between garnet and olivine with formation of Cr-spinel and Opx (transitional zone) is characterized by an expanding pressure interval with decreasing temperature. Since nodular Cr-Spl and Opx (the COR) display compositional zoning (paragraph 3.3.1), the compositional isopleths for the mineral modes reflect intervals of representative analyses rather than single-point measurements. For Cr-Spl with high $Cr_2O_3$ (more than 2 wt.%), (Cr/(Cr+Al) compositional isopleths are in the range of 0.02-0.45 (Fig. 10, a). For Opx the isopleths represent analyses from zones lying close to Ol and mantle parts of the COR's. ($Mg/(Mg+Fe_{tot})$ and Al (a.p.f.u.) compositional isopleths for Opx are in the ranges 0.865 – 0.88 and 0.03 – 0.08, respectively; Fig. 10, b, c). $Mg/(Mg+Fe_{tot})$ compositional isopleths of olivine in the range of 0.855 – 0.875 are also given (Fig. 10, d). The isopleth intervals (shown by yellow, purple, green, and pink colors on Fig. 10) overlap at 11.5 – 14.5 kbar; and wide temperature range of 580 – 800° C.

On Fig. 11 (A) compositional isopleths of Opx G1 ($X_{en}$ and $X_{al}$), Spl Y8 (Mg/(Mg+Fe)) and Cpx Y11 (Mg/(Mg+Fe)) (see Tables S2, S3, S4) fall into the narrow transitional zone, covering the pressure range of 11 – 13 kbar. Furthermore, the isopleths have a good intersection at P = 11.5-12 kbar; T = 750 – 870° C, indicating reaction of garnet breakdown with Cpx-Opx-Spl production at relatively high pressure conditions.

Both pseudosections (Fig. 10 and 11, A) are considered to have been of acceptable quality in accordance with the observed earlier terms of domainal modeling. From here, associations of Cr-Spl, COR's and Cpx-Opx-Spl symplectites were formed at P-T conditions, covering garnet to spinel peridotite transition (Klemme, 2004).

4.1.2.2. Conventional geothermobarometry.

Assuming nearly simultaneous formations of Opx and Cpx in the symplectite (Fig. 8, a), it is possible to conduct two-pyroxene geothermometry. On Fig. 11, B the lines of P-T dependencies after different authors (see the figure caption) show T = 650 - 750° C for a wide pressure range, taken from 11 to 20 kbar. Using of a conventional geobarometry is impermissible in the lack of preserved garnet. The amphibole geobarometers of Hammarstrom and Zen (1986), Hollister et al. (1987), Johnson and Rutherford (1989) and Schmidt (1992) applied to amphiboles from the later Amp-Spl symplectites yielded P = 8.2 – 10.5 kbar; the lack of plagioclase in one association with amphiboles restricts conduction of amphibole geothermometry.

4.2. Geochemical affinity of the ultramafic rocks.

In contrast to the petrological observations, the whole-rock geochemistry of *all* of the ultramafic varieties is representative enough to deduce their geochemical affinity and possible settings of formation. The structural position of the studied ultramafic rocks, located within 'Ashchisu river pod', as well as their closely similar geochemical characteristics (expressed in their REE and multielement distribution patterns) imply a common provenance of these rocks (the only exception is the intensively rodingitizied sample AH 1511 with high LREE values; however, in thin-section the relics of the symplectites are preserved and the rock is certainly not extraneous) (Fig. 6, A, B). A common origin is also indicated by well-defined element covariations (Fig. 5), which tend to follow a single trend.

On the other hand, the strong metamorphic and metasomatic alterations of the rocks demands caution when making arguments about their derivation and origin.

The major element distributions of the spinel-bearing ultramafic rocks are characterized by moderate $Mg/(Mg+Fe_{tot})$ in the range of 0.78 – 0.83; olivine from the rocks shows moderate values of $Mg/(Mg+Fe_{tot})$ as well (0.85 – 87). The rocks are enriched in fertile components (Al, Ca) to varying degrees, whereas contents of highly compatible elements (Cr, Ni) are not very high (402 – 3114 ppm; 1085 – 2240 ppm, respectively). These features are typical for ultramafic

rocks originated from mantle-derived melts, which were emplaced into lower crust and contaminated by the components of crustal rocks (i. e. “crustal type” of the ultramafic rocks (Carswell et al., 1983; Reverdatto et al., 2008; Zhang et al., 2011)). However, the trace element distribution shows strong depletion in REE, Nb, Zr, Hf and Y contents, which is consistent with residual mantle values. On Fig. 12 (A, B) representative patterns of well-studied “mantle”-type (Zhimafang complex, Dabie-Sulu; Almklovdalen complex, Western Gneiss Region) and “crustal”- type (Bixiling complex, Dabie Mountains; Kokchetav massif) garnet and spinel peridotites are plotted. It can be seen that ultramafic rocks of the Zheltau massif are completely different from the “crustal-type” garnet peridotites of the Bixiling complex or Kokchetav massif (which tend to be much more enriched in REE), but they show the lower values than depleted MORB mantle (DMM).

On the other hand, the studied rocks possess considerable differences from mantle wedge garnet peridotites of the Zhimafang and Almklovdalen complexes as well; the rocks manifest distinct spoon-shaped (or smoothly U-shaped) form of the REE patterns with prominent positive Eu anomalies (Fig. 6, A or 12, A), complementary to Sr peaks (Fig. 6, B). This could be a result of the progressive fractionation of certain minerals from a parental melt (Janák et al., 2006; Godard et al., 2009), and in this way Eu anomalies could indicate plagioclase accumulation. This is also, to some extent, confirmed by positive correlations between Sr, Eu and normative plagioclase in the rocks (Fig. 5).

The element patterns of the Zheltau massif ultramafic rocks bear a strong resemblance to the cumulate sequences of the Atlantis massif on Middle Atlantic Ridge (Fig. 6, A) and the South Sandwich arc-basin system (Fig. 12, A), which are clearly different from mantle residual harzburgites (Fig. 6, A; grey area). Nonetheless, it should be noted that refertilized residual mantle peridotites may not be ruled out as possible protolith for the studied rocks. Low contents of HREE in the rocks, compared to DMM ($Lu/Lu^* = 0.09 – 0.17$; $Yb/Yb^* = 0.06 – 0.15$), are consistent with residual MORB mantle compositions for 15-20 % of melt extraction (after Pearce

and Parkinson, 1993). In this case the observed spoon-shaped form of the chondrite-normalized patterns (Fig. 6, A - yellow zone (Paulick et al., 2006)) is thought to have been related to an interaction of LREE-depleted residual mantle with LREE-enriched melts (Pearce et al., 2000). In such a scenario the observed Eu anomalies could have resulted from plagioclase precipitation from percolating Ca-Al-rich basaltic melts (Müntener et al., 2010). However, the relatively low contents of highly and moderately compatible elements (Cr, Ni, Mg) compared to residual mantle, as well as the progressive character of Eu anomalies, correlating with normative-Pl contents (Fig. 5; Table 1), imply that a cumulate origin for the Zheltau massif rocks is more likely.

Inferring a plagioclase-bearing (shallow) crustal protolith for the spinel-bearing peridotites of the Zheltau massif and taking into account their highly depleted chemical characteristics, it is more likely that they have been derived from partial melts of suboceanic rather than subcontinental mantle. Subcontinental mantle-derived cumulates would be characterized by considerably more enriched whole-rock geochemical fingerprints (e.g. Rizhao complex; Fig. 12, A). Besides, among the ultramafic rocks of the studied 'Ashchisu river pod' (Fig. 2, A) *mafic* varieties with similar depleted REE and multielement distribution patterns (Fig. 13; Table S1) are present. The latter could be also considered as metamorphosed fragments of the upper, mafic parts of a sub-oceanic cumulative sequence with a high modal content of plagioclase (Fig. 14).

On the basis that the protolith for the ultramafic (and mafic) rocks of the Zheltau massif was an oceanic cumulate complex, the geodynamic environment of its formation may be inferred in the light of their geochemical signatures and field observations. The rocks demonstrate an enrichment by highly incompatible (HIE) and mobile elements (Cs, Rb, Ba, Pb, Sr) and have clear negative Nb anomaly, which are often considered as a fingerprints of supra-subduction zone (SSZ) magmatism (as a result of fluid action during subduction (e.g. Pearce et al., 1984; Jahn, 1998)). Fig. 13 (A, B) shows compositions for rocks from the SSZ Marum ophiolite cumulative complex (from Pl-bearing peridotite through wherlite and gabbro to diorite).

Serpentinites and amphibolitized gabbroids of the NE part of the Koyandy complex, Zheltau massif (Fig. 2, A), are also depicted. It is clear that the patterns of both suites are very similar. Furthermore, serpentinites and gabbroids of the NE part of the Koyandy complex also possess suprasubductional geochemical signatures (HIE and mobile elements enrichment, negative Nb anomaly; Fig. 13, B; Table S1). Giving that the gabbroids are nearly unmetamorphosed, but have the direct boundary with the Koyandy metamorphic complex and display multielement distribution patterns, similar to those described in the strongly metamorphosed spinel-bearing ultramafic rocks and chloritized mafic lithologies (Fig. 13, B), these evidently could be considered as upper parts of the ophiolitic sequence, remained at a structurally high level and obducted onto the microcontinent after oceanic basin closure, whereas the lower part of the oceanic sequence was detached and subducted up to at least HP conditions with following spinel- and garnet peridotites formation (Paragraph 4.3 in the following).

On the other hand, the indicated "SSZ-type" geochemical signatures of metamorphosed and unmetamorphosed ultramafic/mafic rocks of the Zheltau massif could be acquired as a result of invading by continental crust-derived fluids of the rocks, formed in a Middle Oceanic Ridge (MOR) rather than SSZ setting. Thus, an enrichment in LILE of the studied metamorphosed spinel-bearing ultramafic rocks and chloritized mafic rocks could be resulted from metasomatic effects during their exhumation. Metasomatism, in turn, could be related to interaction of the studied rocks with granitoid melts resulting from partial melting of associated silicic gneisses. In this case the LILE enrichment and negative Nb anomaly of the unmetamorphosed gabbroids could have resulted from contamination by crustal fluids during obduction onto the continental margin (Bodinier and Godard, 2003) after the basin closure. This is also partly supported by the elements pattern in Co-Sc-Al*4 diagram from which the crystallization sequence may be inferred (Fig. 14) (Pearce et al., 2011; Pearce, pers. comm., 2017). The samples follow the anticlockwise ('MOR-type') succession. However, in such a scenario protoliths would have experienced strong serpentinization by seafloor hydrothermal activity. In this case prograde

metamorphism with serpentine dehydration would produce olivine for the observed whole-rock compositions with Mg# of about 90-91 (Merkulova et al., 2017), which is not applicable for the studied formations (Table S2).

In summary, the balance of evidence suggests that ultramafic rocks in the Zheltau massif were formed in a suprasubduction setting and represent Pl peridotites – Ol-rich troctolites – gabbroids of the arc-basin cumulative sequence. This is consistent with the extreme rarity of preserved MOR-type ophiolites worldwide; the similarity of geochemical signatures of the Zheltau massif ultramafic/mafic rocks with SSZ-type ophiolitic cumulate sequences like the Marum complex in Papua New Guinea (Fig. 13); the correspondence of the Zheltau ultramafic/mafic rock compositions in the La-Nb-Y discriminant diagram with a wide range of settings from N-MORB to E-MORB and arc-related settings (Fig. S3). With spreading progressing, part of the sequence was obducted onto the continental margin, whereas most of the complex was tectonically buried to conditions in the garnet stability field under the microcontinent, and afterwards was exhumed with formation of the characteristic Cpx-Opx-Spl symplectites and Opx coronas around olivine at higher pressures and subsequent amphibolite-facies metamorphism. Rodingitization in turn seems to have appeared on the latest stages of the ultramafic rocks evolution, perhaps after the rocks were emplaced in the continental crust.

### 4.3. Geotectonic implications.

The geochemical and petrological characteristics of ultramafic-mafic metamorphic complexes of the Zheltau massif presented here, along with previous studies in adjacent lithotectonic units, allows distinction of two types of HP complexes, namely:

1) Eclogites and garnet clinopyroxenites of “crustal” type with enriched geochemical characteristics, the protoliths of which are derivatives of intraplate tholeiitic melts intruded into continental crust prior to subduction (Alexeiev et al., 2011; Pilitsyna et al., 2018);

2) Spinel-bearing peridotites of cumulate origin, derived from a depleted mantle source (this study).

High-pressure metamorphism in this region has commonly been associated with closure of the Dzhalair-Naiman oceanic basin, followed by collision of the adjacent Chu-Kendyktas and Zheltau continental massifs (e.g. Alexeiev et al., 2011; Kröner et al., 2012; Klemd et al., 2014). However, on the basis of the structural positions of the ophiolites in this region as well as tectonic architecture of the Precambrian and Early Paleozoic complexes in Southern Kazakhstan and Northern Tien Shan, it is possible to suggest an alternative evolutionary model of the region during Cambrian and Early Ordovician. Cambrian ophiolites of the Dzhalair-Naiman zone and ophiolites within the NE part of the Zheltau massif (Fig. 1, B and 2, A) are clearly spatially separated by the intervening Precambrian metamorphic complexes, mostly comprising the Zheltau massif (Fig. 2, A). Therefore, we consider these ophiolites to be fragments of lithosphere of the different oceanic basins, which have experienced different tectonic evolutions.

Following Kröner et al. (2012), and taking into account similarities of the rift-related Neoproterozoic felsic rocks of the massifs (Tretyakov et al., 2016a; Tretyakov et al., 2016b) framing the Dzhalair-Naiman ophiolite zone, we propose that this oceanic basin opened in the late Ediacaran – early Cambrian. From the NE this basin was framed by the Zheltau microcontinent, and from the SW it was bounded by the Chu-Kendyktas microcontinent (in the present-day coordinates). Chemical compositions, ages and structures of the Precambrian complexes of the Chu-Kendyktas massif are significantly different from those described in the Northern Tien Shan (Issyk-Kul) massif, which is attributed to another group of Precambrian terranes in the Western part of the CAOB (Degtyarev et al., 2017). In the NE part of the Zheltau continent there was a *different* oceanic basin, bounded by the Aktau-Yili microcontinent (Fig. 15). On the basis of stratigraphic evidence, the emergence of this basin apparently took place during the late Ediacaran to early Cambrian, although the ages of these ophiolite fragments have not been determined.

The oldest ophiolitic rocks, indicating the earliest stages of oceanic crust formation, are early Cambrian ca. 531±4 Ma metagabbro of the Kopurelisay complex in the Aktyuz area, which

represent fragment of oceanic crust of the Dzhalair-Naiman basin obducted onto the Chu-Kendyktas (North Tianshan) microcontinent (Kröner et al., 2012). It is suggested that fast opening of the Dzhalair-Naiman and other oceanic basins of Southern Kazakhstan and Northern Tien Shan took place in the Early Cambrian as a result of the active spreading processes. At the same time within the Chu-Kendyktas and Aktau-Yili microcontinents the accumulation of a terrigenous, carbonate and shale cover was initiated (Fig. 15, a).

In the middle Cambrian (~ 520 Ma), within the Dzhalair-Naiman oceanic basin, SSZ ophiolites started to form; the upper parts of these ophiolites are represented by gabbro-tonalite-plagiogranite complexes as well as a bimodal basalt-rhyolite series (Ryazantsev et al., 2009a; Degtyarev, 2012). These complexes are considered to have been formed during the back-arc rifting in the rear part of an ensimatic island arc, whose crust was almost completely replaced by rift-related intrusions. In the oceanic basin dividing the Zheltau and Aktau-Yili microcontinents, spreading was proceeding and subduction under the Aktau-Yili microcontinent was initiated. Within the Chu-Kendyktas and Aktau-Yili microcontinents the accumulation of terrigenous, carbonate and shale covers continued (Fig. 15, b).

In the middle-to-late Cambrian (~ 510-500 Ma) the Sulusay ensimatic island arc emerged within the Dzhalair-Naiman oceanic basin. These arc complexes are composed mainly of tuffs with rare flows of intermediate-felsic lavas (Ryazantsev et al., 2009a; Degtyarev, 2012). In the back part of this island arc spreading occurred and the siliciclastic-carbonate-basaltic Ashchisu formation was accumulating during the middle-late Cambrian (Ryazantsev et al., 2009b). Geochemical characteristics of basalts of the Ashchisu formation display different sources (e.g. N-MORB, E-MORB or suprasubductional island-arc tholeiites), which is indicative of back-arc basalts (Degtyarev, 2012). Subduction of the oceanic basin between the Zheltau and Aktau-Yili microcontinents continued and the ensimatic island arc started to emerge. An ensialic island arc within the marginal part of the Aktau-Yili microcontinent was also formed. This is now represented by unmetamorphosed middle Cambrian granodiorites and granites, located in the NE

part of the Zheltau massif (Alexeiev et al., 2011), whereas complexes of the ensimatic island arc are represented by unmetamorphosed amphibolitized gabbroids (this study; Fig. 2, A; Table S1). On the margin of the Chu-Kendyktas microcontinent, siliciclastic and carbonate facies accumulated, whereas a back-arc area of the Aktau-Yili microcontinent experienced intense subsidence and was dominated by deeper marine shales and turbidite facies (Fig. 15, c).

In the late Cambrian-Early Ordovician (~ 490-485 Ma), obduction of the ultramafic-mafic complexes of the Dzhalair-Naiman zone onto the Chu-Kendyktas massif took place, accompanied by formation of a number of allochthons (e.g. Kopurelisay complex of the Aktyuz block). In the early Tremadocian (~ 485 Ma) these allochthons started to erode and pebbles of ophiolitic gabbro and serpentinites were deposited in siliciclastic facies of the Kendyktas formation (Ryazantsev et al., 2009b). The Dzhalair-Naiman oceanic basin started to shrink and accreted ophiolitic complexes and deeper marine deposits were overlain by turbidites of the early Tremadocian Dzhambul formation. The ages of detrital zircons from sandstones of the Dzhambul formation indicate that the turbidites were derived from Precambrian crustal blocks (Kröner et al., 2007). At the same time the oceanic basin between the Zheltau and Aktau-Yili microcontinents finally closed and some parts of the ultramafic-mafic complexes of ensimatic arc-basin system (serpentinite and gabbro) were obducted onto the Aktau-Yili microcontinent, whereas most of the sequence as well as fragments of the Zheltau microcontinent crust (the Koyandy complex) were buried under the Aktau-Yili microcontinent to the depths of 60-70 km, where eclogites, garnet clinopyroxenites and studied spinel-bearing ultramafic rocks were formed (Fig. 15, d).

In the Early Ordovician (~ 480-475 Ma) the Dzhalair-Naiman oceanic basin was completely closed and a suture zone was formed composed of folded Cambrian ophiolites and island-arc complexes as well as the Early Ordovician flyshoid Dzhambul formation. Fragments of the Chu-Kendyktas microcontinental crust were buried under the Zheltau microcontinent to the depths of 70-75 km, where HP metamorphism with formation of eclogites and their

subsequent exhumation occurred (the Aktyuz complex). Within the suture zone dividing the Zheltau and Aktau-Yili microcontinents, high-pressure complexes were also exhumed (Fig. 15, e) (Pilitsyna et al., 2018; this study).

## 5. Conclusions.

1. In the Koyandy complex (Zheltau massif, Central Asian Orogenic Belt) spinel-bearing ultramafic lithologies, comprising a single tectonic pod among strongly retrogressed kyanite-bearing paragneisses, are represented by magnetite-bearing serpentinites, Cr-spinel-bearing serpentinized dunites, Cr-spinel symplectite-bearing peridotites and amphibolitized peridotites. Among the ultramafic spinel-bearing rocks, intensively chloritized and serpentinized *mafic* varieties are also present. All these lithologies have been undergone variable degrees of late-stage rodingitization.

2. Cr-spinel (symplectite-bearing) peridotites contain distinctive Cpx-Opx-Spl symplectites together with Opx coronas around olivine. The microtextures are interpreted to have been formed as a result of two nearly simultaneous reactions, namely a) Grt – Ol reaction and b) garnet breakdown by itself. P and T of symplectite formation (P ~ 11.5 – 14.5 kbar; T ~ 600 – 850° C) correspond to the transition from garnet to spinel peridotites. The subsequent retrogression is expressed in the extensive development of amphibole.

3. Trace element distributions in these rocks indicate that their protoliths were probably plagioclase-bearing (i.e. shallow) magmatic cumulates including Pl ultramafic rocks and troctolites, which were subducted to eclogite facies conditions and then exhumed along with the other metamorphic complexes of the Zheltau massif.

4. The whole-rock geochemistry of the spinel-bearing ultramafic rocks is consistent with their derivation from melts sourced in depleted mantle within a suprasubduction geodynamic setting. Mafic metamorphic varieties sharing a single pod with the Spl-bearing ultramafic rocks are considered to have been plagioclase-rich members of the same subducted SSZ-type cumulative sequence. In this scenario unmetamorphosed gabbroids in lithotectonic units

bounding the metamorphic complexes, are thought to represent an obducted part of the same arc-basin system which had, therefore escaped tectonic burial and HP metamorphism.

5. The spinel-bearing ultramafic rocks are clearly different from eclogites and garnet clinopyroxenites in this region, which are derivatives of intraplate tholeiitic melts introduced into continental crust prior to subduction, and are also present among the metamorphic complexes of the Koyandy complex (Zheltau massif). The spinel ultramafic rocks evidently do not represent fragments of the extracted from a mantle wedge, but instead represent metamorphosed crustal cumulates that show distinctly depleted geochemical signatures, which are clearly different from the well-known UHP garnet and spinel peridotites of the Kokchetav massif. The Cr-Spl symplectite-bearing peridotites are the first to be described from the western part of the CAOB.

**Acknowledgments.**

A.P. kindly thanks Chiara Groppo and James Connolly for their recommendations and help in pseudosection modeling. Pavel Plechov, Atali Agakhanov, Nikolay Karmanov and Kirill Ponkratov are also thanked for providing techniques and their good help. The authors are grateful to Dmitry Alexeiev for his constructive criticism of the geological part of the paper. Andrey Vishnevsky is especially thanked for the timely vuagnatite and niigataite identifications. A.P. is particularly grateful to professor Masaaki Obata for his useful advice, recommendations and sincere attention to petrological aspects of the article. An anonymous reviewer is also warmly thanked for reasonable remarks that promoted reconsideration of many issues relating to the petrogenesis of the studied rocks. We thank Associate Editor T. Tsunogae and Editor-in-Chief M. Santosh for their valuable comments on the organization of the manuscript. Analytical procedures for the study were funded by research project № 14-27-00058 of the Russian Science Foundation. The study was also funded by the research project of RFBR № 18-35-00199.

**References.**

Abdulin, A.A., Volkov, V.M., Scherba, G.N., 1980. Chu-Yili Belt. Geology of the Chu-Yili region. Alma-Ata, NAUKA, 504 p. (in Russian).

Alexeiev, D. V., Ryazantsev, A. V., Kröner, A., Tretyakov, A.A., Xia, X., Liu, D.Y., 2011. Geochemical data and zircon ages for rocks in a high-pressure belt of Chu-Yili Mountains, southern Kazakhstan: Implications for the earliest stages of accretion in Kazakhstan and the Tianshan. Journal of Asian Earth Sciences 42, 805–820. https://doi.org/10.1016/j.jseaes.2010.09.004.

Barnes, S.J., Roeder, P.L., 2001. The Range of Spinel Compositions in Terrestrial Mafic and Ultramafic Rocks. Journal of Petrology 42, 2279–2302. https://doi.org/10.1093/petrology/42.12.2279.

Beyer, E.E., Griffin, W.L., O'Reilly, S.Y., 2006. Transformation of Archaean lithospheric mantle by refertilization: Evidence from exposed peridotites in the Western Gneiss Region, Norway. Journal of Petrology 47, 1611–1636. https://doi.org/10.1093/petrology/egl022.

Bilgrami, S.A., Howie, R.A., 1960. The mineralogy and petrology of a rodingite dike, Hindubagh, Pakistan. American Mineralogist 45, 791–801.

Biryukov, V.M., 1988. High-pressure complexes of the fold-and-thrust belts. NAUKA, Moscow, 208 p. (in Russian).

Bodinier, J.L., Godard, M., 2013. Orogenic, Ophiolitic, and Abyssal Peridotites, Treatise on Geochemistry: Second Edition. https://doi.org/10.1016/B978-0-08-095975-7.00204-7.

Brey, G.P., Kohler, T., 1990. Geothermobarometry in 4-phase lherzolites .2. New thermobarometers, and practical assessment of existing thermobarometers. Journal of Petrology 31, 1353–1378. https://doi.org/10.1093/petrology/31.6.1353.

Brueckner, H.K., Medaris, L.G., 2000. A general model for the intrusion and evolution of 'mantle' garnet peridotites in high-pressure and ultra-high-pressure metamorphic terrains. Journal of metamorphic geology 18, 123 – 133. 10.1046/j.1525-1314.2000.00250.x.

Cabanis, B., Lecolle, M., 1989. Le diagramme La/10-Y/15-Nb/8: Un outil pour la discrimination des series volcaniques et lamise en evidence des processus demelange et/ou de contamination crustale. Compte Rendus de I'Académie des Sciences Series II 309, 2023–2029.

Carswell, D.A., Harvey, M.A., Al-Samman, A., 1983. The Petrogenesis of constraining Fe-Ti and Mg-Cr garnet peridotite types in the high grade gneiss complex of Western Norway. Bulletin of the Mineral Research and Exploration 106, 727–750.

Chavagnac, V., Jahn, B., 1996. Coesite-bearing eclogites from the Bixiling Complex, Dabie Mountains, China: Sm-Nd ages, geochemical characteristics and tectonic implications. Chemical Geology 133, 29–51. https://doi.org/10.1016/S0009-2541(96)00068-X.

Connolly, J.A.D., 1990. Multivariable phase-diagrams: an algorithm based on generalized thermodynamics. American Journal of Science 290, 666 – 718. 10.2475/ajs.290.6.666.

Connolly, J.A.D., 2005. Computation of phase equilibria by linear programming: A tool for geodynamic modeling and its application to subduction zone decarbonation. Earth and Planetary Science Letters 236, 524–541. https://doi.org/10.1016/j.epsl.2005.04.033.

Craw, D., Landis, C.A., Kawachi, Y., 1979. Vuagnatite in new zealand (Note). New Zeal. Journal of Geology and Geophysics 22, 627–629. https://doi.org/10.1080/00288306.1979.10424172.

Cruciani, G., Franceschelli, M., Groppo, C., Brogioni, N., Vaselli, O., 2008. Formation of clinopyroxene + spinel and amphibole + spinel symplectites in coronitic gabbros from the Sierra de San Luis (Argentina): A key to post-magmatic evolution. Journal of metamorphic geology 26, 759–774. https://doi.org/10.1111/j.1525-1314.2008.00786.x.

Degtyarev, K.E., 2012. Tectonic evolution of Early Paleozoic island-arc systems and formation of Caledonides continental crust in Kazakhstan. GEOS, Moscow, 289 p. (in Russian).

Degtyarev, K., Yakubchuk, A., Tretyakov, A., Kotov, A., Kovach, V., 2017. Precambrian geology of the Kazakh Uplands and Tien Shan: An overview. Gondwana Research 47, 44–75. https://doi.org/10.1016/j.gr.2016.12.014.

Dobretsov, N.L., Sobolev, N.V., Shatsky, V.S., Aschepkov, A.B., Bakirov, A.B., Gabov, N.F., et al., 1989. Eclogites and glaucophane-bearing schists of the folded areas. NAUKA, Novosibirsk, 236 p. (in Russian).

Droop, T. R. G., 1987. A General Equation for Estimating Fe3+ Concentrations in Ferromagnesian Silicates and Oxides from Microprobe Analyses, Using Stoichiometric Criteria. Mineralogical Magazine 51, 431–435. https://doi.org/10.1180/minmag.1987.051.361.10.

Ernst, W.G., Mosenfelder, G.L., Leech, M.L., Liu, J., 1998. H2O recycling during continental collision: Phase-equilibrium and kinetic considerations. In: Hacker B.R. and Liou J.G. (Eds.), When Continents Collide: Geodynamics and Geochemistry of Ultrahigh-Pressure Rocks: Dordrecht, Kluwer Academic Publishers, 275 – 295.

Ernst, W., Hacker, B., Liou, J., 2007. Petrotectonics of ultrahigh-pressure crustal and upper-mantle rocks -- Implications for Phanerozoic collisional orogens. Sears, J.W., Harms, T.A., Evenchick, C.A., eds., Whence Mt. Inq. into Evol. Orog. Syst. A Vol. Honor Raymond A. Price Geol. Soc. Am. Specia Pap. 433, 27–49. https://doi.org/10.1130/2007.2433(02).

Field, S.W., Haggerty, S.E., 1994. Symplectites in upper mantle peridotites: Development and implications for the growth of subsolidus garnet, pyroxene and spinel. Contributions to Mineralogy and Petrology 118, 138–156. https://doi.org/10.1007/BF01052865.

Flanagan, F.J., 1967. U.S. Geological Survey silicate rock standards. Geochimica et Cosmochimica Acta 31 (3), 289-308. https://doi.org/10.1016/0016-7037(67)90043-9.

Gallien, F., Mogessie, A., Hauzenberger, C.A., Bjerg, E., Delpino, S., Castro De Machuca, B., 2012. On the origin of multi-layer coronas between olivine and plagioclase at the gabbro-granulite transition, Valle Fértil-La Huerta Ranges, San Juan Province, Argentina. Journal of metamorphic geology 30, 281–302. https://doi.org/10.1111/j.1525-1314.2011.00967.x.

Godard, G., Martin, S., Prosser, G., Kienast, J.R., Morten, L., 1996. Variscan migmatites, eclogites and garnet-peridotites of the Ulten zone, Eastern Austroalpine system. Tectonophysics 259, 313–341. https://doi.org/10.1016/0040-1951(95)00145-X.

Godard, G., Martin, S., 2000. Petrogenesis of kelyphites in garnet peridotites: A case study from the Ulten zone, Italian Alps. Journal of Geodynamics 30, 117–145. https://doi.org/10.1016/S0264-3707(99)00030-7.

Godard, M., Lagabrielle, Y., Alard, O., Harvey, J., 2008. Geochemistry of the highly depleted peridotites drilled at ODP Sites 1272 and 1274 (Fifteen-Twenty Fracture Zone, Mid-Atlantic Ridge): Implications for mantle dynamics beneath a slow spreading ridge. Earth and Planetary Science Letters 267, 410–425. https://doi.org/10.1016/j.epsl.2007.11.058.

Godard, M., Awaji, S., Hansen, H., Hellebrand, E., Brunelli, D., Johnson, K., Yamasaki, T., Maeda, J., Abratis, M., Christie, D., Kato, Y., Mariet, C., Rosner, M., 2009. Geochemistry of a long in-situ section of intrusive slow-spread oceanic lithosphere: Results from IODP Site U1309 (Atlantis Massif, 30°N Mid-Atlantic-Ridge). Earth and Planetary Science Letters 279, 110–122. https://doi.org/10.1016/j.epsl.2008.12.034.

Groppo, C., Rolfo, F., Liu, Y.C., Deng, L.P., Wang, A.D., 2015. P-T evolution of elusive UHP eclogites from the Luotian dome (North Dabie Zone, China): How far can the thermodynamic modeling lead us? Lithos 226, 183–200. https://doi.org/10.1016/j.lithos.2014.11.013.

Hammarstrom, J.M., Zen, E., 1986. Aluminum in hornblende: an empirical igneous geobarometer. American Mineralogist 71, 1297–1313.

Hegner, E., Klemd, R., Kröner, A., Corsini, M., Alexeiev, D. V., Iaccheri, L.M., Zack, T., Dulski, P., Xia, X., Windley, B.F., 2010. Mineral ages and P-T conditions of late Paleozoic high-pressure eclogite and provenance of mélange sediments from Atbashi in the south Tianshan orogen of Kyrgyzstan. American Journal of Science 310, 916–950. https://doi.org/10.2475/09.2010.07.

Holland, T.J.B., Powell, R., 1996. Thermodymanics of ORder-Disorder in Minerals. 2. Symmetric Formulism Applied to Solid Solutions. American Mineralogist 81, 1425–1437.

Holland, T.J.B., Powell, R., 1998. An internally consistent thermodynamic data set for phases of petrological interest. Journal of metamorphic geology 16, 309–343. https://doi.org/10.1111/j.1525-1314.1998.00140.x.

Hollister, L.S., Grissom, G.C., Peters, E.K., Stowell, H.H., Sisson, V.B., 1987. Confirmation of the empirical correlation of Al in hornblende with pressure of solidification of calc-alkaline plutons. American Mineralogist 72, 231–239.

Irvine, T.N., Baragar, W.R.A., 1971. A Guide to the Chemical Classification of the Common Volcanic Rocks. Canadian Journal of Earth Sciences 8, 523–548. https://doi.org/10.1139/e71-055.

Jahn, B.-M., 1998. Geochemical and isotopic characteristics of UHP eclogites of the Dabie orogen: implications for continental subduction and collisional tectonics. In: Hacker, B.R. and Liou, J.G. (Eds.), When Continents Collide: Geodynamics and Geochemistry of Ultrahigh-Pressure Rocks: Dordrecht, Kluwer Academic Publishers, 275 – 295.

Jaques, A.L., Chappell, B.W., Taylor, S.R., 1983. Geochemistry of cumulus peridotites and gabbros from the Marum ophiolite complex, northern Papua New Guinea. Contributions to Mineralogy and Petrology 82, 154–164. https://doi.org/10.1007/BF01166610.

Janák, M., Froitzheim, N., Vrabec, M., Krogh Ravna, E.J., De Hoog, J.C.M., 2006. Ultrahigh-pressure metamorphism and exhumation of garnet peridotite in Pohorje, Eastern Alps. Journal of metamorphic geology 24, 19–31. https://doi.org/10.1111/j.1525-1314.2005.00619.x.

Jennings, E.S., Holland, T.J.B., 2015. A simple thermodynamic model for melting of peridotite in the system NCFMASOCr. Journal of Petrology 56, 869–892. https://doi.org/10.1093/petrology/egv020.

Johnson, M.., Rutherford, M.J., 1989. Experimental calibration of the aluminium-in-hornblende geobarometer with application to Long Valley caldera. Geology 17, 837–841. https://doi.org/10.1130/0091-7613(1989)017<0837:ecotai>2.3.co;2.

Katayama, I., Maruyama, S., Parkinson, C.D., Terada, K., Sano, Y., 2001. Ion micro-probe U-Pb zircon geochronology of peak and retrograde stages of ultrahigh-pressure metamorphic rocks from the Kokchetav massif, northern Kazakhstan. Earth and Planetary Science Letters 188, 185–198. https://doi.org/10.1016/S0012-821X(01)00319-3.

Klemd, R., Hegner, E., Bergmann, H., Pfänder, J.A., Li, J.L., Hentschel, F., 2014. Eclogitization of transient crust of the Aktyuz Complex during Late Palaeozoic plate collisions in the Northern Tianshan of Kyrgyzstan. Gondwana Research 26, 925–941. https://doi.org/10.1016/j.gr.2013.08.018.

Klemd, R., Gao, J., Li, J.L., Meyer, M., 2015. Metamorphic evolution of (ultra)-high-pressure subduction-related transient crust in the South Tianshan Orogen (Central Asian Orogenic Belt): Geodynamic implications. Gondwana Research 28, 1–25. https://doi.org/10.1016/j.gr.2014.11.008.

Klemme, S., 2004. The influence of Cr on the garnet-spinel transition in the Earth's mantle: Experiments in the system MgO-Cr2O3-SiO2 and thermodynamic modelling. Lithos 77, 639–646. https://doi.org/10.1016/j.lithos.2004.03.017.

Klemme, S., Ivanic, T.J., Connolly, J.A.D., Harte, B., 2009. Thermodynamic modelling of Cr-bearing garnets with implications for diamond inclusions and peridotite xenoliths. Lithos 112, 986–991. https://doi.org/10.1016/j.lithos.2009.05.007.

Kotková, J., 2007. High-pressure granulites of the Bohemian Massif: Recent advances and open questions. Journal of Geosciences 52, 45–71. https://doi.org/10.3190/jgeosci.006.

Kröner, A., Windley, B.F., Badarch, G., Tomurtogoo, O., Hegner, E., Jahn, B.M., Gruschka, S., Khain, E.V., Demoux, A., Wingate, M.T.D., 2007. Accretionary growth and crust formation in the Central Asian orogenic belt and comparison with the Arabian–Nubian shield. in "4-D Framework of Continental Crust", Hatcher, R.D., Carlson, M.P., McBride, J.H., Martínez, Catalán, J.R. (Eds.), Geological Society of America Memoirs, 181–209. https://doi.org/10.1130/2007.1200(11).

Kröner, A., Alexeiev, D. V., Hegner, E., Rojas-Agramonte, Y., Corsini, M., Chao, Y., Wong, J., Windley, B.F., Liu, D., Tretyakov, A.A., 2012. Zircon and muscovite ages, geochemistry, and Nd-Hf isotopes for the Aktyuz metamorphic terrane: Evidence for an Early Ordovician collisional belt in the northern Tianshan of Kyrgyzstan. Gondwana Research 21, 901–927. https://doi.org/10.1016/j.gr.2011.05.010.

Kushev, V.G., Vinogradov, D.P., 1978. Metamorphogenic eclogites. NAUKA, Novosibirsk, 112 p. (in Russian).

Lang, H.M., Wachter, A.J., Peterson, V.L., Ryan, J.G., 2004. Coexisting clinopyroxene/spinel and amphibole/spinel symplectites in metatroctolites from the Buck Creek ultramafic body, North Carolina Blue Ridge. American Mineralogist 89, 20–30. https://doi.org/10.2138/am-2004-0104.

Leake, B.E., Wooley, A.R., Arps, C.E., et al., 1997. Nomenclature of amphiboles: report of the subcommittee on amphiboles of the international mineralogical association, commission on new minerals and mineral names. The Canadian Mineralogist 35, 219-246.

Lexa, O., 2011. PyWerami: countour/3D plotting program for Perple_X WERAMI data (Version 2.0.1) [Software]. Available from http://petrol.natur.cuni.cz/~ondro/pywerami:home.

Li., X.P., Zhang, L.F., Wang, Z.L., 2008. Geochemistry of rodingite derived from eclogite in western Tianshan, China. Acta Petrologica Sinica 24, 711–717. https://doi.org/10.1111/j.1525-1314.2007.00700.x.

Liu, X., Su, W., Gao, J., Li, J.-L., Jiang, T., 2013. Continental crust material in subduction complex in southwestern Tienshan – geochemical implications from metabasic rocks. Acta Petrologia Sinica 29 (5), 1675 – 1684.

Loury, C., Rolland, Y., Cenki-Tok, B., Lanari, P., Guillot, S., 2016. Late Paleozoic evolution of the South Tien Shan: Insights from P-T estimates and allanite geochronology on retrogressed eclogites (Chatkal range, Kyrgyzstan). Journal of Geodynamics 96, 62–80. https://doi.org/10.1016/j.jog.2015.06.005.

MacGregor, I.D., 2015. Empirical geothermometers and geothermobarometers for spinel peridotite phase assemblages. International Geology Review 57, 1940–1974. https://doi.org/10.1080/00206814.2015.1045307.

Medaris, L.G., Beard, B.L., Johnson, C.M., Valley, J.W., Spicuzza, M.J., Jelínek, E., Mísâr, Z., 1995. Garnet pyroxenite and eclogite in the Bohemian Massif: geochemical evidence for Variscan recycling of subducted lithosphere. Geologische Rundschau 84, 489–505. https://doi.org/10.1007/BF00284516.

Medaris, G., Wang, H., Jelínek, E., Mihaljevič, M., Jakeš, P., 2005. Characteristics and origins of diverse Variscan peridotites in the Gföhl Nappe, Bohemian Massif, Czech Republic. Lithos 82, 1–23. https://doi.org/10.1016/j.lithos.2004.12.004.

Merkulova, M. V., Muñoz, M., Brunet, F., Vidal, O., Hattori, K., Vantelon, D., Trcera, N., Huthwelker, T., 2017. Experimental insight into redox transfer by iron- and sulfur-bearing serpentinite dehydration in subduction zones. Earth and Planetary Science Letters 479, 133–143. https://doi.org/10.1016/j.epsl.2017.09.009.

Meyer, M., Klemd, R., Konopelko, D., 2013. High-pressure mafic oceanic rocks from the Makbal Complex, Tianshan Mountains (Kazakhstan & Kyrgyzstan): Implications for the metamorphic evolution of a fossil subduction zone. Lithos 177, 207–225. https://doi.org/10.1016/j.lithos.2013.06.015.

Meyer, M., Klemd, R., Hegner, E., Konopelko, D., 2014. Subduction and exhumation mechanisms of ultra-high and high-pressure oceanic and continental crust at Makbal (Tianshan, Kazakhstan and Kyrgyzstan). Journal of metamorphic geology 32, 861–884. https://doi.org/10.1111/jmg.12097.

Mongkoltip, P., Ashworth, J.R., 1983. Quantitative Estimation of an Open-system Symplectite- forming Reaction: Restricted Diffusion of Al and Si in Coronas around Olivine. Journal of Petrology 24, 635–661. https://doi.org/10.1093/petrology/24.4.635.

Morimoto, N., Fabries, J., Ferguson, A.K., et al., 1988. Nomenclature of pyroxenes. American Mineralogist 73, 1123–1133.

Morishita, T., Arai, S., 2003. Evolution of spinel-pyroxene symplectite in spinel-lherzolites from the Horoman Complex, Japan. Contributions to Mineralogy and Petrology 144, 509–522. https://doi.org/10.1007/s00410-002-0417-y.

Müntener, O., Manatschal, G., Desmurs, L., Pettke, T., 2009. Plagioclase peridotites in ocean-continent transitions: Refertilized mantle domains generated by melt stagnation in the shallow mantle lithosphere. Journal of Petrology 51, 255–294. https://doi.org/10.1093/petrology/egp087.

Nedovizin, A.A., 1961. To the stratigraphy of the Akzhal formation of the Chu-Ili Mountains. Izvestiya AN KazSSR. Series geod. 2, 26–34 (in Russian).

Newton, R.C., Charlu, T.V., Kleppa, O.J., 1980. Thermochemistry of the high structural state plagioclases. Geochemica et Cosmochimica Acta 44, 933–941. https://doi.org/10.1016/0016-7037(80)90283-5.

Nikitina, O.I., Popov, L.E., Neuman, R.B., Bassett, M.G., Holmer, L.E., 2006. Mid Ordovician (Darriwilian) brachiopods of South Kazakhstan. In: BASSETT, M.G. and DEISLER, V.K. (eds), Studies in Palaeozoic palaeontology. National Museum of Wales Geological Series No. 25, Cardiff.145–222.

Obata, M., 2011. Kelyphite and symplectite: textural and mineralogical diversities and universality, and a new dynamic view of their structural formation, New Frontiers in Tectonic Research - General Problems, Sedimentary Basins and Island Arcs, Prof. Evgenii Sharkov (Ed.), InTech, DOI: https://doi.org/10.5772/20265.

Obata, M., Ozawa, K., 2011. Topotaxic relationships between spinel and pyroxene in kelyphite after garnet in mantle-derived peridotites and their implications to reaction mechanism and kinetics. Mineralogy and Petrology 101, 217–224. https://doi.org/10.1007/s00710-011-0145-y.

Obata, M., Ozawa, K., Naemura, K., Miyake, A., 2013. Isochemical breakdown of garnet in orogenic garnet peridotite and its implication to reaction kinetics. Mineralogy and Petrology 107, 881–895. https://doi.org/10.1007/s00710-012-0260-4.

Okamoto, K., Liou, J.G., Ogasawara, Y., 2000. Petrology of the diamond-grade eclogite in the Kokchetav Massif, northern Kazakhstan. Island Arc 9, 379–399. https://doi.org/10.1046/j.1440-1738.2000.00284.x.

Orozbaev, R.T., Takasu, A., Bakirov, A.B., Tagiri, M., Sakiev, K.S., 2010. Metamorphic history of eclogites and country rock gneisses in the Aktyuz area, Northern Tien-Shan, Kyrgyzstan: A record from initiation of subduction through to oceanic closure by continent-continent collision. Journal of Metamorphic Geology 28, 317–339. https://doi.org/10.1111/j.1525-1314.2010.00865.x.

Paulick, H., Bach, W., Godard, M., De Hoog, J.C.M., Suhr, G., Harvey, J., 2006. Geochemistry of abyssal peridotites (Mid-Atlantic Ridge, 15°20′N, ODP Leg 209): Implications for fluid/rock interaction in slow spreading environments. Chemical Geology 234, 179–210. https://doi.org/10.1016/j.chemgeo.2006.04.011.

Pearce, J.A., Lippard, S.J., Roberts, S., 1984. Characteristics and tectonic significance of supra-subduction zone ophiolites. Geol. Soc. London, Spec. Publ. 16, 77–94. https://doi.org/10.1144/GSL.SP.1984.016.01.06.

Pearce, J.A., Parkinson, I.J., 1993. Trace element models for mantle melting: application to volcanic arc petrogenesis. Geol. Soc. London, Spec. Publ. 76, 373–403. https://doi.org/10.1144/GSL.SP.1993.076.01.19.

Pearce, J.A., Barker, P.F., Edwards, S.J., Parkinson, I.J., Leat, P.T., 2000. Geochemistry and tectonic significance of peridotites from the South Sandwich arc-basin system, South Atlantic. Contributions to Mineralogy and Petrology 139, 36–53. https://doi.org/10.1007/s004100050572.

Pearce, J. A., Robinson, P., Yang, J., 2011. Identification and interpretation of eclogite protoliths using immobile element geochemistry: some new methodologies. American Geophysical Union, Fall Meeting 2011, abstract #V22C-07.

Pilitsyna, A. V., Tretyakov, A.A., Degtyarev, K.E., Cuthbert, S.J., Batanova, V.G., Kovalchuk, E. V., 2018. Eclogites and garnet clinopyroxenites in the Anrakhai complex, Central Asian Orogenic Belt, Southern Kazakhstan: P-T evolution, protoliths and some geodynamic implications. Journal of Asian Earth Sciences 153, 325–345. https://doi.org/10.1016/j.jseaes.2017.03.027.

Proyer, A., 2003. The preservation of high-pressure rocks during exhumation: Metagranites and metapelites. Lithos 70, 183–194. https://doi.org/10.1016/S0024-4937(03)00098-7.

Reverdatto, V. V., Selyatitskiy, A.Y., Carswell, D.A., 2008. Geochemical distinctions between “crustal” and mantle-derived peridotites/pyroxenites in high/ultrahigh pressure metamorphic complexes. Russian Geology and Geophysics 49, 73–90. https://doi.org/10.1016/j.rgg.2008.01.002.

Rice, J.M., 1983. Metamorphism of rodingites: part I. Phase relations in a portion of the system CaO-MgO-Al2O3-SiO2-CO2-H2O. American Journal of Science 283 (A), 121 – 510.

Ruiz Cruz, M.D., Puga, E., Nieto, J.M., 1999. Silicate and oxide exsolution in pseudo-spinifex olivine from metaultramafic rocks of the Betic ophiolitic association: A TEM study. American Mineralogist 84, 1915–1924. https://doi.org/10.2138/am-1999-11-1219.

Ryazantsev, A.V., Mikolaychuk, A.V., Tolmacheva, T.Yu., Degtyarev, K.E., Kotov, A.B., Nikitina, O.I., Mamonov, E.P., Zorin, A.E., 2009a. Ophiolites and island-arc complexes of Dzhalair-Naiman zone and Chu-Kendyktas massifs (Southern Kazakhstan): structures, ages and formation settings // Geodynamics of intracontinental orogens and geoecological problems. Moscow – Bishkek, vol. 4C, 53 – 58.

Ryazantsev, A.V., Degtyrev, K.E., Kotova, A.B., Salynikova, E.B., Anisimova, I.V., Yakovleva, S.Z., 2009b. Ophiolites of Dzhalair-Naiman zone (Southern Kazakhstan): sequences structure, ages interpretation. Doklady RAS 427 (3), 359–364. https://doi.org/10.1134/S1028334X09060038.

Sarp, H., J. Bertrand, McNear, E., 1976. Vuagnatite, CaAl(OH)SiO4; a new natural calcium aluminum nesosilicate. American Mineralogist 61, 825–830.

Schmidt, M.W., 1992. Amphibole composition in tonalite as a function of pressure: an experimental calibration of the Al-in-hornblende barometer. Contributions to Mineralogy and Petrology 110, 304–310. https://doi.org/10.1007/BF00310745.

Soldner, J., Oliot, E., Schulmann, K., Stipska, P., Kusbach, V., Anczkiewicz, R., 2017. Metamorphic P - T - t - d evolution of (U)HP metabasites from the South Tianshan accretionary complex (NW China) – Implications for rock deformation during exhumation in a subduction channel. Gondwana Research 47, 161 – 187. https://doi.org/10.1016/j.gr.2016.07.007.

Song, S., Zhang, L., Niu, Y., 2004. Ultra-deep origin of garnet peridotite from the North Qaidam ultrahigh-pressure belt, northern Tibetan Plateau, NW China. American Mineralogist 89, 1330–1336. https://doi.org/10.2138/am-2004-8-922.

Song, S., Su, L., Niu, Y., Zhang, G., Zhang, L., 2009. Two types of peridotite in North Qaidam UHPM belt and their tectonic implications for oceanic and continental subduction: A review. Journal of Asian Earth Sciences 35, 285–297. https://doi.org/10.1016/j.jseaes.2008.11.009.

Streckeisen, A., 1976. Classification of the common igneous rocks by means of their chemical composition: a provisional attempt. Neues Jahrbuch fur Mineralogie, Monatschefte, 1 – 15.

Sun, S. -s., McDonough, W.F., 1989. Chemical and isotopic systematics of oceanic basalts: implications for mantle composition and processes. Geol. Soc. London, Spec. Publ. 42, 313–345. https://doi.org/10.1144/GSL.SP.1989.042.01.19.

Tan, Z., Agard, P., Gao, J., John, T., Li, J.L., Jiang, T., Bayet, L., Wang, X.S., Zhang, X., 2017. P–T–time-isotopic evolution of coesite-bearing eclogites: Implications for exhumation processes in SW Tianshan. Lithos 278–281, 1–25. https://doi.org/10.1016/j.lithos.2017.01.010.

Taylor, W.R., 1998. An experimental test of some geothermometer and geobarometer formulations for upper mantle peridotites with application to the thermobarometry of fertile lherzolite and garnet websterite. Neues Jahrbuch fur Mineralogie Abhandlungen 172, 381–408. https://doi.org/10.1127/njma/172/1998/381.

Tretyakov, A.A., Degtyarev, K.E., Kovach, V.P., Kotov, A.B., Salnikova, E.B., Pilitsyna, A.V., Yakovleva, S.Z., 2016a. The migmatite–gneiss complex of the Chuya–Kendyktas sialic massif (Southern Kazakhstan): Structure and age. Doklagy Earth Sciences 467. https://doi.org/10.1134/S1028334X16030156.

Tretyakov, A.A., Degtyarev, K.E., Sal'nikova, E.B., Shatagin, K.N., Kotov, A.B., Ryazantsev, A.V., Pilitsyna, A.V., Yakovleva, S.Z., Tolmacheva, E.V., Plotkina, Y.V., 2016b. Paleoproterozoic anorogenic granitoids of the Zheltav sialic massif (Southern Kazakhstan): Structural position and geochronology. Doklagy Earth Sciences 466. https://doi.org/10.1134/S1028334X16010165.

Turkin, A.I., Sobolev, N. V., 2009. Pyrope-knorringite garnets: overview of experimental data and natural parageneses. Russian Geology and Geophysics 50, 1169–1182. https://doi.org/10.1016/j.rgg.2009.11.015.

Turkin, A.I., 2011. Chromium-bearing garnets and spinels as index-minerals of P-T conditions of peridotites formation (experimental study). Doctor of Sci. Thesis. Novosibirsk, Russia.

Whitney, D.L., Evans, B.W., 2010. Abbreviations for names of rock-forming minerals. American Mineralogy 95, 185–187. https://doi.org/10.2138/am.2010.3371.

Windley, B.F., Alexeiev, D., Xiao, W., Kroner, A., Badarch, G., 2007. Tectonic models for accretion of the Central Asian Orogenic Belt. Journal of the Geological Society London. 164, 31–47. https://doi.org/10.1144/0016-76492006-022.

Workman, R.K., Hart, S.R., 2005. Major and trace element composition of the depleted MORB mantle (DMM). Earth Planet. Sci. Lett. 231, 53–72. https://doi.org/10.1016/j.epsl.2004.12.005.

Zhang, R.Y., Liou, J.G., Ernst, W.G., Coleman, R.G., Sobolev, N. V., Shatsky, V.S., 1997. Metamorphic evolution of diamond-bearing and associated rocks from the Kokchetav Massif, northern Kazakhstan. Journal of metamorphic geology 15, 479–496. https://doi.org/10.1111/j.1525-1314.1997.00035.x.

Zhang, R.Y., Liou, J.G., Yang, J.S., Yui, T.F., 2000. Petrochemical constraints for dual origin of garnet peridotites from the Dabie-Sulu UHP terrane, eastern-central China. Journal of metamorphic geology 18, 149–166. https://doi.org/10.1046/j.1525-1314.2000.00248.x.

Zhang, C., van Roermund, H., Zhang, L., 2011. Orogenic Garnet Peridotites. Tools to Reconstruct Paleo-Geodynamic Settings of Fossil Continental Collision Zones, Ultrahigh-Pressure Metamorphism. https://doi.org/10.1016/B978-0-12-385144-4.00015-1.

Zhang, L.F., Du, J.X., Lü, Z., Yang, X., Gou, L.L., Xia, B., Chen, Z.Y., Wei, C.J., Song, S.G., 2013. A huge oceanic-type UHP metamorphic belt in southwestern Tianshan, China: Peak metamorphic age and P-T path. Chinese Science Bulletin 58, 4378–4383. https://doi.org/10.1007/s11434-013-6074-x.

Ziberna, L., Klemme, S., Nimis, P., 2013. Garnet and spinel in fertile and depleted mantle: Insights from thermodynamic modelling. Contributions to Mineralogy and Petrology 166, 411–421. https://doi.org/10.1007/s00410-013-0882-5.

Fig.1. A. Precambrian massifs in the Western part of the CAOB: AY – Aktau-Yili, CT – Chinese Central Tien Shan, E-N – Erementau-Niyaz, IS – Issyk-Kul, K – Kokchetav, I –Ishkeolmes, ZT – Zheltau, Ch – Chatkal, Ch-K – Chu-Kendyktas, K-D – Karatau-Dzhebagly, K-T – Karatau-Talas, N-S – Naryn-Sarydzhaz, Ul – Ulutau (after Degtyarev et al., 2017).
B. Geological structure of the SE part of the Chu-Ili Mountains.

Fig.2. A. Geological structure of the Anrakhai Mountains. B. Field sketch of the investigated 'Ashchisu river' serpentinite pod.

Fig.3. Photomicrographs of minerals and microtextures of Cr-Spl serpentinized dunite (a) and symplectite-bearing Cr-Spl peridotite (b – e): a) Anhedral serpentinized olivine grains, surrounded by laths of chlorite (crossed nicols); b) General microtexture of symplectite-bearing Cr-Spl peridotite (crossed nicols). White dotted-lines mark Ol + Opx (COR) areas; yellow dotted-lines delimit metasomatically reworked areas; red dashed-lines indicate the "seams" in Cpx-Opx-Spl symplectitic areas; c) Back-scattered electron (BSE) images of Cpx-Opx-Spl symplectites (with different magnifications). Red-contoured areas are former Cpx (likely prior symplectite intergrowths); d) BSE image of Amp-Spl symplectites enclosing Cpx-Opx-Spl symplectites; e) Cr-bearing clinopyroxene rim with preserved cleavage, replacing the COR around olivine (crossed nicols).
Cr-Chl – chromium-bearing chlorite; Ol – olivine; (Cr-)Spl – (chromium-bearing) spinel; COR – coarse Opx rim; Amp – amphibole; Cpx – clinopyroxene; Opx – orthopyroxene; Hgr – hydrogrossular; Prh – prehnite; Vgn – vuagnatite.

Fig.4. Photomicrographs of the main minerals of symplectite-bearing Cr-Spl (a – d, f) and amphibole (e) peridotites: a) Solid inclusions of chromium spinel in olivine (plane light and BSE images); b) Zoned grains of Cr-Spl, at the boundaries between the CORs and symplectites (plane light). Black dashed-lines indicate the "seams" in Cpx-Opx-Spl symplectitic areas; c) Exsolutional lamellae of Cr-Spl in olivine (plane light and BSE images); d) Anhedral pale-green grains of Spl in association with amphibole (plane light); e) Groundmass amphibole crystals with relics of serpentinized olivine (crossed nicols); f) Areas of metasomatic assemblage development. Prehnite, vuagnatite and hydrogrossular tend to nucleate in the "seams" of Cpx-Opx-Spl symplectites (plane light and BSE images).
Ol – olivine; (Cr-)Spl – (chromium-bearing) spinel; COR – coarse Opx rim; Amp – amphibole; Cpx – clinopyroxene; Srp – serpentine; Hgr – hydrogrossular; Prh – prehnite; Vgn – vuagnatite.

Fig.5. Variation diagrams of major and trace elements, and normative mineral compositions for all sampled ultramafic rocks.

Fig.6. Chondrite- (A) and primitive mantle- (B) normalized patterns for ultramafic rocks. Black and red dashed-lines are samples from the layered cumulate sequence of the Atlantis massif (Middle-Atlantic Ridge (MAR)) (Godard et al., 2009). Grey area represents the refractory (mantle residue) harzburgite field (Godard et al., 2008); yellow area shows peridotites that have reacted with basaltic melts during their formation and were impregnated by LREE and fertile components (data from Paulick et al., 2006). Chondrite, primitive mantle and N-MORB values are from Sun and McDonough (1989); DMM (depleted MORB mantle) composition is from Workman and Hart (2005).

Fig.7. Chemical compositions of: a spinel (plot of Barnes and Roeder, 2001), b – spinel Mg# vs. Cr#; c – orthopyroxene; d – clinopyroxene (Morimoto et al., 1988).

Fig.8. Cpx-Opx-Spl symplectite area (from Fig. 4, b): a) – high-resolution BSE image of Cpx-Opx-Spl symplectite area with calculated local bulk composition (Table S7); b) – X-ray element maps (Mg, Na, Fe, Ca) of the symplectite area.

Fig.9. Chemical compositions of amphibole (Leake et al., 1997).

Fig.10. P-T pseudosection for CFMNASCr system based upon a calculated effective bulk composition (EBC). The details of recalculations and solution models are given in section 4.1.2. Colored lines are compositional isopleths for Cr-Spl (a), Opx (b, c) and Ol (d) (see details in the text).

Fig.11. a) – P-T pseudosection for Cpx-Opx-Spl symplectite (shown in Fig.8, a) for the CFMNAS system using the calculated effective bulk composition (EBC) (Table S7). Details of recalculations and solution models are given in section 4.1.2; b) - two-pyroxene geothermometry for Cpx-Opx-Spl symplectite (Cpx Y11 with Opx G1; tables S2, S4). The geothermometer isopleths are after: Taylor (1998) (red line), Brey and Köhler (1990) (blue line), MacGregor (2015) (green line).

Fig.12. Chondrite- (A) and Primitive Mantle-normalized (B) trace element distributions for high-pressure ultramafic complexes of different petrogenesis. 1 – serpentinites, Cr-Spinel serpentinized dunites, Cr-Spinel (symplectite-bearing) peridotites and amphibolitized peridotites of the Zheltau massif (this study; Table 1); 2 – garnet lherzolites of the Zhimafang complex, Dabie-Sulu UHP terrane (Zhang et al., 2000); 3 – garnet peridotites of the Bixiling complex, Dabie Mountains (Chavagnac and Jahn, 1996); 4 – eclogites of the Bixiling complex, Dabie Mountains (Chavagnac and Jahn, 1996); 5 – spinel and garnet peridotites of the Kokchetav massif, west CAOB (Reverdatto et al., 2008); 6 – garnet peridotites of the Almklovdalen complex, Western Gneiss Region (Beyer et al., 2006); 7 – garnet clinopyroxenites of the Rizhao complex, Dabie-Sulu UHP terrane (Jahn, 1998). Refertilized residual-mantle peridotites of the South Sandwich arc-basin system (Pearce et al., 2000): a) – lherzolites; b) dunites with cumulative textures; c) peridotites of the transitional zone; d) harzburgite.
Chondrite, PM and N-MORB values are from Sun and McDonough (1989); DMM (depleted MORB mantle) composition is from Workman and Hart (2005).

Fig.13. Chondrite- (A) and Primitive Mantle-normalized (B) trace elements distributions for ultramafic-mafic complexes of the Zheltau massif (this study) and the Marum Ophiolite Complex, Northern Papua New Guinea (Jaques et al., 1983). 1 – serpentinites, Cr-Spinel serpentinized dunites, Cr-Spinel (symplectite-bearing) peridotites and amphibolitized peridotites of the Zheltau massif (this study; Table 1); 2 - metamorphosed mafic Al-rich rocks of the Zheltau massif, sharing the single pod with the studied ultramafic rocks (unpublished personal data of author A.P.; Table S1); 3 – serpentinites in the NE part of the Koyandy complex, Zheltau massif (Fig. 2, A) (unpublished personal data of author A.P.; Table S1); 4 – amphibolitized gabbroids in the NE part of the Koyandy complex, Zheltau massif (Fig. 2, A) (unpublished personal data of author A.P.; Table S1); 5 – plagioclase lherzolite and wherlite of the Marum Ophiolite Complex (lower parts of the cumulative sequence) (Jackues et al., 1983); 6 – troctolite, olivine gabbros, gabbros and diorite of the Marum Ophiolite Complex (upper parts of the cumulative sequence) (Jackues et al., 1983). Chondrite, PM and N-MORB values are from Sun and McDonough (1989); DMM (depleted MORB mantle) composition is from Workman and Hart (2005).

Fig.14. Sc-Co-Al*4 diagrams with ‘MOR-type’ (left triangle) and ‘SSZ-type’ (right triangle) crystallization sequences for both unmetamorphosed and strongly metamorphosed ultramafic/mafic complexes (Pearce et al., 2011 and Pearce, pers. comm., 2017) of the Zheltau massif.

Fig. 15. Geodynamic model for the Zheltau massif complexes formation.

**Table 1.** Selected chemical analyses of spinel-bearing ultramafic rocks. Major elements are in wt.%, trace elements are in ppm. Mg# = MgO/(MgO + $FeO_{(tot)}$); $FeO_{(tot)} = 0.9Fe_2O_3 + FeO$; n.d. is 'not determined'; LOI is 'loss on ignition'. Starred samples are intensively rodingitizied varieties. Normative compositions are in vol.%, calculated with using of the Normalization excel-based program, written by Kurt Hollocher (Geology Department, Union College, Schenectady, NY).

**Table 1.** Selected chemical analyses of spinel-bearing ultramafic rocks. Major elements are in wt.%, trace elements are in ppm. Mg# = MgO/(MgO + $FeO_{(tot)}$); $FeO_{(tot)}$ = $0.9Fe_2O_3$ + FeO; n.d. is 'not determined'; LOI is 'loss on ignition'. Starred samples are intensively rodingitizied varieties. Normative compositions are in vol.%, calculated with using of the Normalization excel-based program, written by Kurt Hollocher (Geology Department, Union College, Schenectady, NY).

| Sample | Magnetite-bearing serpentinite | | | | Cr-Spl serpentinized dunite | | Cr-Spl (symplectite-bearing) peridotite | | | | Amphibolitized Cr-Spl peridotite | | |
|---|---|---|---|---|---|---|---|---|---|---|---|---|---|
| | AH 1513 | AH 1504 | AH 1506 | AH 1417/1 | AH 1507 | AH 1322/3 | AH 1512* | AH 1503* | AH 1417/2 | AH 1511* | AH 1510 | AH 1417 | AH 1508 |
| $SiO_2$ | 37.99 | 34.54 | 35.89 | 39.32 | 37.76 | 36.87 | 37.80 | 37.24 | 39.08 | 35.77 | 36.87 | 38.76 | 38.72 |
| $TiO_2$ | 0.02 | 0.03 | 0.02 | 0.03 | 0.03 | 0.03 | 0.02 | 0.03 | 0.02 | 0.02 | 0.04 | 0.04 | 0.02 |
| $Al_2O_3$ | 1.06 | 2.41 | 2.58 | 2.49 | 5.32 | 4.93 | 5.70 | 6.51 | 7.67 | 6.97 | 7.88 | 9.15 | 7.19 |
| $Fe_2O_3$ (I&B) | 1.52 | 1.53 | 1.52 | 1.54 | 1.53 | 1.53 | 1.52 | 1.53 | 1.52 | 1.53 | 1.54 | 1.54 | 1.52 |
| FeO (I&B) | 9.17 | 8.50 | 7.64 | 7.13 | 7.71 | 7.93 | 7.17 | 8.40 | 9.15 | 6.84 | 7.55 | 7.91 | 8.42 |
| MnO | 0.12 | 0.10 | 0.06 | 0.12 | 0.13 | 0.13 | 0.17 | 0.14 | 0.16 | 0.19 | 0.12 | 0.12 | 0.17 |
| MgO | 37.88 | 36.07 | 36.50 | 36.41 | 34.18 | 34.04 | 33.97 | 31.63 | 30.68 | 31.88 | 29.46 | 27.93 | 30.93 |
| CaO | 0.55 | 3.29 | 2.59 | 0.12 | 1.96 | 2.51 | 2.40 | 3.83 | 4.26 | 4.09 | 7.07 | 5.08 | 2.93 |
| $Na_2O$ | 0.01 | 0.01 | 0.09 | 0.06 | 0.09 | 0.09 | 0.02 | 0.29 | 0.68 | 0.03 | 0.20 | 0.70 | 0.33 |
| $K_2O$ | 0.01 | 0.01 | 0.01 | 0.02 | 0.01 | 0.01 | 0.01 | 0.02 | 0.03 | 0.01 | 0.02 | 0.36 | 0.01 |
| $P_2O_5$ | 0.03 | 0.03 | 0.03 | 0.03 | 0.03 | 0.03 | 0.03 | 0.03 | 0.03 | 0.03 | 0.03 | 0.03 | 0.03 |
| LOI | 12.05 | 14.10 | 13.57 | 13.18 | 11.56 | 12.30 | 11.50 | 10.61 | 6.52 | 13.10 | 9.35 | 8.39 | 9.90 |
| $FeO_{(tot)}$ | 9.26 | 8.48 | 7.78 | 7.39 | 8.02 | 8.14 | 7.55 | 8.71 | 9.79 | 7.12 | 8.08 | 8.48 | 8.79 |
| Total | 98.98 | 99.07 | 99.13 | 99.17 | 99.09 | 99.08 | 99.16 | 99.04 | 98.91 | 99.21 | 99.10 | 99.05 | 99.02 |
| Mg# | 0.80 | 0.81 | 0.82 | 0.83 | 0.81 | 0.81 | 0.82 | 0.78 | 0.76 | 0.82 | 0.78 | 0.77 | 0.78 |
| K+Na | 0.02 | 0.02 | 0.10 | 0.08 | 0.10 | 0.10 | 0.03 | 0.31 | 0.71 | 0.04 | 0.21 | 1.06 | 0.34 |
| $Fe_2O_3$ (init) | 9.41 | 8.94 | 7.84 | 7.86 | 7.08 | 6.65 | 6.94 | 6.78 | 6.89 | 5.37 | 6.54 | 5.96 | 7.20 |
| FeO (init) | 0.79 | 0.43 | 0.73 | 0.32 | 1.65 | 2.16 | 1.30 | 2.61 | 3.59 | 2.29 | 2.19 | 3.12 | 2.31 |
| Sc | 7.187 | 10.544 | 6.699 | 7.671 | 7.516 | 7.4 | 6.298 | 7.075 | 5.796 | 5.745 | 11.111 | 6.612 | 6.176 |
| V | 8.057 | 22.006 | 15.724 | n.d. | 26.372 | 16.2 | 10.187 | 9.441 | 8.135 | 15.830 | 27.011 | 16.126 | 21.687 |
| Cr | 810.975 | 995.827 | 1084.748 | 3080.184 | 3114.394 | 2713 | 737.494 | 401.629 | 601.004 | 1350.199 | 1269.162 | 1273.125 | 1879.129 |
| Co | 156.534 | 134.954 | 126.105 | 109.946 | 123.702 | 116 | 119.201 | 116.540 | 94.438 | 125.388 | 104.238 | 95.799 | 132.692 |
| Ni | 2064.112 | 1839.599 | 1837.408 | 2240.486 | 1719.128 | 1529 | 1603.039 | 1356.622 | 1293.485 | 1527.471 | 1085.563 | 1393.011 | 1502.281 |
| Cu | 6.885 | 36.140 | 113.626 | 70.236 | 28.590 | 18.1 | 59.627 | 61.619 | 111.121 | 39.180 | 66.442 | 86.709 | 216.383 |
| Zn | 43.543 | 36.708 | 19.975 | 49.104 | 36.826 | 34.9 | 35.412 | 39.537 | 37.106 | 37.533 | 22.096 | 33.758 | 33.762 |
| Ga | 1.088 | 1.535 | 2.011 | 2.233 | 3.927 | 3.2 | 2.794 | 3.461 | 3.501 | 3.583 | 4.208 | 5.364 | 4.850 |
| Rb | n.d. | 0.129 | 0.195 | 0.402 | 0.399 | 0.66 | 0.188 | 0.676 | 1.405 | 0.512 | 0.377 | 11.335 | 0.596 |
| Sr | 7.741 | 48.451 | 21.343 | 2.384 | 10.170 | 16.1 | 4.729 | 37.764 | 53.649 | 23.481 | 27.950 | 81.372 | 25.910 |
| Y | 0.153 | 0.593 | 0.172 | 0.390 | 0.335 | 0.45 | 0.254 | 0.267 | 0.138 | 0.551 | 0.685 | 0.353 | 0.156 |
| Zr | 0.452 | 0.694 | 0.456 | 0.734 | 0.465 | 0.87 | 0.818 | 0.606 | 0.671 | 0.645 | 0.708 | 1.020 | 0.464 |
| Nb | n.d. | 0.055 | n.d. | 0.123 | n.d. | 0.093 | n.d. | 0.056 | n.d. | 0.063 | n.d. | 0.070 | n.d. |
| Mo | 1.146 | 0.539 | 0.252 | 1.423 | 1.071 | 0.076 | 0.276 | 0.181 | 0.062 | 0.182 | 0.302 | 0.103 | 0.580 |

| | | | | | | | | | | | | | |
|---|---|---|---|---|---|---|---|---|---|---|---|---|---|
| **Cs** | 0.008 | 0.074 | 0.009 | n.d. | 0.301 | 0.58 | 0.056 | 0.487 | 1.276 | 0.326 | 0.197 | 0.818 | 0.276 |
| **Ba** | 2.605 | 3.076 | 5.428 | 2.445 | 2.229 | 4.7 | 1.570 | 3.452 | 4.574 | 2.511 | 2.417 | 32.648 | 5.522 |
| **La** | n.d. | 0.176 | n.d. | 0.087 | n.d. | 0.066 | n.d. | n.d. | 0.060 | 0.861 | n.d. | 0.066 | n.d. |
| **Ce** | n.d. | 0.355 | 0.148 | 0.259 | 0.086 | 0.2 | 0.118 | 0.198 | 0.196 | 1.439 | 0.114 | 0.244 | 0.108 |
| **Pr** | n.d. | 0.043 | 0.016 | 0.031 | 0.014 | 0.033 | 0.018 | 0.019 | 0.021 | 0.191 | 0.023 | 0.027 | 0.014 |
| **Nd** | n.d. | 0.037 | n.d. | n.d. | n.d. | 0.13 | n.d. | n.d. | 0.036 | 0.580 | n.d. | 0.077 | n.d. |
| **Sm** | n.d. | 0.046 | n.d. | 0.043 | 0.023 | 0.05 | 0.031 | 0.026 | 0.018 | 0.120 | 0.044 | 0.045 | 0.019 |
| **Eu** | n.d. | 0.021 | 0.014 | 0.024 | 0.029 | 0.03 | 0.021 | 0.050 | 0.062 | 0.043 | 0.029 | 0.083 | 0.050 |
| **Gd** | n.d. | 0.058 | n.d. | 0.054 | 0.034 | 0.05 | 0.021 | 0.024 | 0.015 | 0.101 | 0.073 | 0.066 | 0.016 |
| **Tb** | n.d. | 0.011 | n.d. | 0.009 | 0.007 | 0.011 | 0.006 | 0.006 | n.d. | 0.016 | 0.016 | 0.010 | n.d. |
| **Dy** | n.d. | 0.046 | n.d. | 0.059 | n.d. | 0.08 | n.d. | n.d. | 0.012 | 0.049 | 0.075 | 0.048 | n.d. |
| **Ho** | n.d. | 0.020 | n.d. | 0.014 | 0.011 | 0.017 | 0.009 | 0.009 | n.d. | 0.019 | 0.025 | 0.015 | n.d. |
| **Er** | n.d. | 0.070 | 0.022 | 0.059 | 0.035 | 0.063 | 0.026 | 0.030 | 0.019 | 0.055 | 0.072 | 0.043 | n.d. |
| **Tm** | n.d. | n.d. | n.d. | 0.009 | n.d. | 0.01 | n.d. | n.d. | 0.004 | n.d. | 0.010 | 0.007 | n.d. |
| **Yb** | n.d. | 0.081 | 0.046 | 0.075 | 0.057 | 0.071 | 0.040 | 0.051 | 0.028 | 0.055 | 0.071 | 0.039 | 0.026 |
| **Lu** | n.d. | 0.015 | 0.009 | 0.013 | 0.010 | 0.012 | 0.007 | 0.009 | n.d. | 0.013 | 0.013 | 0.008 | 0.007 |
| **Hf** | n.d. | n.d. | n.d. | n.d. | n.d. | 0.01 | n.d. | n.d. | n.d. | n.d. | n.d. | n.d. | n.d. |
| **Ta** | 0.018 | 0.043 | 0.031 | 0.107 | 0.051 | 0.17 | 0.027 | 0.175 | 0.057 | 0.077 | 0.018 | 0.049 | 0.033 |
| **W** | 0.145 | 1.035 | 0.612 | 1.076 | 0.433 | 0.26 | 0.081 | n.d. | 0.042 | 0.351 | 0.133 | 0.106 | 0.134 |
| **Pb** | 0.960 | 1.426 | 0.840 | 0.559 | 0.785 | 0.64 | 0.444 | 0.594 | 0.917 | 0.712 | 0.534 | 1.603 | 1.199 |
| **Th** | n.d. | 0.048 | 0.029 | 0.042 | n.d. | 0.019 | n.d. | n.d. | 0.021 | 0.152 | n.d. | 0.034 | n.d. |
| **U** | 0.013 | 0.029 | 0.019 | 0.067 | n.d. | 0.01 | 0.041 | n.d. | n.d. | n.d. | 0.141 | 0.014 | n.d. |
| **Ti** | 151 | 252 | 196 | 333 | 294 | 300 | 200 | 273 | 164 | 244 | 373 | 358 | 199 |
| **K** | 54 | 68 | 118 | 198 | 114 | 100 | 91 | 216 | 338 | 105 | 166 | 3566 | 142 |
| **P** | 260 | 280 | 290 | 260 | 260 | 300 | 260 | 290 | 270 | 270 | 280 | 334 | 270 |
| **Li** | 2.425 | 1.384 | 13.783 | 0.730 | 2.321 | n.d. | 13.268 | 30.985 | 43.494 | 0.793 | 2.235 | 13.757 | 6.322 |
| **∑REE** | n.d. | 0.979 | 0.255 | 0.737 | 0.307 | 0.823 | 0.296 | 0.423 | 0.470 | 3.541 | 0.566 | 0.777 | 0.239 |
| | | | | | | **Normative compositions (vol.%)** | | | | | | | |
| **Number on Fig. S1** | **1** | **2** | **3** | **4** | **5** | **6** | **7** | **8** | **9** | **10** | **11** | **12** | **13** |
| **Pl** | 3.7 | 9.2 | 10.3 | 1.4 | 14.1 | 17.7 | 16.0 | 25.0 | 29.8 | 25.7 | 26.5 | 32.2 | 22.7 |
| **Cpx** | 0.0 | 4.0 | 5.7 | 0.0 | 0.0 | 0.0 | 0.0 | 2.1 | 2.6 | 1.2 | 5.7 | 3.5 | 0.0 |
| **Opx** | 21.6 | 0.0 | 3.0 | 37.3 | 19.3 | 11.6 | 18.7 | 4.4 | 0.3 | 3.7 | 0.0 | 0.0 | 17.2 |
| **Ol** | 73.0 | 83.2 | 79.5 | 57.5 | 63.5 | 68.8 | 62.5 | 66.9 | 65.5 | 67.9 | 62.3 | 59.0 | 57.2 |

## Highlights

- Cpx-Opx-Spl symplectites in spinel peridotites were formed after garnet breakdown
- Shallow plagioclase-bearing ultramafic rocks were subducted to HP conditions
- Suboceanic depleted mantle-derived cumulative sequence is an inferred protolith

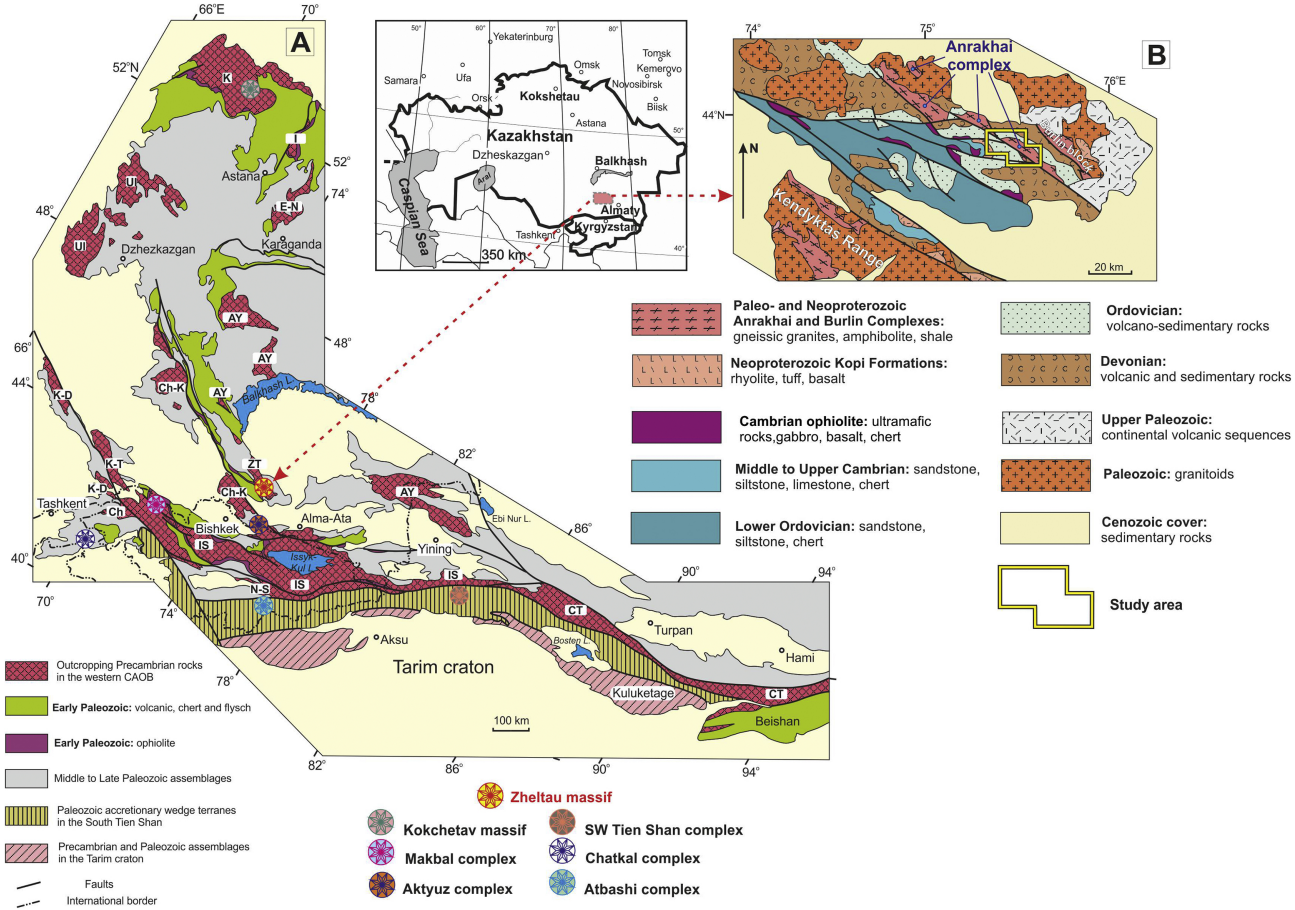
A
B
66°E
70°
52°N
48°
44°
74°
78°
82°
86°
90°
94°
Astana
Karaganda
Dzhezkazgan
Tashkent
Bishkek
Alma-Ata
Yining
Aksu
Turpan
Hami
Kuluketage
Beishan
Tarim craton
100 km
Issyk Kul L.
Ebi Nur L.
Bosten L.
Yekaterinburg
Omsk
Tomsk
Kemerovo
Novosibirsk
Biisk
Samara
Ufa
Orsk
Kokshetau
Astana
Kazakhstan
Dzheskazgan
Balkhash
Aral
Caspian Sea
Almaty
Kyrgyzstan
Tashkent
350 km
Anrakhai complex
Kendyktas Range
Sarmbulak
20 km
N
K
U
I
E-N
AY
Ch-K
K-D
Ch
IS
N-S
ZT
K-T
CT
Paleo- and Neoproterozoic Anrakhai and Burlin Complexes: gneissic granites, amphibolite, shale
Neoproterozoic Kopi Formations: rhyolite, tuff, basalt
Cambrian ophiolite: ultramafic rocks,gabbro, basalt, chert
Middle to Upper Cambrian: sandstone, siltstone, limestone, chert
Lower Ordovician: sandstone, siltstone, chert
Ordovician: volcano-sedimentary rocks
Devonian: volcanic and sedimentary rocks
Upper Paleozoic: continental volcanic sequences
Paleozoic: granitoids
Cenozoic cover: sedimentary rocks
Study area
Outcropping Precambrian rocks in the western CAOB
Early Paleozoic: volcanic, chert and flysch
Early Paleozoic: ophiolite
Middle to Late Paleozoic assemblages
Paleozoic accretionary wedge terranes in the South Tien Shan
Precambrian and Paleozoic assemblages in the Tarim craton
Faults
International border
Zheltau massif
Kokchetav massif
Makbal complex
Aktyuz complex
SW Tien Shan complex
Chatkal complex
Atbashi complex

Figure 1

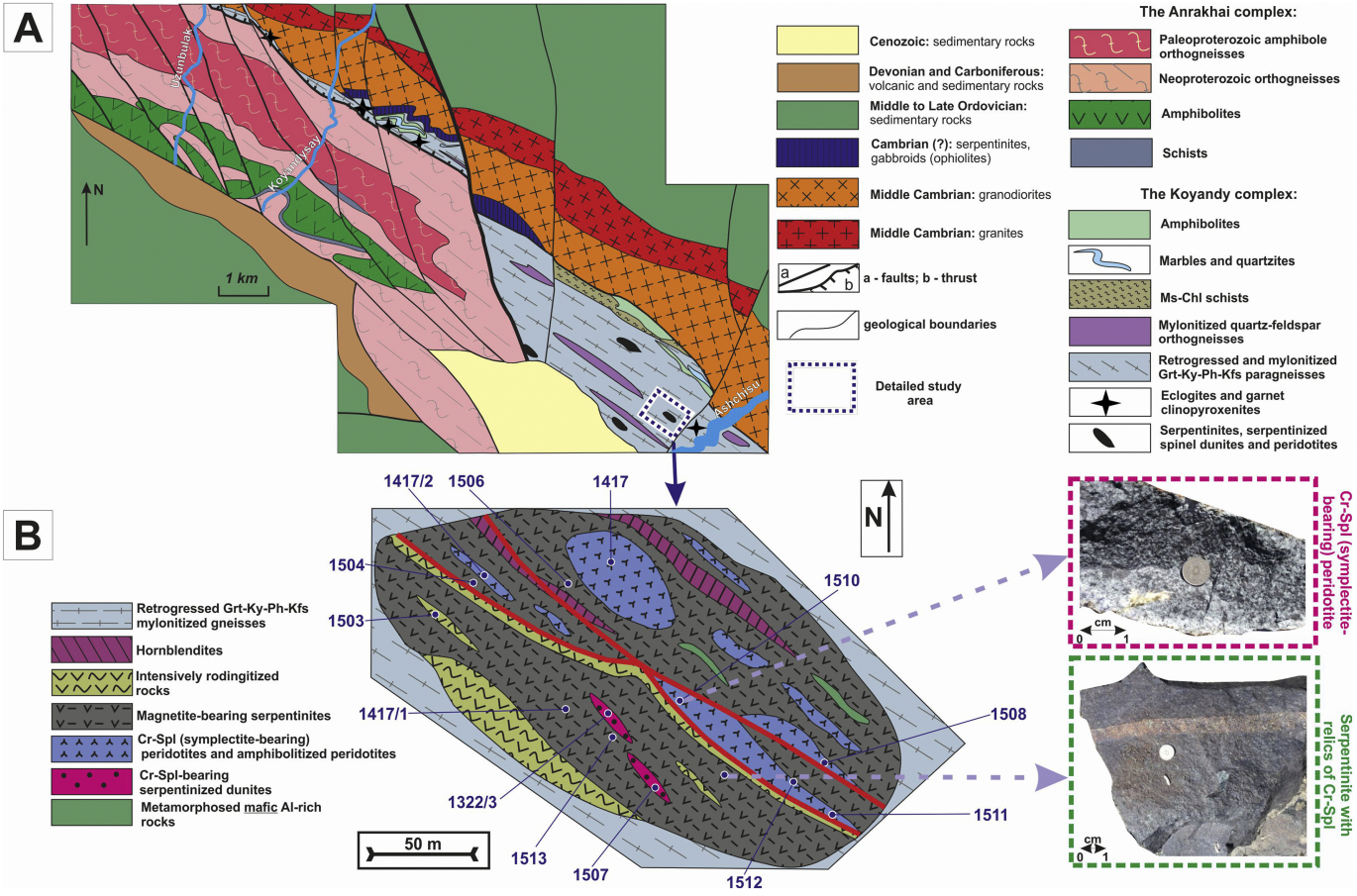
A
Ozernburlak
Koyandysay
N
1 km
Ashchysay
Cenozoic: sedimentary rocks
Devonian and Carboniferous: volcanic and sedimentary rocks
Middle to Late Ordovician: sedimentary rocks
Cambrian (?): serpentinites, gabbroids (ophiolites)
Middle Cambrian: granodiorites
Middle Cambrian: granites
a - faults; b - thrust
geological boundaries
Detailed study area
The Anrakhai complex:
Paleoproterozoic amphibole orthogneisses
Neoproterozoic orthogneisses
Amphibolites
Schists
The Koyandy complex:
Amphibolites
Marbles and quartzites
Ms-Chl schists
Mylonitized quartz-feldspar orthogneisses
Retrogressed and mylonitized Grt-Ky-Ph-Kfs paragneisses
Eclogites and garnet clinopyroxenites
Serpentinites, serpentinized spinel dunites and peridotites
B
Retrogressed Grt-Ky-Ph-Kfs mylonitized gneisses
Hornblendites
Intensively rodingitized rocks
Magnetite-bearing serpentinites
Cr-Spl (symplectite-bearing) peridotites and amphibolitized peridotites
Cr-Spl-bearing serpentinized dunites
Metamorphosed mafic Al-rich rocks
1417/2
1506
1417
1504
1503
1510
1417/1
1508
1322/3
1511
1513
1507
1512
50 m
N
Cr-Spl (symplectite-bearing) peridotite
cm
0
1
Serpentinite with relics of Cr-Spl

Figure 2

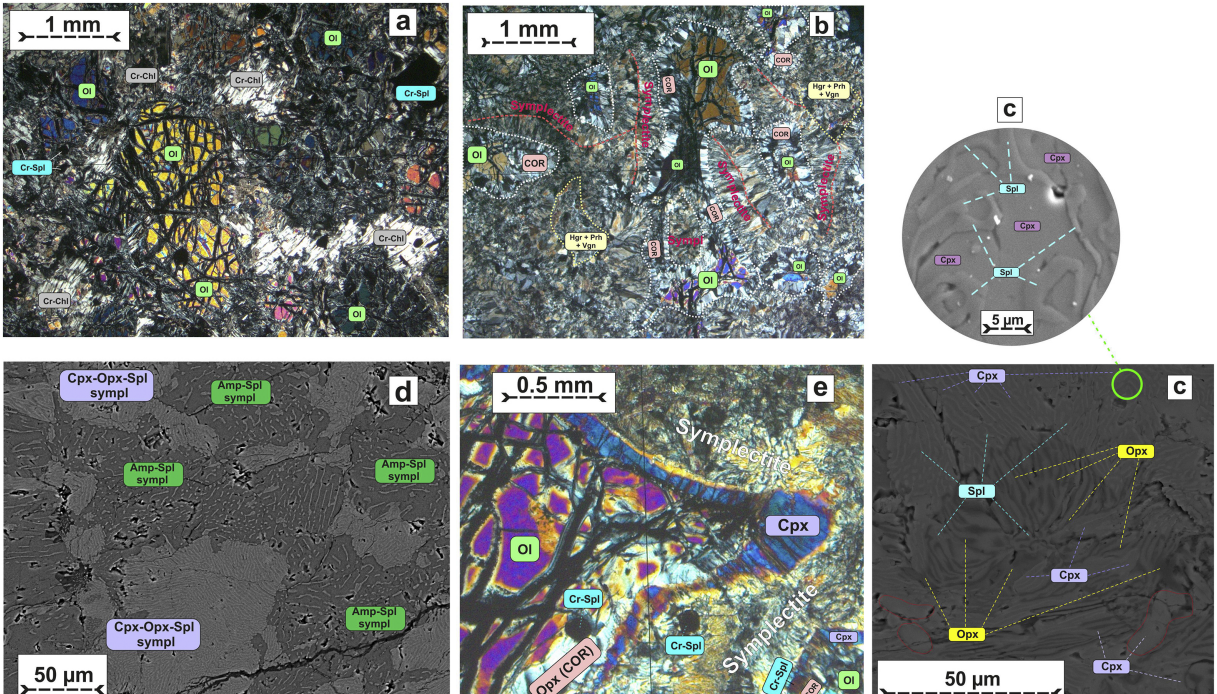
a
1 mm
Ol
Cr-Chl
Cr-Spl
b
1 mm
COR
Hgr + Prh + Ygn
Symplectite
c
Cpx
Spl
5 μm
d
Cpx-Opx-Spl sympl
Amp-Spl sympl
50 μm
e
0.5 mm
Symplectite
Cpx
Opx (COR)
c
Opx
50 μm

Figure 3

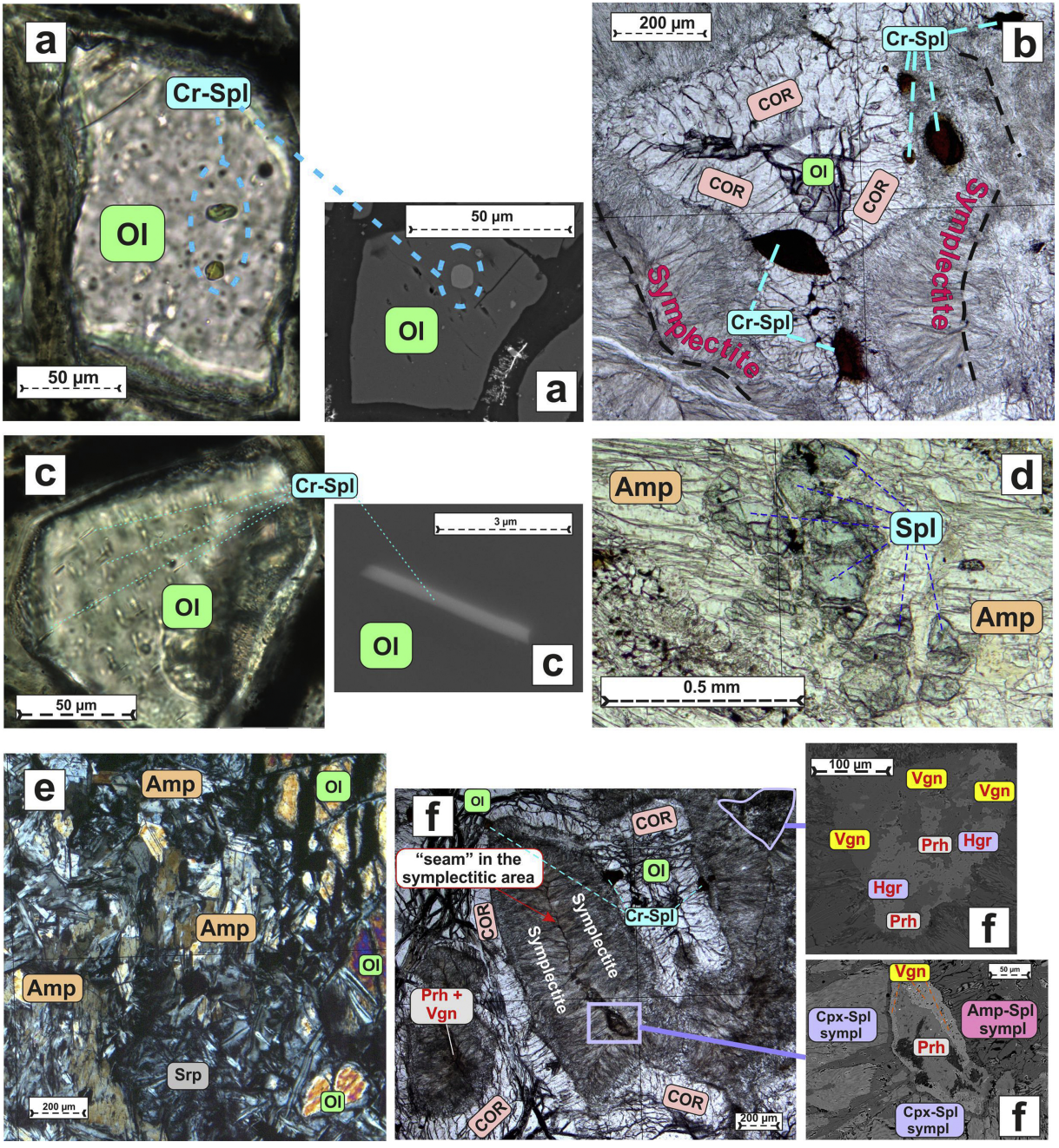
a
Cr-Spl
Ol
50 µm
50 µm
Ol
a
200 µm
Cr-Spl
b
COR
COR
Ol
COR
Symplectite
Symplectite
Cr-Spl
c
Cr-Spl
Ol
50 µm
3 µm
Ol
c
Amp
d
Spl
Amp
0.5 mm
e
Amp
Ol
Amp
Ol
Amp
Srp
200 µm
Ol
f
Ol
COR
"seam" in the symplectitic area
Ol
COR
Symplectite
Cr-Spl
Symplectite
Prh + Vgn
COR
COR
200 µm
100 µm
Vgn
Vgn
Vgn
Prh
Hgr
Hgr
Prh
f
Vgn
50 µm
Cpx-Spl sympl
Amp-Spl sympl
Prh
Cpx-Spl sympl
f

Figure 4

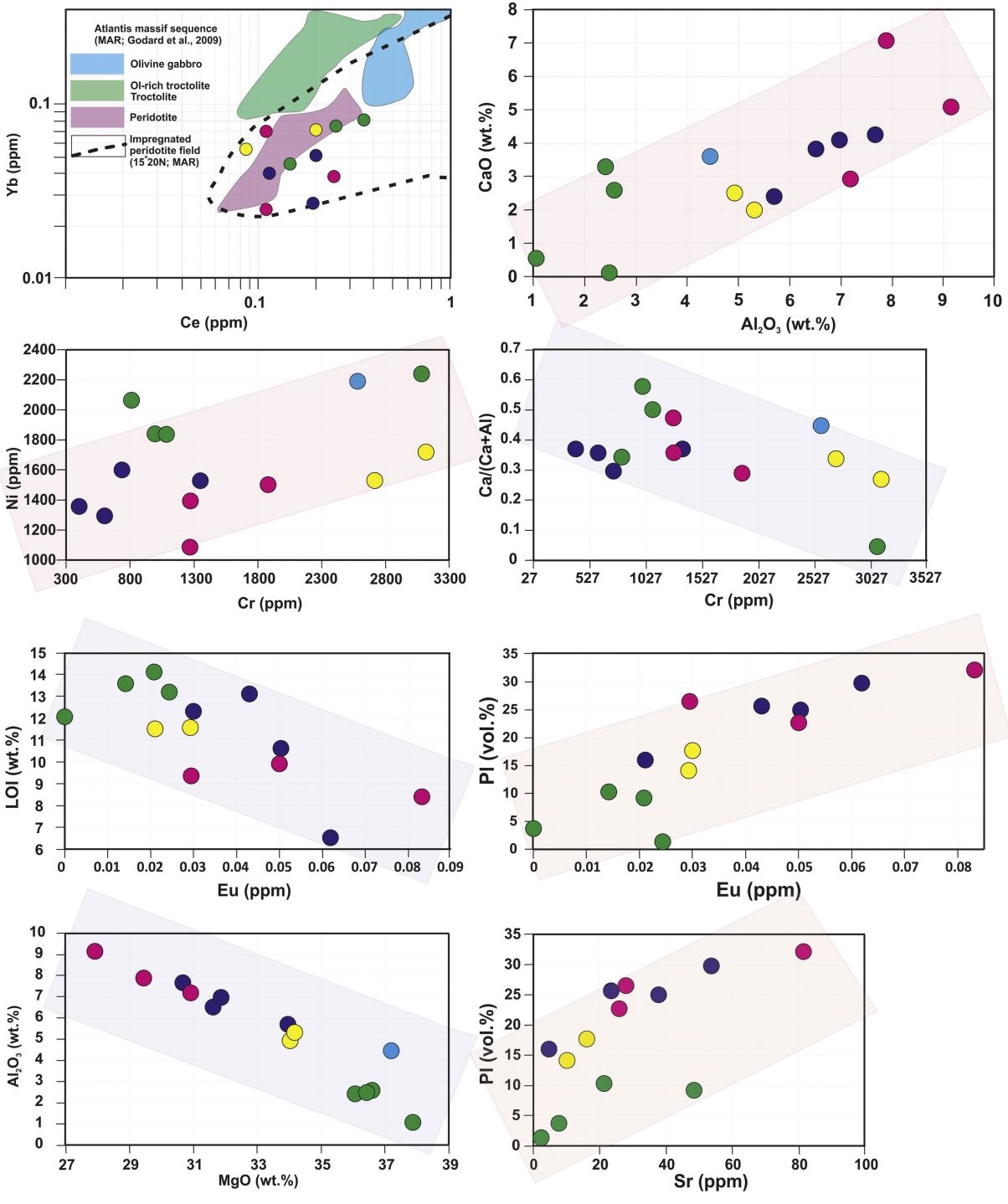
Atlantis massif sequence
(MAR; Godard et al., 2009)
Olivine gabbro
Ol-rich troctolite
Troctolite
Peridotite
Impregnated
peridotite field
(15°20N; MAR)
Yb (ppm)
Ce (ppm)
CaO (wt.%)
Al2O3 (wt.%)
Ni (ppm)
Cr (ppm)
Ca/(Ca+Al)
Cr (ppm)
LOI (wt.%)
Eu (ppm)
Pl (vol.%)
Eu (ppm)
Al2O3 (wt.%)
MgO (wt.%)
Pl (vol.%)
Sr (ppm)
Primitive mantle (after Sun & McDonough, 1989)
Magnetite-bearing serpentinite
Cr-Spl serpentinized dunite
Cr-Spl symplectite-bearing peridotite
Amphibolitized Cr-Spl peridotite

Figure 5

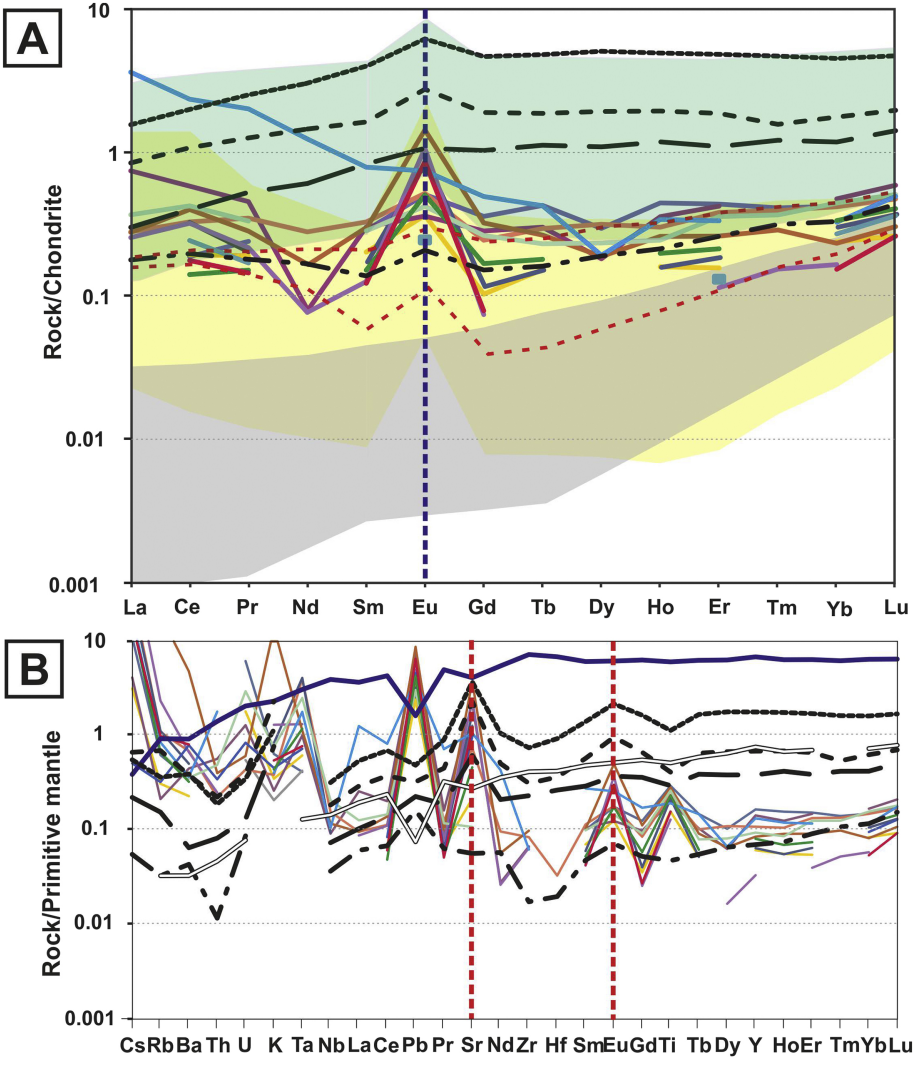
A
Rock/Chondrite
10
1
0.1
0.01
0.001
La Ce Pr Nd Sm Eu Gd Tb Dy Ho Er Tm Yb Lu
B
Rock/Primitive mantle
10
1
0.1
0.01
0.001
Cs Rb Ba Th U K Ta Nb La Ce Pb Pr Sr Nd Zr Hf Sm Eu Gd Ti Tb Dy Y Ho Er Tm Yb Lu
AH 1322/3
AH 1417/1
AH 1511
AH 1504
AH 1507
AH 1503
AH 1506
AH 1417
AH 1512
AH 1508
AH 1417/2
AH 1510
AH 1513
DMM
N-MORB
Reacted and impregnated peridotites (Paulick et al., 2006)
Mantle refractory harzburgites (Godard et al., 2008)
Atlantis massif sequence (MAR; Godard et al., 2009)
Cumulative sequence
Olivine gabbro
Troctolite
Olivine-rich troctolite
Olivine gabbro, troctolite, olivine-rich troctolite
Mantle residue
Refertilized refractory peridotite
Refertilized refractory peridotite (Hole U1309B)

Figure 6

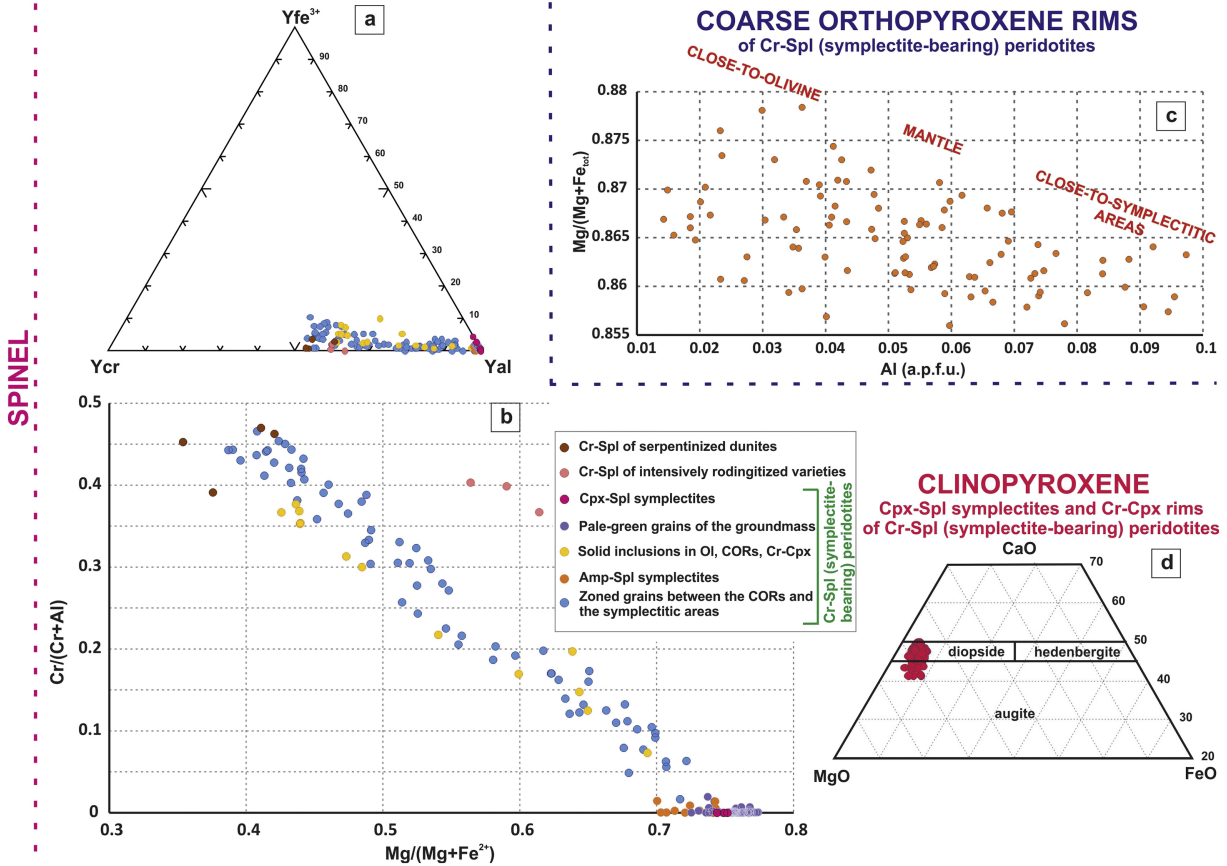
SPINEL
a
Yfe3+
Ycr
Yal
b
Cr/(Cr+Al)
Mg/(Mg+Fe2+)
Cr-Spl of serpentinized dunites
Cr-Spl of intensively rodingitized varieties
Cpx-Spl symplectites
Pale-green grains of the groundmass
Solid inclusions in Ol, CORs, Cr-Cpx
Amp-Spl symplectites
Zoned grains between the CORs and the symplectitic areas
Cr-Spl (symplectite-bearing) peridotites
COARSE ORTHOPYROXENE RIMS
of Cr-Spl (symplectite-bearing) peridotites
c
CLOSE-TO-OLIVINE
MANTLE
CLOSE-TO-SYMPLECTITIC AREAS
Mg/(Mg+Fetot)
Al (a.p.f.u.)
CLINOPYROXENE
Cpx-Spl symplectites and Cr-Cpx rims
of Cr-Spl (symplectite-bearing) peridotites
d
CaO
MgO
FeO
diopside
hedenbergite
augite

Figure 7

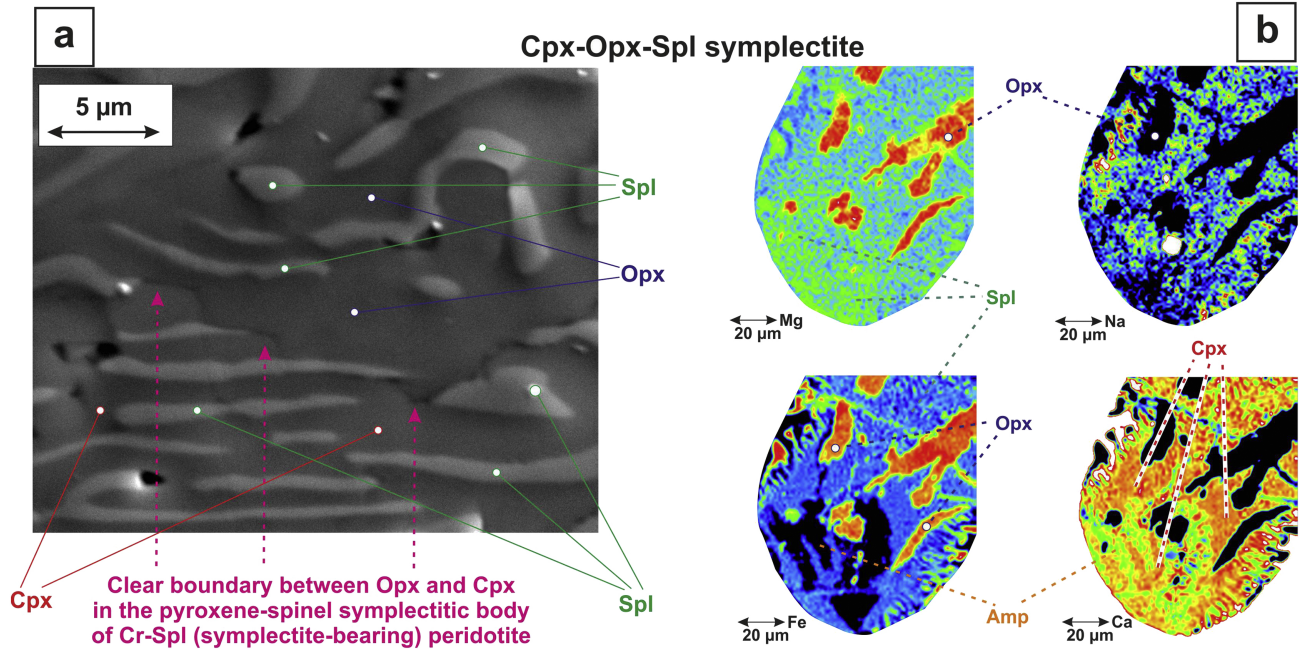
a
Cpx-Opx-Spl symplectite
5 µm
Spl
Opx
Cpx
Clear boundary between Opx and Cpx
in the pyroxene-spinel symplectitic body
of Cr-Spl (symplectite-bearing) peridotite
Spl
b
Opx
Spl
Mg
20 µm
Na
20 µm
Cpx
Opx
Fe
20 µm
Amp
Ca
20 µm

Figure 8

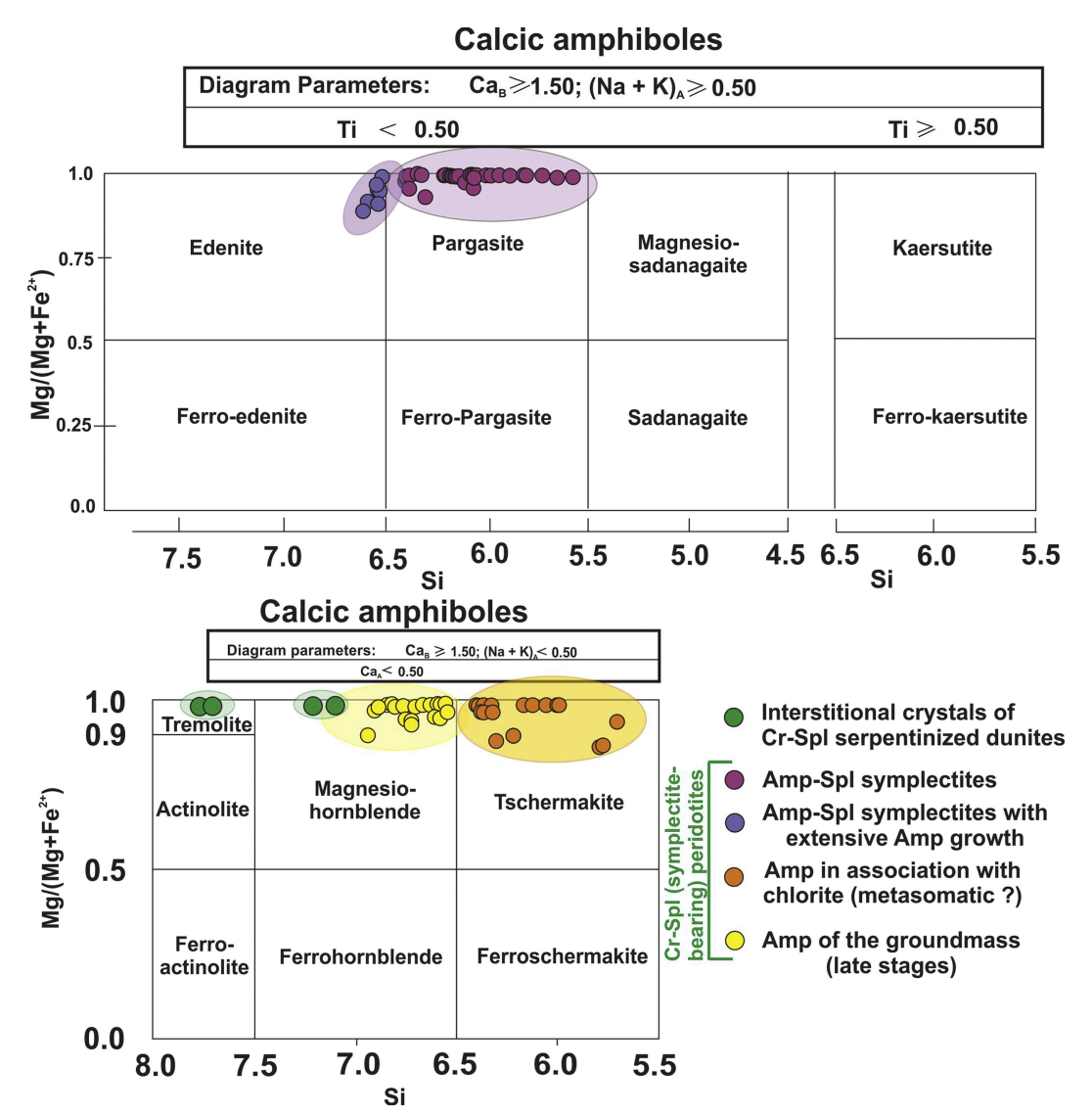
Calcic amphiboles
Diagram Parameters: $Ca_B \geqslant 1.50$; $(Na + K)_A \geqslant 0.50$
Ti < 0.50
Ti ⩾ 0.50
Edenite
Pargasite
Magnesio-sadanagaite
Kaersutite
Ferro-edenite
Ferro-Pargasite
Sadanagaite
Ferro-kaersutite
Mg/(Mg+Fe2+)
Si
Calcic amphiboles
Diagram parameters: $Ca_B \geqslant 1.50$; $(Na + K)_A < 0.50$
$Ca_A < 0.50$
Tremolite
Actinolite
Magnesio-hornblende
Tschermakite
Ferro-actinolite
Ferrohornblende
Ferroschermakite
Mg/(Mg+Fe2+)
Si
Interstitional crystals of Cr-Spl serpentinized dunites
Amp-Spl symplectites
Amp-Spl symplectites with extensive Amp growth
Amp in association with chlorite (metasomatic ?)
Amp of the groundmass (late stages)
Cr-Spl (symplectite-bearing) peridotites

Figure 9

# CFMNASCr system

**EBC (in wt.%): $SiO_2$ = 46.055; $Al_2O_3$ = 9.461; MgO = 28.689; FeO = 8.696; CaO = 6.295; $Na_2O$ = 0.189; $Cr_2O_3$ = 0.261.**

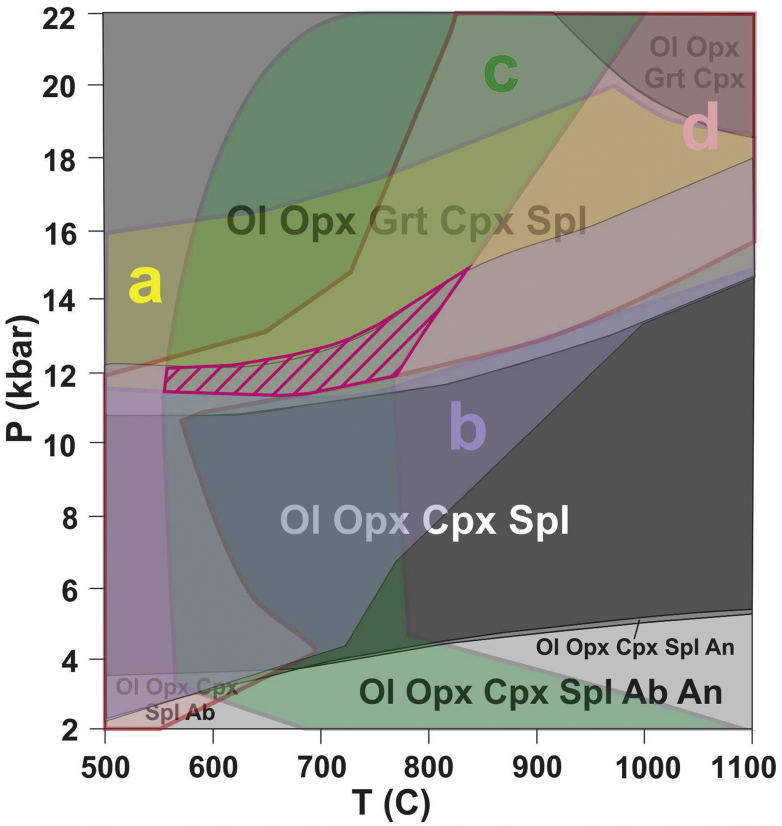


**Minimum is in dark-BLUE – Maximum is in dark-RED**

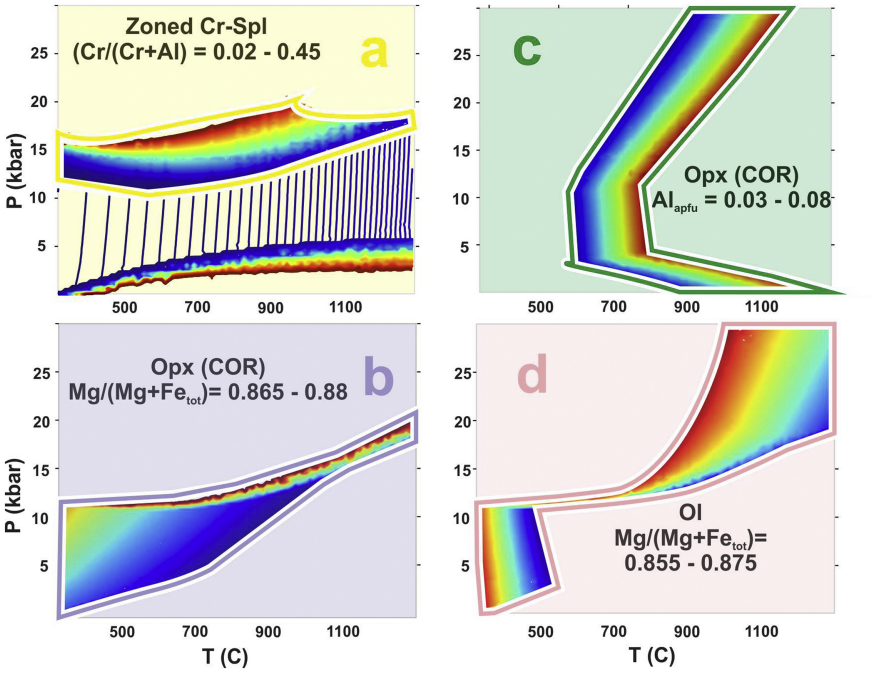


Figure 10

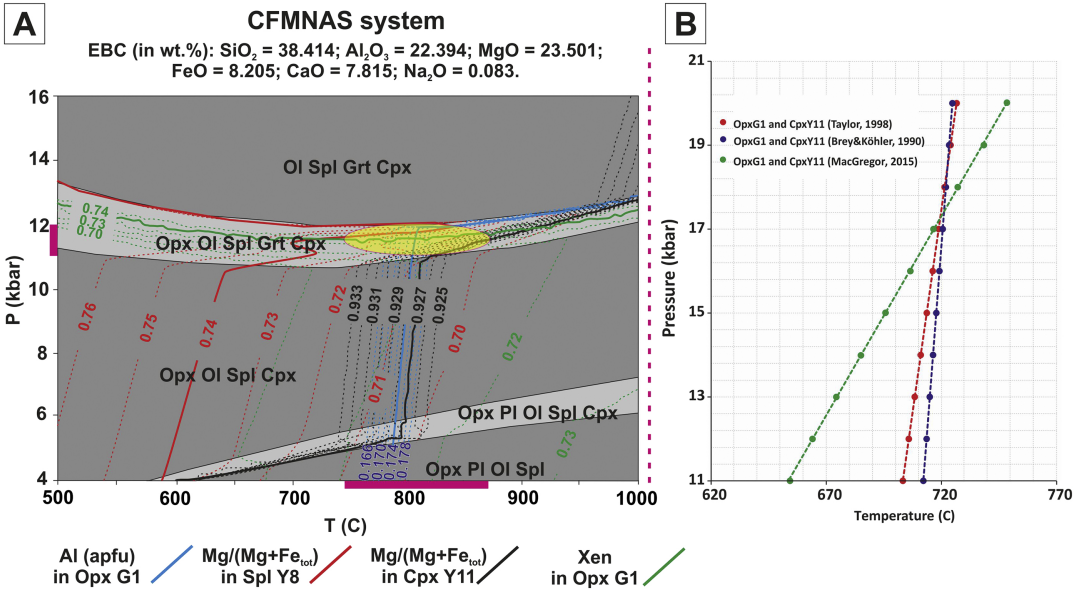
A
CFMNAS system
EBC (in wt.%): SiO2 = 38.414; Al2O3 = 22.394; MgO = 23.501;
FeO = 8.205; CaO = 7.815; Na2O = 0.083.
Ol Spl Grt Cpx
Opx Ol Spl Grt Cpx
Opx Ol Spl Cpx
Opx Pl Ol Spl Cpx
Opx Pl Ol Spl
P (kbar)
T (C)
B
OpxG1 and CpxY11 (Taylor, 1998)
OpxG1 and CpxY11 (Brey&Köhler, 1990)
OpxG1 and CpxY11 (MacGregor, 2015)
Pressure (kbar)
Temperature (C)
Al (apfu) in Opx G1
Mg/(Mg+Fetot) in Spl Y8
Mg/(Mg+Fetot) in Cpx Y11
Xen in Opx G1

Figure 11

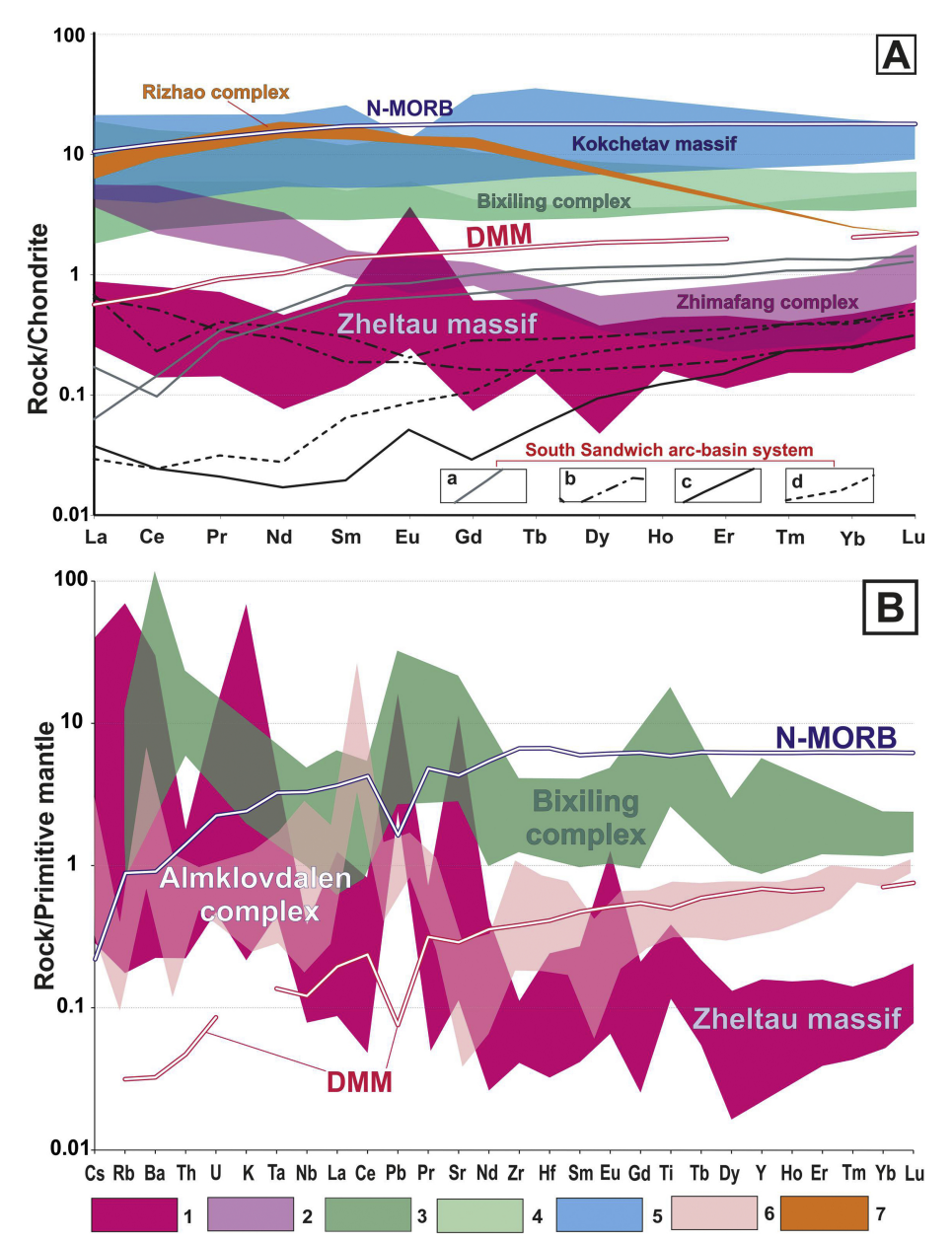
A
Rizhao complex
N-MORB
Kokchetav massif
Bixiling complex
DMM
Zhimafang complex
Zheltau massif
South Sandwich arc-basin system
a
b
c
d
Rock/Chondrite
100
10
1
0.1
0.01
La Ce Pr Nd Sm Eu Gd Tb Dy Ho Er Tm Yb Lu
B
N-MORB
Bixiling complex
Almklovdalen complex
Zheltau massif
DMM
Rock/Primitive mantle
100
10
1
0.1
0.01
Cs Rb Ba Th U K Ta Nb La Ce Pb Pr Sr Nd Zr Hf Sm Eu Gd Ti Tb Dy Y Ho Er Tm Yb Lu
1
2
3
4
5
6
7

Figure 12

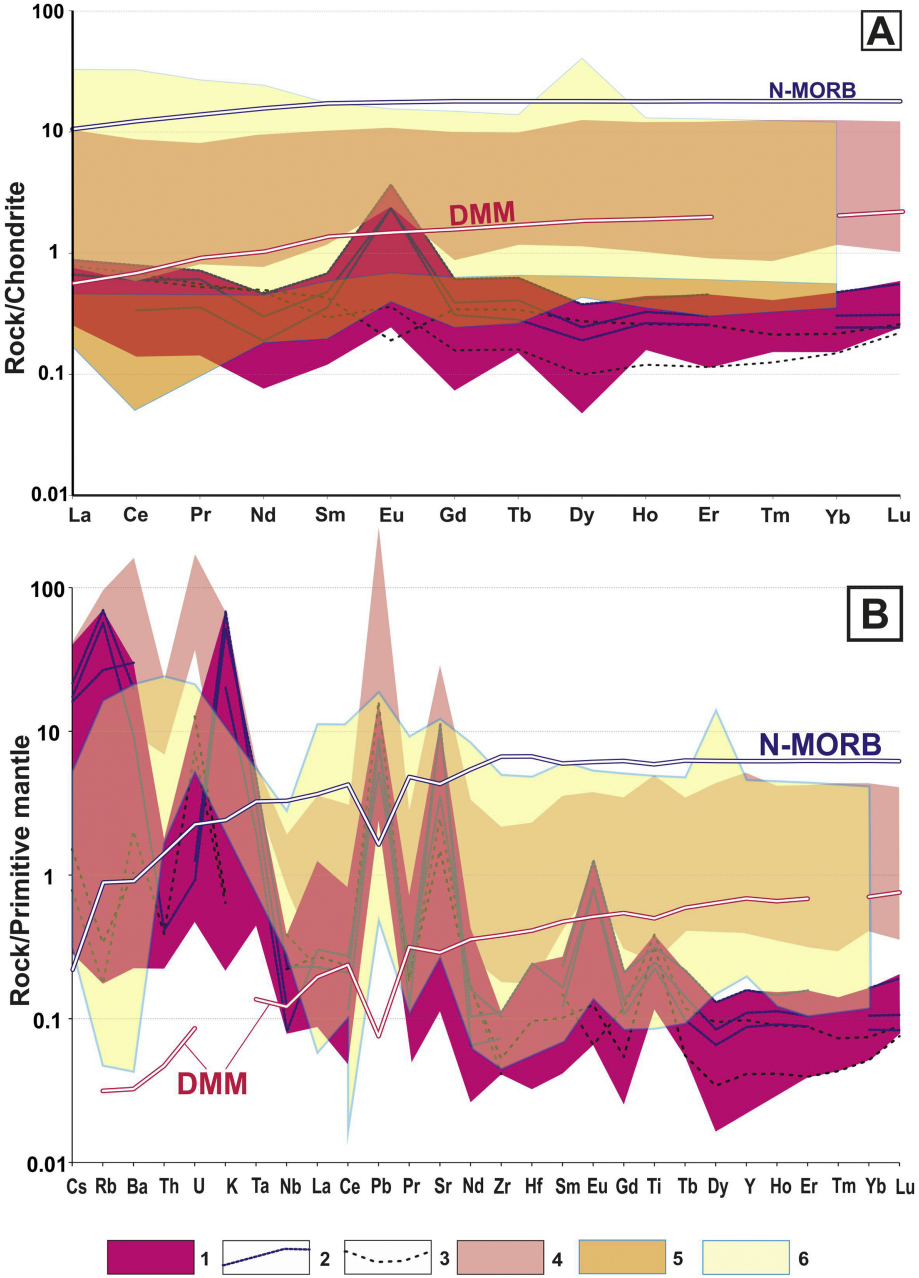
A
N-MORB
DMM
Rock/Chondrite
100
10
1
0.1
0.01
La Ce Pr Nd Sm Eu Gd Tb Dy Ho Er Tm Yb Lu
B
N-MORB
DMM
Rock/Primitive mantle
100
10
1
0.1
0.01
Cs Rb Ba Th U K Ta Nb La Ce Pb Pr Sr Nd Zr Hf Sm Eu Gd Ti Tb Dy Y Ho Er Tm Yb Lu
1
2
3
4
5
6

Figure 13

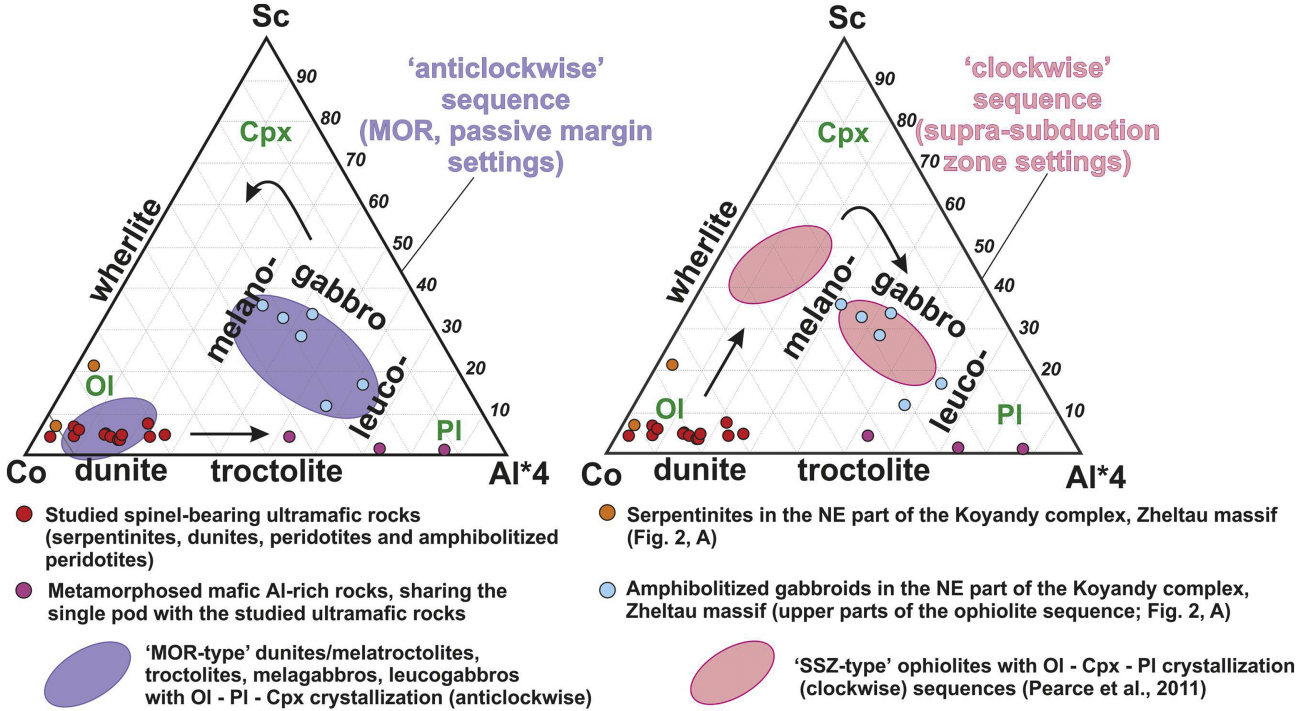
Sc
'anticlockwise' sequence (MOR, passive margin settings)
Cpx
wherlite
melano-
gabbro
leuco-
Ol
Pl
Co
dunite
troctolite
Al*4
90
80
70
60
50
40
30
20
10
Studied spinel-bearing ultramafic rocks (serpentinites, dunites, peridotites and amphibolitized peridotites)
Metamorphosed mafic Al-rich rocks, sharing the single pod with the studied ultramafic rocks
'MOR-type' dunites/melatroctolites, troctolites, melagabbros, leucogabbros with Ol - Pl - Cpx crystallization (anticlockwise) sequences (Pearce et al., 2011)
Sc
'clockwise' sequence (supra-subduction zone settings)
Cpx
wherlite
melano-
gabbro
leuco-
Ol
Pl
Co
dunite
troctolite
Al*4
90
80
70
60
50
40
30
20
10
Serpentinites in the NE part of the Koyandy complex, Zheltau massif (Fig. 2, A)
Amphibolitized gabbroids in the NE part of the Koyandy complex, Zheltau massif (upper parts of the ophiolite sequence; Fig. 2, A)
'SSZ-type' ophiolites with Ol - Cpx - Pl crystallization (clockwise) sequences (Pearce et al., 2011)

Figure 14

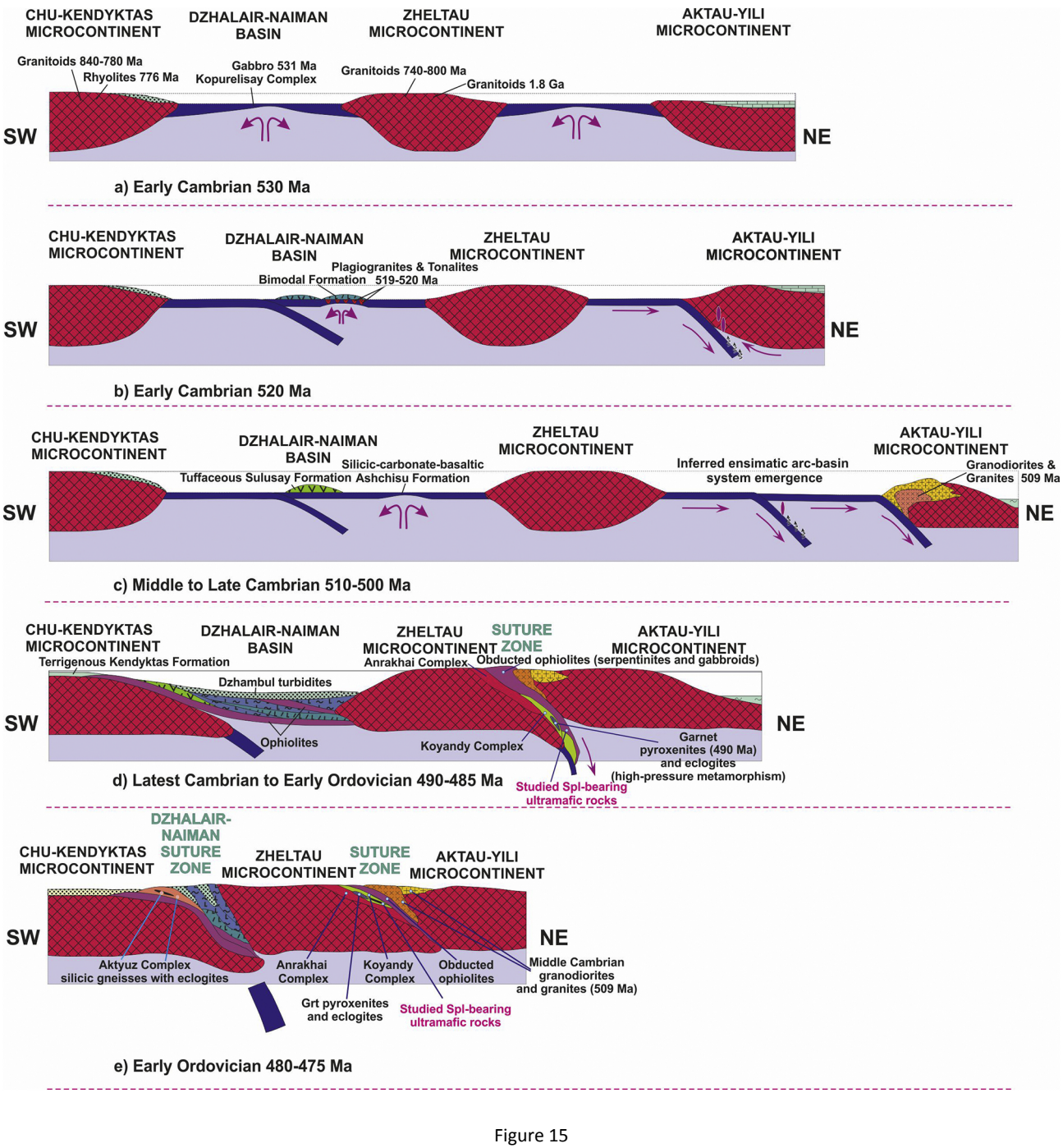
CHU-KENDYKTAS MICROCONTINENT
DZHALAIR-NAIMAN BASIN
ZHELTAU MICROCONTINENT
AKTAU-YILI MICROCONTINENT
Granitoids 840-780 Ma
Rhyolites 776 Ma
Gabbro 531 Ma
Kopurelisay Complex
Granitoids 740-800 Ma
Granitoids 1.8 Ga
SW
NE
a) Early Cambrian 530 Ma
CHU-KENDYKTAS MICROCONTINENT
DZHALAIR-NAIMAN BASIN
ZHELTAU MICROCONTINENT
AKTAU-YILI MICROCONTINENT
Plagiogranites & Tonalites
Bimodal Formation
519-520 Ma
SW
NE
b) Early Cambrian 520 Ma
CHU-KENDYKTAS MICROCONTINENT
DZHALAIR-NAIMAN BASIN
ZHELTAU MICROCONTINENT
AKTAU-YILI MICROCONTINENT
Silicic-carbonate-basaltic
Tuffaceous Sulusay Formation
Ashchisu Formation
Inferred ensimatic arc-basin system emergence
Granodiorites & Granites
509 Ma
SW
NE
c) Middle to Late Cambrian 510-500 Ma
CHU-KENDYKTAS MICROCONTINENT
DZHALAIR-NAIMAN BASIN
ZHELTAU MICROCONTINENT
SUTURE ZONE
AKTAU-YILI MICROCONTINENT
Terrigenous Kendyktas Formation
Anrakhai Complex
Obducted ophiolites (serpentinites and gabbroids)
Dzhambul turbidites
Ophiolites
Koyandy Complex
Garnet pyroxenites (490 Ma) and eclogites (high-pressure metamorphism)
Studied Spl-bearing ultramafic rocks
SW
NE
d) Latest Cambrian to Early Ordovician 490-485 Ma
DZHALAIR-NAIMAN SUTURE ZONE
CHU-KENDYKTAS MICROCONTINENT
ZHELTAU MICROCONTINENT
SUTURE ZONE
AKTAU-YILI MICROCONTINENT
Aktyuz Complex silicic gneisses with eclogites
Anrakhai Complex
Koyandy Complex
Obducted ophiolites
Middle Cambrian granodiorites and granites (509 Ma)
Grt pyroxenites and eclogites
Studied Spl-bearing ultramafic rocks
SW
NE
e) Early Ordovician 480-475 Ma

Figure 15

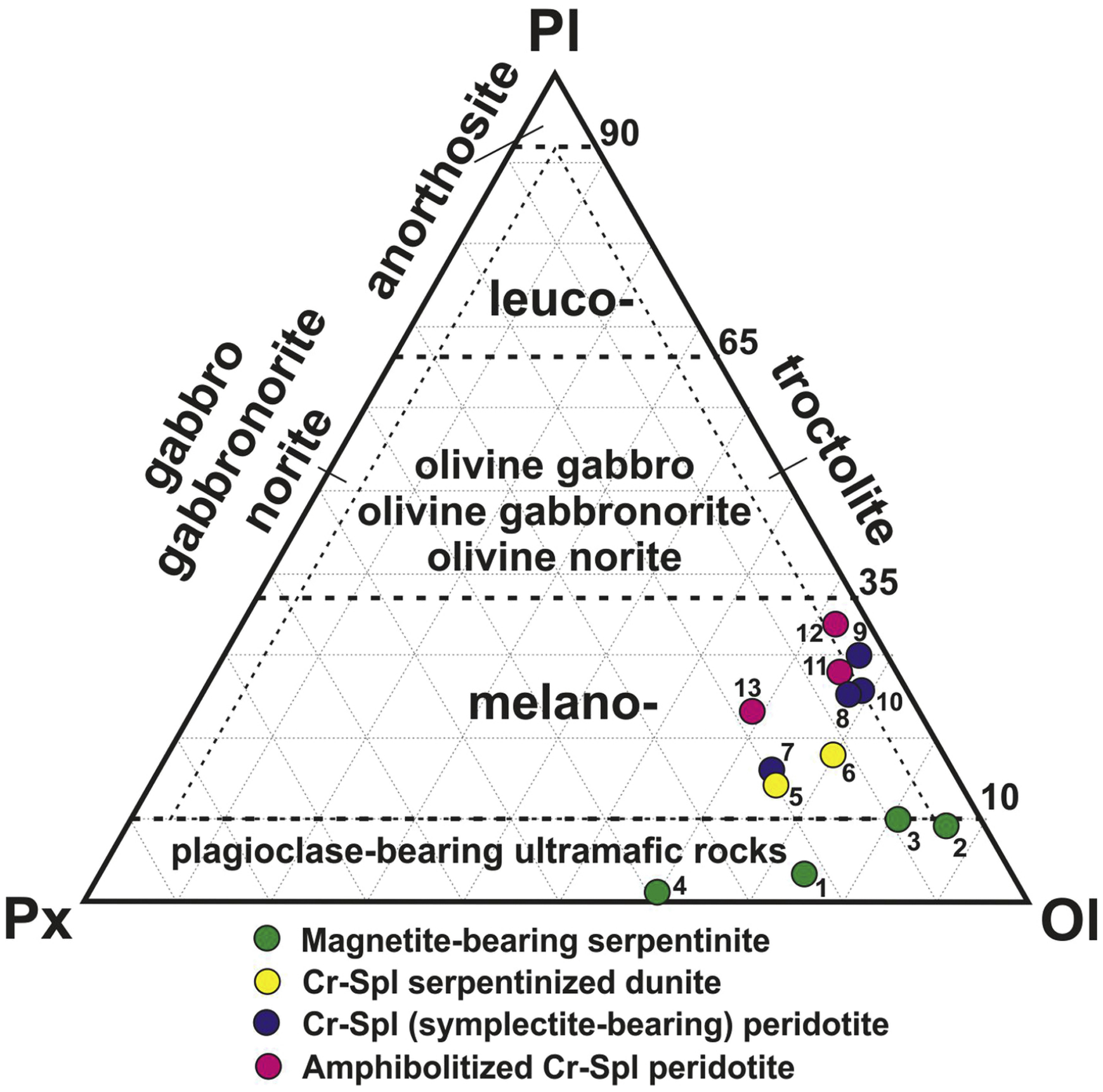
Pl
Px
Ol
anorthosite
gabbro
gabbronorite
norite
troctolite
90
65
35
10
leuco-
olivine gabbro
olivine gabbronorite
olivine norite
melano-
plagioclase-bearing ultramafic rocks
1
2
3
4
5
6
7
8
9
10
11
12
13
Magnetite-bearing serpentinite
Cr-Spl serpentinized dunite
Cr-Spl (symplectite-bearing) peridotite
Amphibolitized Cr-Spl peridotite

Figure 16

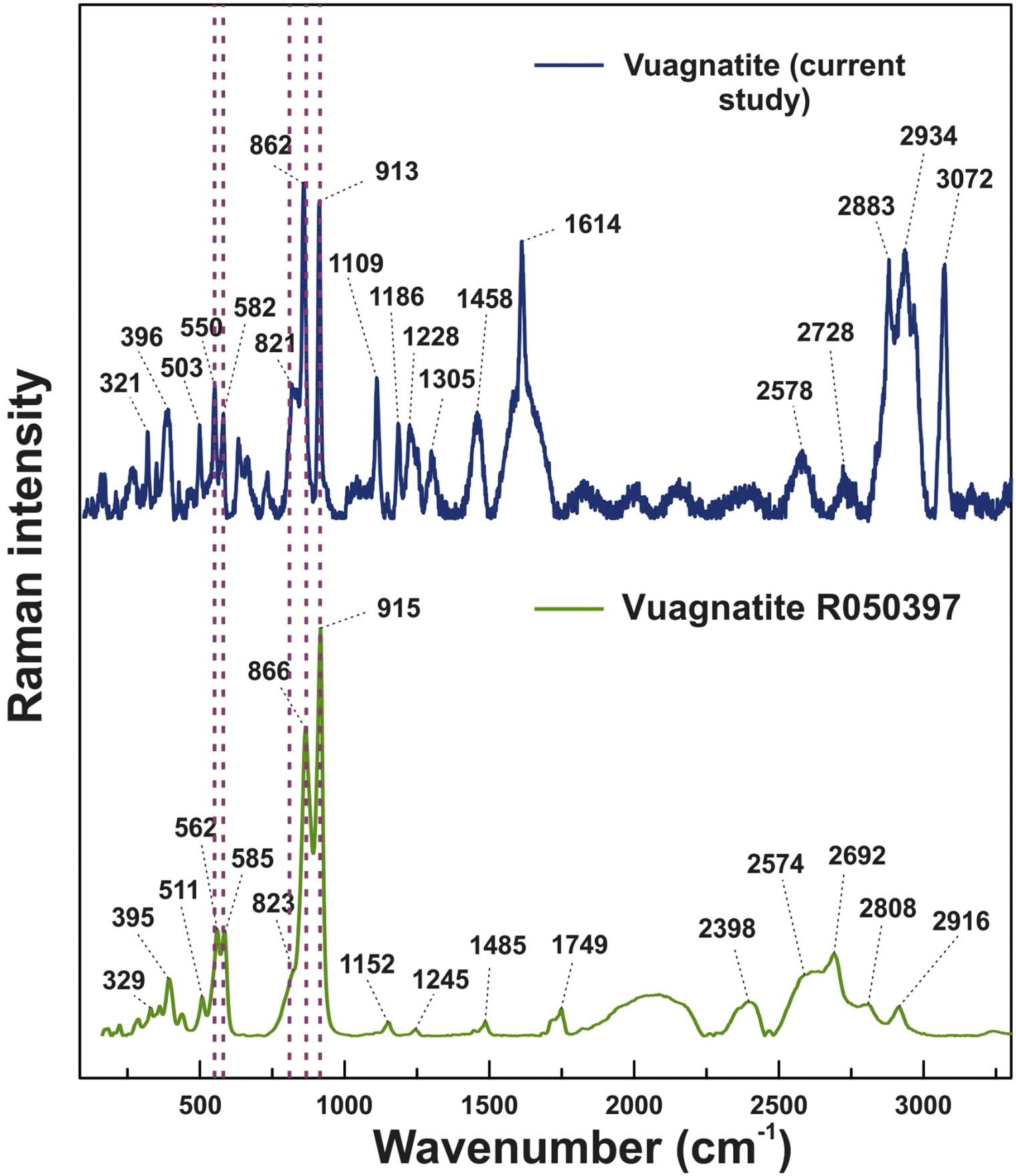
Vuagnatite (current study)
Vuagnatite R050397
Raman intensity
Wavenumber (cm-1)
500
1000
1500
2000
2500
3000
321
329
395
396
503
511
550
562
582
585
821
823
862
866
913
915
1109
1152
1186
1228
1245
1305
1458
1485
1614
1749
2398
2574
2578
2692
2728
2808
2883
2916
2934
3072

Figure 17

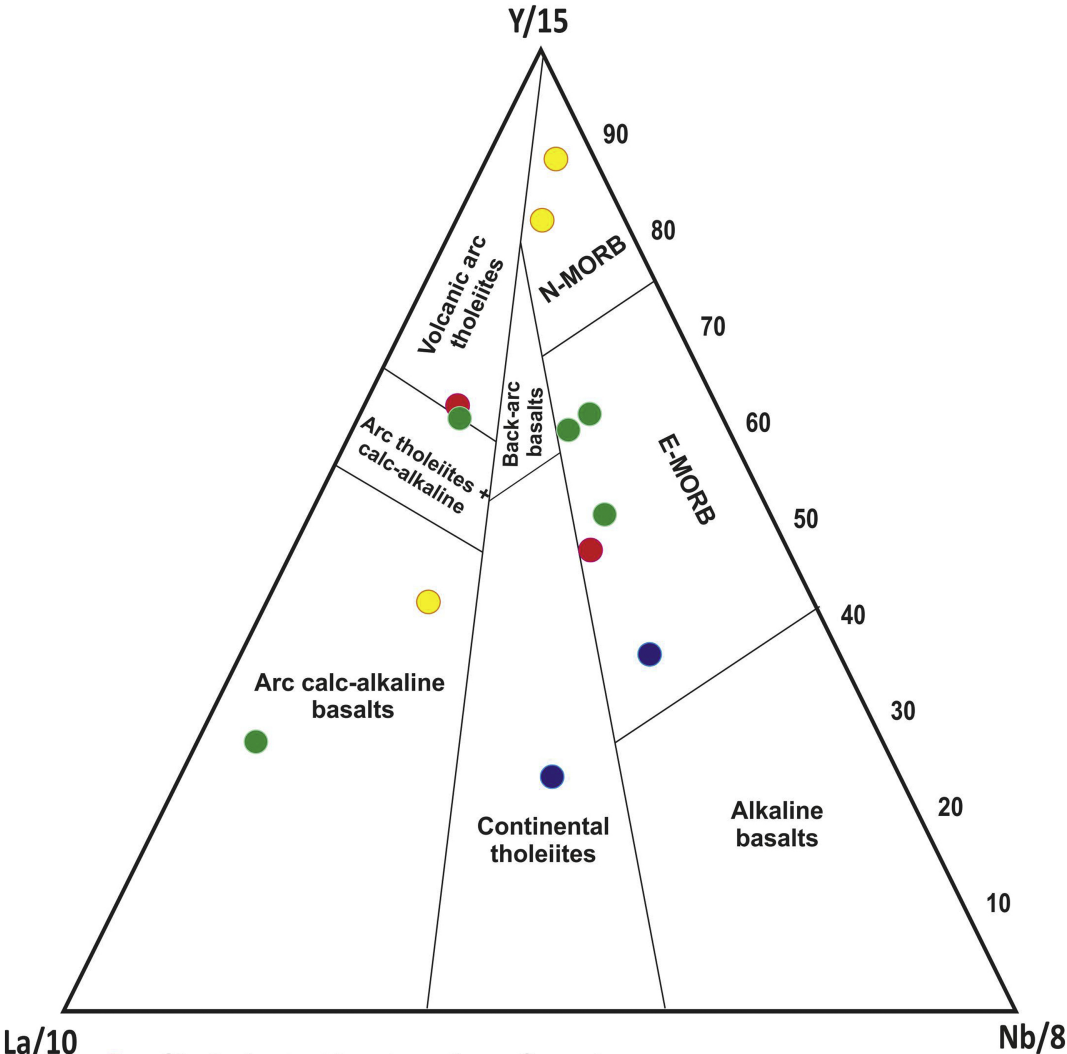


Studied spinel-bearing ultramafic rocks (serpentinites, dunites, peridotites and amphibolitized peridotites)

Metamorphosed mafic Al-rich rocks (20-32 wt.% of $Al_2O_3$), sharing the single pod with the studied ultramafic rocks

Serpentinites in the NE part of the Koyandy complex, Zheltau massif (Fig. 2, A)

Amphibolitized gabbroids in the NE part of the Koyandy complex, Zheltau massif (upper parts of the ophiolite sequence; Fig. 2, A)

Figure 18